RIGOROUS MODELING OF THE RADIATIVE PROPERTIES OF MICRO/NANOSTRUCTURES AND COMPARISONS WITH MEASUREMENTS OF FABRICATED GRATINGS AND SLIT ARRAYS

A Dissertation
Presented to
The Academic Faculty

By

Yu-Bin Chen

In Partial Fulfillment
of the Requirements for the Degree
Doctor of Philosophy in the
School of Mechanical Engineering

Georgia Institute of Technology
May 2007

RIGOROUS MODELING OF THE RADIATIVE PROPERTIES OF MICRO/NANOSTRUCTURES AND COMPARISONS WITH MEASUREMENTS OF FABRICATED GRATINGS AND SLIT ARRAYS

Approved by:

Dr. Zhuomin Zhang, Advisor
George W. Woodruff School of Mechanical Engineering
Georgia Institute of Technology

Dr. F. Levent Degertekin
George W. Woodruff School of Mechanical Engineering
Georgia Institute of Technology

Dr. Peter J. Hesketh
George W. Woodruff School of Mechanical Engineering
Georgia Institute of Technology

Dr. Gee-Kung Chang
School of Electrical and Computer Engineering
Georgia Institute of Technology

Dr. Pei-feng Hsu
Department of Mechanical and Aerospace Engineering
Florida Institute of Technology

Date Approved: 03/30/2007

ACKNOWLEDGEMENTS

First, I want to address my sincere appreciation to my Ph.D. advisor, Dr. Zhuomin Zhang, for his guidance, support, and encouragement all these years. He has put his best efforts for my future success and laid down tremendous influences on me. I would also like to thank my Ph.D. dissertation reading committee members, Dr. F. Levent Degertekin and Dr. Gee-Kung Chang, for their willingness to serve on my committee and provide valuable suggestions in various aspects of my work. Specifically, I would like to thank Dr. Peter J. Hesketh and Dr. Pei-feng Hsu, who are also my committee members, together with Dr. William P. King. They gave me opportunities to learn from them and work with their group members. The same appreciation is given to Dr. Paul J. Timans for our excellent collaboration experience.

Much appreciation is expressed to all my former and current colleagues whom I enjoyed interacting with during the study. I want to thank Dr. Ceji Fu and Dr. Qunzhi Zhu for their help during my first two years at Atlanta. I thank Mr. Soumyadipta Basu, Mr. Bong Jae Lee, and Dr. Hyunjin Lee for their valuable suggestions and our joyful working experience. I also thank Dr. Qinhe Lee and Mr. Keunhan Park for their friendship and supports.

I am very grateful to my parents, parents-in-law, and my brother as well as brother-in-law for their love and support through all these years when I am far away from them. I also want to thank my wife, Wan-yu Chen, who is always patient and takes good care of my two lovely angels, Renny and Rosie. Their participation in my Ph.D. life makes it much more fruitful.

TABLE OF CONTENTS

	Page
ACKNOWLEDGEMENTS	iii
LIST OF TABLES	vi
LIST OF FIGURES	vii
LIST OF SYMBOLS AND ABBREVIATIONS	xi
SUMMARY	xv
CHAPTER	
1 INTRODUCTION	1
2 THEORETICAL FOUNDATIONS	8
2.1 Background	8
2.2 Effective Medium Formulations	11
2.3 Rigorous Coupled-Wave Analysis for Transverse Electric Wave	13
2.4 Rigorous Coupled-Wave Analysis for Transverse Magnetic Wave	22
2.5 Rigorous Coupled-Wave Analysis for Conical Diffraction	25
3 DIFFRACTION EFFICIENCY OF MICROSTRUCTURES	36
3.1 1D and 2D Microstructure Design and Fabrication	36
3.2 Instrumentation	41
3.3 Diffraction Efficiency Measurements	43
4 ABSORPTANCE OF NANOSCALE PATTERNED WAFER	50
4.1 Model Development and Algorithm Validation	50
4.2 Spectral Absorptance	57
4.3 Validity Assessment for Effective Medium Formulations	65

4.4 Directional Absorptance 68
5 SPECTRAL AND DIRECTIONAL EMITTANCE CONTROL 73
5.1 Micro/Nanostructures for Thermophotovoltaic System 73
5.2 Complex Grating Design for Thermophotovoltaic Radiators 77
5.3 Emittance Modeling 89
6 TRANSMITTANCE THROUGH NANOSCALE SLIT ARRAYS 96
6.1 Transmission Enhancement 97
6.1.1 Wood's Anomaly 100
6.1.2 Cavity Resonance 104
6.1.3 Effective Medium 113
6.2 Near-Field Confinement 119
6.3 Sample Fabrication and Transmission Measurement 131
7 SUMMARY CONCLUSIONS AND RECOMMENDATIONS 142
REFERENCES 147

LIST OF TABLES

		Page
Table 4.1	Feature dimensions of selected cases (Unit: nm)	53
Table 4.2	Total absorptance for different cases at 910°C	63
Table 6.1	Calculated η_s, η_u, and T for slit arrays with 1, 2, or 3 slits per period, for TM waves at normal incidence and $\lambda = 10.64$ μm	127
Table 6.2	Lateral dimension of submicron metallic slit arrays	134

LIST OF FIGURES

		Page
Figure 2.1	Coordinate and angles for the definition of bidirectional reflectance of periodic structure	9
Figure 2.2	Diffraction of the TE wave on a binary grating	15
Figure 2.3	Conical diffraction on a binary grating	26
Figure 2.4	Illustrations of a conical diffraction from a 1D grating in: (a) 3D *k*-space; (b) projected to the $k_x - k_z$ plane	29
Figure 3.1	SEM and AFM images of three different samples: (a) and (b) are 1D features with $w = 4$ μm; (c) and (d) are 1D features with $w = 1$ μm; (e) and (f) are 2D features with $w_1 = w_2 = 1$ μm	39
Figure 3.2	Schematic drawings of three automatically controlled stages for the TAAS	42
Figure 3.3	Diffraction efficiency of a 1D microstructure with $\Lambda = 5$ μm and $w = 4$ μm. The incidence zenith angles are: (a) $\theta = 0^\circ$; (b) $\theta = 15^\circ$; (c) $\theta = 30^\circ$	44
Figure 3.4	Diffraction efficiency of a 1D microstructure with $\Lambda = 5$ μm and $w = 1$ μm. The incidence zenith angles are: (a) $\theta = 0^\circ$; (b) $\theta = 15^\circ$; (c) $\theta = 30^\circ$	46
Figure 3.5	Diffraction efficiency of 2D microstructures	49
Figure 4.1	Structure sketches of selected cases, where d_G and d_T are the depths of gate and trench, respectively. l_G, l_P, and l_T are the lengths of gate, pitch, and trench, respectively	51
Figure 4.2	Optical constants of silicon at 25°C, 700°C, and 910°C: (a) refractive index; (b) extinction coefficient	55
Figure 4.3	Calculated normal, spectral absorptance for plain Si (Case A-1) and SiO_2-coated Si (Case A-2) at 25°C, 700°C, and 910°C	58
Figure 4.4	Spectral absorptance predicted using RCWA for cases with gratings at 910°C at $\theta = 0^\circ$ and 45°: (a) Case A-3; (b) Case B-1; (c) Case B-2; (d) Case B-3	60

Figure 4.5 Comparison of the absorptance predicted by different methods at 910°C: (a) TE wave for Case A-3; (b) TM wave for Case A-3; (c) TE wave for Case B-1; (d) TM wave for Case B-1; (e) TE wave for Case B-3; (f) TM wave for Case B-3 66

Figure 4.6 Effect of incidence angle on the absorptance at 910°C for cases without gates: (a) TE wave for Case A-1; (b) TM wave for Case A-1; (c) TE wave for Case A-2; (d) TM wave for Case A-2; (e) TE wave for Case A-3; (f) TM wave for Case A-3 71

Figure 4.7 Effect of incidence angle on the absorptance at 910°C for cases with gates: (a) TE wave for Case B-1; (b) TM wave for Case B-1; (c) TE wave for Case B-2; (d) TM wave for Case B-2; (e) TE wave for Case B-3; (f) TM wave for Case B-3 72

Figure 5.1 Schematic of a binary 1D tungsten grating for a TM wave incident from air at an incidence angle θ, where **k** is the wavevector, **H** is the magnetic field, and **E** is the electric field. The geometry of the binary grating is determined by its period (Λ), filling ratio (*f*), and ridge height (*h*) 79

Figure 5.2 Dispersion curves of tungsten shallow gratings for two periods: Λ_1 = 1.6 μm (solid line with squares) and Λ_2 = 3.2 μm (dashed line with open circles) 80

Figure 5.3 Amplitudes of the diffraction order with dominant evanescent fields at different wavelengths: (a) amplitude of −1 order at oblique incidence; (b) amplitude of +1/-1 orders at normal incidence 82

Figure 5.4 Emittance of 1D tungsten binary gratings for TM waves: (a) effects of filling ratio and emission angle for *h* = 0.2 μm and Λ = 1.6 μm; (b) effects of grating period and height for normal emittance 85

Figure 5.5 Tungsten complex grating formed by superposition of two simple gratings: (a) short-period (Λ = 0.4 μm) simple grating I; (b) long-period (Λ = 1.6 μm) simple grating II; (c) the generated complex grating with Λ = 1.6 μm and ridges of the same height (0.2 μm) 87

Figure 5.6 Spectral emittance of plain tungsten and tungsten gratings for TM waves at (a) $\theta = 0^\circ$ and (b) $\theta = 60^\circ$ 91

Figure 5.7 Directional emittance for TM waves of λ = 1.0 μm (short dashed line), 1.6 μm (long dashed line), and 2.2 μm (solid line): (a) plain tungsten; (b) simple grating I; (c) simple grating II; (d) complex grating 95

Figure 6.1 Transmittance and absorptance of the free-standing Ag grating with $\Lambda = 400$ nm, $d = 800$ nm, and $w = 200$ nm when the plane of incidence is perpendicular to the grating grooves for: (a) TE wave; (b) TM wave 99

Figure 6.2 Square of the magnitude of complex magnetic field in logarithmic scale for TM wave over the two grating periods: (a) $\lambda = 398$ nm; (b) $\lambda = 402$ nm 103

Figure 6.3 Square of the magnitude of complex magnetic field when the cavity resonance occurs for TM waves over the two grating periods: (a) $\lambda = 1950$ nm; (b) $\lambda = 960$ nm and that of complex electric field for TE waves: (c) $\lambda = 484$ nm; (d) $\lambda = 444$ nm 106

Figure 6.4 Effects of the geometric parameters on the cavity resonance of Ag gratings for TM waves. The geometric parameters of the base case are $\Lambda = 400$ nm, $d = 800$ nm, $w = 200$ nm, and $\phi = 0^\circ$. Only one of the parameters is varied in each of the following cases: (a) different thicknesses; (b) different slit widths; (c) different periods 109

Figure 6.5 Contour plot of the transmittance with respect to the wavelength and the incidence angle for the grating with the same geometric parameters as in Fig. 6.1: (a) $\phi = 30^\circ$ and $\psi = 0^\circ$; (b) $\phi = 30^\circ$ and $\psi = 90^\circ$. The inset shows the solution of Wood's anomaly determined by Eq. (6.2) 112

Figure 6.6 Effective medium behavior of the grating structure in the mid-IR spectral region for the TM wave: (a) effective optical constants of the Ag grating with $f = 0.5$; (b) transmittance based on the EMT (solid line) when $\Lambda = 400$ nm, $d = 800$ nm, and $f = 0.5$, and those from RCWA for gratings (dashed line for $\Lambda = 400$ nm; dash-dotted line for $\Lambda = 800$ nm) with the same f and d; (c) transmittance from the EMT (dotted lines) and RCWA (solid lines) with different filling ratios when $\Lambda = 400$ nm and $d = 800$ nm 115

Figure 6.7 Transmittance of the Ag grating with the same geometric parameters as in Fig. 6.1: (a) the PoI is perpendicular to the grating grooves; (b) the PoI is parallel to the grating grooves 117

Figure 6.8 Square of the magnitude of complex magnetic field and Poynting vector distribution for TM waves over the two grating periods at $\lambda = 8$ μm 118

Figure 6.9 Effective medium behavior of the grating structure in the MIR spectral region for the TM wave: (a) the schematic of the Al grating, whose geometry is defined by the thickness *d*, period Λ, and slit width *w*; (b) spectral transmittance of the Al grating at normal incidence based on RCWA and EMT. The geometric parameters of the Al grating are $d = 100$ nm, $l = 250$ nm, and $w = 50$ nm, where $\Lambda = l + w = 300$ nm 121

Figure 6.10 Energy density and the Poynting vector distributions for the Al grating with two slits per period SA-2, whose geometric parameters are given in Table 6.1: (a) energy density; (b) Poynting vector 123

Figure 6.11 Energy density distribution for the Al grating with three slits in a period SA-3 126

Figure 6.12 The spectral transmittance for the structure of Al grating mounted on a silicon substrate at normal incidence for the TM wave based on RCWA and EMT 128

Figure 6.13 The normalized energy density distribution of the Al grating on Si structure over one grating period at various distances from the exit plane of the slit array: (a) when the radiation is incident from vacuum (SA-4); (b) when the radiation is incident from silicon (SA-5) 130

Figure 6.14 Fabrication of periodic nanoscale slit arrays. (a) exposing electron beam; (b) developing the resist; (c) evaporating metals; (d) stripping the resist 133

Figure 6.15 SEM images of: (a) Sample No.2; (b) Sample No. 3 135

Figure 6.16 Set-up of normal transmission measurement for nanoscale slit arrays 136

Figure 6.17 Normal transmittance of plain 400-μm-thick silicon substrate 137

Figure 6.18 Normal transmittance of nanoscale metallic slit arrays: (a) TE waves and (b) TM waves for sample No. 1; (c) TE waves and (d) TM waves for sample No. 2; (e) TE waves and (f) TM waves for sample No. 3 141

LIST OF SYMBOLS AND ABBREVIATIONS

d	=	layer thickness, m
E	=	electric field vector (V/m) or matrix of the dielectric function
EM	=	electromagnetic
EMA	=	effective medium approximation
EMT	=	effective medium theory
f	=	filling ratio
G	=	spectral irradiation, $W/m^2 \cdot nm$
H	=	magnetic field vector, A/m
h	=	ridge height, m
I	=	unit matrix
I	=	intensity, $W/m^2 \cdot sr$
i	=	$\sqrt{-1}$
j	=	diffraction order
k	=	wavevector, 1/m
k_x	=	wavevector component in the x-direction, 1/m
k_y	=	wavevector component in the x-direction, 1/m
k_z	=	wavevector component in the z-direction, 1/m
l	=	lateral width, m
n	=	refractive index
PoI	=	plane of incidence
R	=	reflectance

R_j	=	Fresnel reflection coefficient of *j*th order diffraction
RCWA	=	rigorous coupled-wave analysis
SPP	=	surface plasmon polaritons
T_j	=	Fresnel transmission coefficient of *j*th order diffraction
TE	=	transverse electric
TM	=	transverse magnetic
TPV	=	thermophotovoltaic
t	=	time, s
u	=	energy density, J/m^3
w	=	slit width, m

Greek Symbols

α	=	absorptance
$\alpha'^{\cap}_{\lambda}$	=	spectral directional-hemispherical absorptance
β	=	phase shift, rad
γ	=	vector component of space-harmonic magnetic field
δ_{j0}	=	Kronecke delta
$\delta\Omega$	=	solid angle of the beam
ε	=	relative (electric) permittivity or dielectric function
ε'_{λ}	=	spectral directional emissivity
ε_0	=	permittivity of vacuum, 8.854×10^{-12} F/m
η	=	diffraction efficiency

θ	=	zenith angle, degree
κ	=	extinction coefficient
Λ	=	structure period, m
λ	=	wavelength, m
μ	=	relative (magnetic) permeability
μ_0	=	permeability of vacuum, $4\pi\times10^7$ H/m
ρ	=	reflectance
ρ''_λ	=	spectral bidirectional reflectance
$\rho'^{\cap}_\lambda$	=	spectral directional-hemispherical reflectance
$\tau'^{\cap}_\lambda$	=	spectral directional-hemispherical transmittance
ϕ	=	azimuthal angle (degree) or lateral shift (m)
χ	=	vector component of space-harmonic electric field
ψ	=	electric field oscillation angle, degree
ω	=	angular frequency, rad/s

Subscripts

G	=	gate
i	=	incidence
r	=	reflection
P	=	period
T	=	trench
t	=	transmission

Superscripts

inv	=	inverse
ord	=	ordinary
*	=	conjugate of a complex number

SUMMARY

Radiative properties of a material is the core of thermal science and optics, which play critical roles in modern technologies, including microelectronics, energy conversion, and nanotechnology. The key to modify or enhance radiative properties is employing one-, two-, and three-dimensional (1, 2, and 3D) periodic micro/nanostructures. Since their applications are not fully uncovered and very few comprehensive studies are available, the objective of this dissertation is to explore applications of periodic micro/nanostructures with modified radiative properties in modern technologies through both numerically and experimentally investigations. Theses representative applications include the thermal control in rapid thermal processing, the design of a wavelength-selective radiator for thermophotovoltaic systems, and the nanothermal manufacturing.

The theoretical foundation of the study is built on the rigorous coupled-wave analysis (RCWA) for numerical calculation of the far-field radiative properties and the electromagnetic field distribution in the near-field regime. Measurements of diffraction efficiencies are conducted on fabricated 1D and 2D periodic silicon microstructures with a laser scatterometer/diffractometer with high angular resolution. The diffraction efficiency can be employed for non-contact surface profile inspection tool because it strongly depends on structure patterns.

For better temperature control during rapid thermal processing, the dissertation performs a parametric study on radiation absorption of a generic CMOS device together with its simplified nanoscale structures. The applicability of approximation models, which homogenize micro/nanostructures into a film, is also evaluated. Next, a new

concept of complex gratings is proposed for actively tailoring the radiative properties and serving as a thermophotovoltaic (TPV) radiator. The radiator exhibits a wide-band and angle-independent high transverse magnetic wave emittance matching the bandgap of TPV cells so that the energy conversion efficiency can be improved. Furthermore, the nanoscale metallic slit arrays show polarization-dependant enhanced transmission and highly localized electromagnetic energy density, which hold promising potentials in nanothermal manufacturing. Three submicrometer metallic slit arrays are fabricated on top of a silicon substrate. Their spectral transmittance is measured with a Fourier-transform infrared spectrometer and largely agrees with RCWA modeling results. In short, the dissertation clearly demonstrates that precise control and tuning of radiative properties using micro/nanofabrication are not only feasible but also may have numerous technological impacts.

CHAPTER 1

INTRODUCTION

Radiative properties of a material is the core of thermal science and optics, which play critical roles in modern technologies, including microelectronics, energy conversion, and nanotechnology. The key to enhance the radiative properties is employing one-, two-, and three-dimensional (1, 2, and 3D) periodic structures (Basu *et al.*, 2007). Although it has been known for a long time that radiative properties can be modified by periodic surface features, earlier studies mainly dealt with rather simple geometries and were mostly for metallic surfaces (Brewster, 1992; Siegel and Howell, 2002; Modest, 2003). Due to the recent development of micro/nanofabrication, the ability to manufacture, control, and manipulate periodic structures at extremely small scales is feasible and shows promising application potentials. Some attractive radiative properties were discovered (Hesketh *et al.*, 1986; Greffet *et al.*, 2002), and more exciting findings of complicated microstructures or nanostructures are expected. However, very few experimental data together with rigorous modeling results are available in a comprehensive study. Moreover, the potential applications of micro/nanostructure radiative properties in modern technologies were not fully uncovered. Hence, the objective of this dissertation is to explore applications of periodic micro/nanostructures with modified radiative properties in modern technologies through both numerically and experimentally investigations.

It is imperative to have a rigorous modeling algorithm applicable to micro/nanostructure radiative property calculation from the ultraviolet to mid-infrared.

Besides, radiative properties of nanostructures may be very different from those of microstructures made of similar materials (Zhang *et al.*, 2003). A number of researchers have modeled relatively simple patterned structures on wafers and obtained reasonable agreement with experimental results at wavelengths longer than 0.4 μm (Erofeev *et al.*, 1995; Hebb and Jensen, 1998; Tada *et al.*, 2000; Liu *et al.*, 2004). Though many rigorous numerical methods were proposed, their calculation efficiency is low, especially for modeling nanoscale structures. On the contrary, some approximation methods, which homogenize the micro/nanostructures into one layer with effective optical constants, may provide modeling results much faster, but their accuracy is not guaranteed with the wavelength close to the feature size. Hence, an efficient and rigorous numerical algorithm, rigorous coupled-wave analysis (RCWA), will be employed to assess the approximation method applicability.

The RCWA is one of the efficient tools for modeling radiative properties of periodic gratings by solving Maxwell's equations regardless of feature size (Moharam *et al.*, 1995a; Moharam *et al.*, 1995b). For 1D gratings, the RCWA algorithm is well established with the plane of incidence (PoI) perpendicular to the grating grooves. In this case, a modification for convergence efficiency enhancement has been proposed by Li (1996) for TM (transverse magnetic) waves. When the PoI is not perpendicular to the grating grooves, diffracted waves do not lie in the PoI except the zeroth order, and all the reflected waves lie on a conical surface (i.e., conical diffraction). Since conical diffraction is more general and complicated, its formulations (Han *et al.*, 1992; Moharam *et al.*, 1995a; Peng and Morris, 1995) were not modified accordingly. Therefore, concise and corrected mathematical formulations for RCWA will be presented here as the

theoretical foundation. Both far-field radiative properties and near-field electromagnetic (EM) fields can be obtained from the RCWA regardless of PoI orientations.

In addition to the theoretical study, the emergence of microfabrication has led to more systematic investigations of the influence of microstructure on radiative properties. Hesketh et al. (1986; 1988) and Wang and Zemel (1993) observed emissivity enhancement from micromachined 1D silicon surfaces with period between 10 and 22 μm due to the excitation of surface phonon polaritons (Carminati and Greffet, 1999). Reflectance from 1D periodic metallic surface with different profiles is also measured (Cohn *et al.*, 1997). Radiative properties of 2D microstructures were also experimentally studied, such as the bidirectional reflection (Tang and Buckius, 1998), coherent reflection (Maruyama *et al.*, 2001), and emission (Sai and Yugami, 2004). Because high angular resolution measurement is rarely found, multiple diffraction orders from fabricated 1D and 2D silicon microstructures will be obtained by a high resolution laser scatterometer/diffractometer in this dissertation. The microstructure profiles will also be measured for the clear explanation to the radiative property modification by periodic structures.

Based on the understanding of numerical algorithms and diffraction efficiency measurement, the objective of the dissertation is to explore application potentials of periodic micro/nanostructure radiative properties in microelectronics, energy conversion, and nanotechnology. Three representative applications are the thermal control in rapid thermal processing (RTP), the design of a wavelength-selective radiator for thermophotovoltaic (TPV) systems, and the nanothermal manufacturing. According to the International Technology Roadmap for Semiconductors (ITRS, 2004), the gate length

and junction depth will be 25 and 13.8 nm, respectively, for the 65-nm devices used in high-performance complementary metal oxide semiconductor (CMOS) technology. RTP currently provides the high-temperature annealing needed; however, conventional RTP tools encounter a dilemma between limiting the junction depth and maximizing the degree of electrical activation of implanted dopants (Gelpey *et al.*, 2002). This difficulty can be overcome by using high-intensity flash-lamps with millisecond optical pulses to raise the wafer surface temperature to around 1300°C. The energy sources are Ar or Xe arc lamps, which mainly emit ultraviolet and visible radiation. During the flash-lamp heating, thermal energy is absorbed at the wafer surface due to the small penetration depth of Si. The energy is absorbed within milliseconds; consequently, thermal diffusion cannot distribute heat uniformly across the wafer surface. Note that temperature uniformity is critical because it may cause uneven implant activation and excessive thermal stresses introducing crystallographic defects (Bentini and Correra, 1983). A major reason for the temperature nonuniformity arises from the absorptance difference of various device patterns. Therefore, studying the strong influence on the radiative properties of micro/nanostructures will be necessary for better thermal control of semiconductor device fabrication.

Since radiative properties of a material strongly depend on its surface periodic structures, their second application is to actively tailor emissivity. Tailoring radiative properties is important for energy conversion systems, such as solar cells and TPV devices (Coutts, 1999). The conversion efficiency can be enhanced by modified reflectance and emittance spectra using periodic micro/nanostructures. 1D deep gratings (Hesketh *et al.*, 1986) and 2D microcavities (Maruyama *et al.*, 2001) can enhance the

emittance via resonance modes. Gratings can also excite surface electromagnetic (EM) waves, or polaritons, for coherent thermal emission due to its periodic structure (Kreiter *et al.*, 1999; Greffet *et al.*, 2002). The cavity resonance modes and surface polaritons can interplay for the development of a TPV radiator with specific radiative properties. A TPV radiator is a thermal emitter working in the operating wavelength region of typical TPV cells, which transfer the photon energy into electric power. This conversion occurs when the wavelength is shorter than the cut-off wavelength of the bandgap of TPV cells. The absorption of the emitted energy at wavelengths longer than the cut-off wavelength produces no photocurrent and cause thermal leakage. On the other hand, thermal emission at short wavelengths ($< 0.6\ \mu m$) is not significant for usual TPV heating source (~1500 K). Besides, the efficiency is lower at short wavelengths due to the shallow penetration depth and the fast electron-hole recombination. Accordingly, an ideal TPV radiator should have a high broad-band emittance peak within the wavelength region of interest but low emittance at long wavelengths. Furthermore, the spectral emittance peak should be independent of direction. The dissertation will try to fulfill such specific emittance requirements by utilizing periodic nanostructures.

In fact, nanostructures can play the role as a mother by taking advantages of radiation transmission. This is a kind of nanothermal manufacturing or nanolithography, which gives birth of replicated micro/nanostructures with high throughput and resolution. Traditional photolithography has dominated the fabrication of microstructures for a long time due to its low cost and fabrication flexibility. However, as the semiconductor device size keeps shrinking down to nanoscale for higher density and better performance, the intrinsic problems of photolithography limits the applications. The low transmission and

the diffraction limit are two major problems, which boost the search for good solutions and alternative techniques. The main approach to solve the problems is reducing the working wavelength, such as using x-rays (Silverman, 1998) or extreme ultraviolet (EUV) light (Gwyn *et al.*, 1998). Their drawback is the drastic increase of complexity and cost for instrumentation (Luo and Ishihara, 2004). Another way to reduce wavelength is to use immersion photolithography (Abdo *et al.*, 2004), which replaces the air gap between the wafer and optics with higher refractive index (n) material such that the working wavelength is divided by n. But, it is really challenging to manage the filled liquid with uniform optical property and no air bubbles throughout the whole fabrication process. Other alternative techniques for nanostructure fabrication include dip-pen lithography (Piner *et al.*, 1999), electron-beam (e-beam) lithography (Groves *et al.*, 2002), and nanoimprinting (Guo, 2004). The first two alternatives suffer from slow throughput due to direct scanning, while the third one may not be appropriate for semiconductor device fabrication because of high pressure involvement. Consequently, nanolithography still holds great practical value if transmission can be both enhanced and confined in nanoscale without complicated optics. It has been shown that transmission through periodic slit/hole arrays can be enhanced not only due to surface plasmon excitation but also other mechanisms. Depending on the spectral region, enhanced transmission can be attributed to Wood's anomaly, cavity resonance, and the effective medium behavior. The transmission enhancement through nanoscale metallic slit will be studied both numerically and experimentally in the dissertation. Furthermore, in-depth understanding of EM fields and the path of energy funnels will assist the development of nanolithography as well as other optical applications.

For clearly addressing the values of periodic micro/nanostructure radiative properties in modern technologies with comprehensive background illustration, the organization of this dissertation is in the following. Chapter 2 will present numerical algorithms on which the work in subsequent chapters is based, including RCWA and effective medium formulations. Chapter 3 will demonstrate the structure profile and diffraction efficiency measurement results of both fabricated 1D and 2D silicon microstructures. Chapter 4 will present a parametrical study on both spectral and directional absorptance modeling of nanoscale patterned wafer. RCWA modeling results will be validated and employed for the assessment of effective medium formulation applicability. Chapter 5 will review micro/nanostructure devices in TPV systems and propose a kind of nanoscale periodic structures, complex gratings, as TPV radiators due to its wavelength-selective emittance. The chapter will show the originality of design as well as its spectral and directional emittance. Chapter 6 will investigate the transmittance enhancement through nanoscale slit arrays and confinement of periodic slit arrays. EM fields, energy density, and time-averaged Poynting vector will all be numerical modeled. The polarization-dependant transmittance behavior of 1D nanoscale metallic slit arrays will be experimentally exhibited. At the end, Chapter 7 will summarize the conclusions and the recommended future work.

CHAPTER 2

THEORETICAL FOUNDATIONS

This chapter gives clear definition of radiative properties for periodic structures based on their anisotropic diffraction efficiency. Coordinate and symbols for describing the diffraction are also specified here. Furthermore, this chapter illustrates all numerical algorithms in detail for 1D periodic structure. The algorithms include rigorous coupled-wave analysis (RCWA) method and three approximation methods, which are theoretical foundations of subsequent chapters. Depending on the plane of incidence (PoI) orientation and incidence polarization, the chapter presents corrected RCWA formulas for fast convergence.

2.1. Background

The spectral bidirectional reflectance ρ''_λ is defined by the ratio of the reflected intensity over the incident partial flux (Modest, 2003):

$$\rho''_\lambda(\lambda,\theta_i,\phi_i,\theta_r,\phi_r)=\frac{dI_r(\lambda,\theta_r,\phi_r)}{I_i(\lambda,\theta_i,\phi_i)\cos\theta_i\delta\Omega_i} \tag{2.1}$$

where λ is the wavelength, θ and ϕ are the zenith angle and azimuthal angle, respectively, and $\delta\Omega$ is the solid angle of the beam. In the spherical coordinates as shown in Fig. 2.1, subscripts *i* and *r* denote the incidence and reflected light, respectively. However, the subscripts for angles may not be specifically marked in other sections for clarity. dI_r is the reflected intensity in the direction of (θ_r,ϕ_r), and the denominator $I_i\cos\theta_i\delta\Omega_i$ represents the incident spectral radiation flux per unit area. Note that ρ''_λ is not the ratio

of actual reflected flux to the incident flux, and the value can be larger than one. For example, the bidirectional reflectance of a specular reflector is zero for all angles of reflection except the specular angle ($\phi_i = \phi_r + \pi$ and $\theta_i = \theta_r$), at which angle the bidirectional reflectance goes to infinity. Large or zero bidirectional reflectance does not violate the radiative energy conservation principle. On the other hand, the balance of radiative energy at an interface involves the directional-hemispherical properties. The directional-hemispherical reflectance $\rho'^{\cap}_{\lambda}$ is defined below and related to the bidirectional reflectance as (Modest, 2003):

$$\rho'^{\cap}_{\lambda}(\lambda,\theta_i,\phi_i) = \frac{\int dI_r(\lambda,\theta_r,\phi_r)\cos\theta_r d\Omega_r}{I_i(\lambda,\theta_i,\phi_i)\cos\theta_i \delta\Omega_i} = \frac{1}{\pi}\int \rho''_{\lambda}\cos\theta_r d\Omega_r \tag{2.2}$$

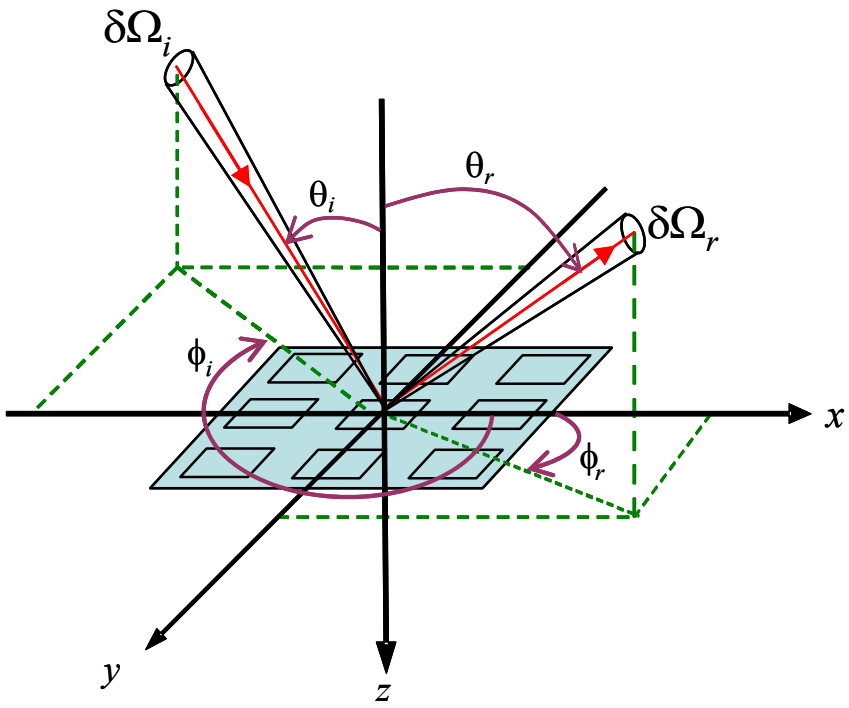

Figure 2.1 Coordinate and angles for the definition of bidirectional reflectance of periodic structure.

When the reflected energy focuses within solid angle $\delta\Omega_r$ only, such as a specular reflector, the directional-hemispherical reflectance can be simplified from Eq. (2.2) as:

$$\rho'^{\cap}_{\lambda}(\lambda,\theta_i,\phi_i)=\frac{I_r(\lambda,\theta_r,\phi_r)\cos\theta_r\delta\Omega_r}{I_i(\lambda,\theta_i,\phi_i)\cos\theta_i\delta\Omega_i} \tag{2.3}$$

For 1D gratings with period close to the wavelength, the reflected energy is limited in specific directions depending on diffraction order *j*, which is an integer. As a result, the directional-hemispherical reflectance of 1D grating can be obtained by replacing its numerator in Eq. (2.3) with energy summation of all *j*th reflected orders as below:

$$\rho'^{\cap}_{\lambda}(\lambda,\theta_i,\phi_i)=\sum_j\frac{I_{rj}(\lambda,\theta_{rj},\phi_{rj})\cos\theta_{rj}\delta\Omega_{rj}}{I_i(\lambda,\theta_i,\phi_i)\cos\theta_i\delta\Omega_i}=\sum_j\eta_{rj} \tag{2.4}$$

where η_{rj} is the *j*th order reflected diffraction efficiency and defined as the flux ratio of the *j*th order diffraction to the incidence (Petit and Botten, 1980). Note that only efficiency of propagating rays can be defined and is considered here. The directional-hemispherical transmittance $\tau'^{\cap}_{\lambda}$ and the transmitted diffraction efficiency η_{tj} can be defined in a similar way. The energy conservation connects the directional-hemispherical absorptance $\alpha'^{\cap}_{\lambda}$ with defined $\rho'^{\cap}_{\lambda}$ and $\tau'^{\cap}_{\lambda}$ in the following:

$$\alpha'^{\cap}_{\lambda}=1-\rho'^{\cap}_{\lambda}-\tau'^{\cap}_{\lambda} \tag{2.5}$$

Another radiative property, the emittance, is a ratio of the actual emissive power from a surface to that of a blackbody at the same temperature. According to the Kirchhoff's law (Siegel and Howell, 2002), the emittance equals to the absorptance. Hereafter, the directional-hemispherical radiative properties will not be explicitly expressed for simple notation. The arguments about radiative properties for 1D periodic structures are also

applicable for 2D structures; however, two integers are necessary for specifying the diffraction orders.

2.2 Effective Medium Formulations

Initially, approximation methods were proposed to model radiative properties of micro/nanostructures to provide fast calculation speed with reasonable accuracy. Some previous studies have used the method of homogenization (Raguin and Morris, 1993; Sentenac and Greffet, 1994), and the underlying physics is based on the effective medium theory (EMT) (Lalanne and Lemercier-Lalanne, 1996). The EMT may be valid when the grating period (Λ) is much shorter than the wavelength (λ) because all the diffracted waves are evanescent waves, except the zeroth order in specular direction. As a result, the radiative properties of periodic structures can be treated as a homogeneous layer with an effective dielectric function ε_{EMT}. This way, the patterned structures are simplified to planar multilayer structures, which requires much less computation time to solve the matrix equations based on thin-film optics (Raguin and Morris, 1993; Sentenac and Greffet, 1994).

The EMT was first postulated by Maxwell Garnett (1904) to obtain the effective dielectric function of metal particles embedded in a dielectric medium. The general assumption is that the space separating the particles to be sufficiently large or the filling ratio (volume fraction) of the particles to be small (Granqvist and Hunderi, 1977). Bruggeman (1935) assumed that two materials are both embedded in the effective medium and obtained an expression, which has been successfully applied to study the effect of porosity on the refractive index and absorption coefficient of different materials (Zhang *et al.*, 2003). Bruggeman's expression is often called the effective medium

approximation (EMA). The dielectric function of the effective medium ε_{EMA} is related to that of the two components by

$$f\frac{\varepsilon_{EMA}-\varepsilon_A}{\varepsilon_A+2\varepsilon_{EMA}}+(1-f)\frac{\varepsilon_{EMA}-\varepsilon_B}{\varepsilon_B+2\varepsilon_{EMA}}=0 \tag{2.6}$$

where f is the filling ratio of material A. Rytov (1956) first applied EMT for a periodic structure by treating a stratified medium as a homogeneous uniaxial crystal and obtained the effective permittivity and permeability tensors. The zeroth order is considered to be applicable when $\Lambda << \lambda$ and has been used for the design surfaces with antireflection and selective radiative properties (Glytsis and Gaylord, 1992; Sentenac and Greffet, 1994). The effective medium formulation for gratings depends on the polarization. The zeroth-order expressions are given below (Glytsis and Gaylord, 1992; Raguin and Morris, 1993; Sentenac and Greffet, 1994):

$$\varepsilon_{TE,0}=f\varepsilon_A+(1-f)\varepsilon_B \tag{2.7a}$$

$$\varepsilon_{TM,0}=\left(\frac{f}{\varepsilon_A}+\frac{1-f}{\varepsilon_B}\right)^{-1} \tag{2.7b}$$

where subscripts TE (transverse electric) and TM (transverse magnetic) indicate the polarization of the incidence. The expressions including the second-order terms are (Raguin and Morris, 1993; Lalanne and Lemercier-Lalanne, 1996):

$$\varepsilon_{TE,2}=\varepsilon_{TE,0}\left[1+\frac{\pi^2}{3}\left(\frac{\Lambda}{\lambda}\right)^2 f^2(1-f)^2\frac{(\varepsilon_A-\varepsilon_B)^2}{\varepsilon_{TE,0}}\right] \tag{2.8a}$$

$$\varepsilon_{TM,2}=\varepsilon_{TM,0}\left[1+\frac{\pi^2}{3}\left(\frac{\Lambda}{\lambda}\right)^2 f^2(1-f)^2(\varepsilon_A-\varepsilon_B)^2\varepsilon_{TE,0}\left(\frac{\varepsilon_{TM,0}}{\varepsilon_A\varepsilon_B}\right)^2\right] \tag{2.8b}$$

Notice that when $\Lambda << \lambda$ or in the case of small filling ratio, the second-order term drops out. It is hoped that the second-order correction may improve the useful range of the EMT. After the effective dielectric function is obtained, the grating region is treated as a homogeneous isotropic material for the given polarization and incidence. The transfer matrix method (Zhang *et al.*, 2003; Lee *et al.*, 2005) for calculating radiative properties of multilayer thin films is then applied to obtain the reflectance. To distinguish different formulations, EMA refers to Eq. (2.6), EMT-0 refers to Eq. (2.7) with zeroth order only, and EMT-2 refers to Eq. (2.8) with the second-order terms.

2.3 Rigorous Coupled-Wave Analysis for Transverse Electric Wave

The radiative properties of different patterned structures can be modeled with different numerical methods, such as finite element method coupled with the boundary integral method (Erofeev *et al.*, 1995), thin film optics (Hebb and Jensen, 1998), and finite-difference time-domain (FDTD) method (Liu *et al.*, 2004). However, for periodic structures, RCWA can calculate diffraction efficiencies of periodic gratings much faster than other methods by solving Maxwell's equations. Subsequently, RCWA is employed to calculate the directional-hemispherical radiative properties for periodic structures. Brief derivations for the TE wave incident on 1D gratings with the PoI perpendicular to the grating grooves are presented here.

A plane wave is obliquely incident on a 1D grating from free space, as shown in Fig. 2.2. The space is divided into three regions with different dielectric function $\varepsilon = (n + i\kappa)^2$, where n is the refractive index and κ is the extinction coefficient. Region I is air and its dielectric function is assumed to be the same as that of vacuum

($\varepsilon_{\mathrm{I}} = n_{\mathrm{I}}^2 = 1,\ \kappa_{\mathrm{I}} = 0$). Region II is a periodic grating composed of material A and B such that its dielectric function is a periodic function of *x*. The lateral extension of the gratings is assumed to be infinite with groove depth *d*, and the gating period Λ is comparable to the wavelength λ. The filling ratio of material A in a period is *f*. Region III is the substrate with dielectric function, $\varepsilon_{\mathrm{III}} = (n_{\mathrm{III}} + i\kappa_{\mathrm{III}})^2$. Conventionally, the PoI is defined by the direction of incidence and the *z*-axis. This definition results in infinite numbers of PoI at normal incidence. To remedy this drawback, the PoI is uniquely defined as *x*-*y* plane for normal incidence case. Accordingly, the PoI is in the *x*-*z* plane in Fig. 2.2 and the electric field is perpendicular to the plane of incidence (i.e. *s*-polarized or TE wave). The angle of incidence θ is the zenith angle between the wavevector and *z*-axis. **E** and **H** are the normalized incidence electric field and magnetic field with unity magnitude, respectively. Because the oscillation direction of **E** is perpendicular to *x*-*z* plane, $k_y = 0$. Besides, **E** can be expressed as $\exp\left(ik_x x + ik_z z - i\omega t\right)$ by assuming unity magnitude, where k_x and k_z are the *x*- and *z*-components of wavevector **k**, ω is the angular frequency, *t* is time. For simplicity, the time harmonic term $\exp(-i\omega t)$ will be omitted in the following. The magnitude of **k** in regions I and III can be expressed as:

$$k_{\mathrm{I}} = \frac{2\pi}{\lambda} = k \ \text{ and } \ k_{\mathrm{III}} = \frac{2\pi}{\lambda}\sqrt{\varepsilon_{\mathrm{III}}} = k\sqrt{\varepsilon_{\mathrm{III}}} \tag{2.9}$$

In region I, each different k_{xj} satisfies the Floquet condition (Moharam *et al.*, 1995a):

$$k_{xj} = \frac{2\pi}{\lambda}\sin\theta + \frac{2\pi}{\Lambda} j \tag{2.10}$$

where k_{xj} is the same in all regions. If Eq. (2.10) is divided by *k*, the well-known grating equation is obtained.

$$\sin\theta_j = \sin\theta + \frac{j\lambda}{\Lambda} \tag{2.11}$$

where jth order diffraction angle $\theta_j = \sin^{-1}(k_{xj}/k)$. If $k_{xj}^2 > k_{\mathrm{I}}^2$, $\sin\theta_j > 1$ and θ_j is not a physical property. The jth order reflected wave decays exponentially towards the negative z direction. The wave is an evanescent wave existing only in the near-field regime and the far-field diffraction efficiency is zero. However, both propagating and evanescent diffraction orders must be included in RCWA for matching boundary conditions in order to correctly predict radiative properties. Furthermore, this inclusion will allow one to study near-field effect such as absorption and energy density near the grating region.

On the other hand, the z-components of **k** for the jth order reflected diffraction is as follows:

$$k_{zj}^r = \begin{cases} \sqrt{k^2 - k_{xj}^2}, & k^2 > k_{xj}^2 \\ i\sqrt{k_{xj}^2 - k^2}, & k_{xj}^2 > k^2 \end{cases} \tag{2.12}$$

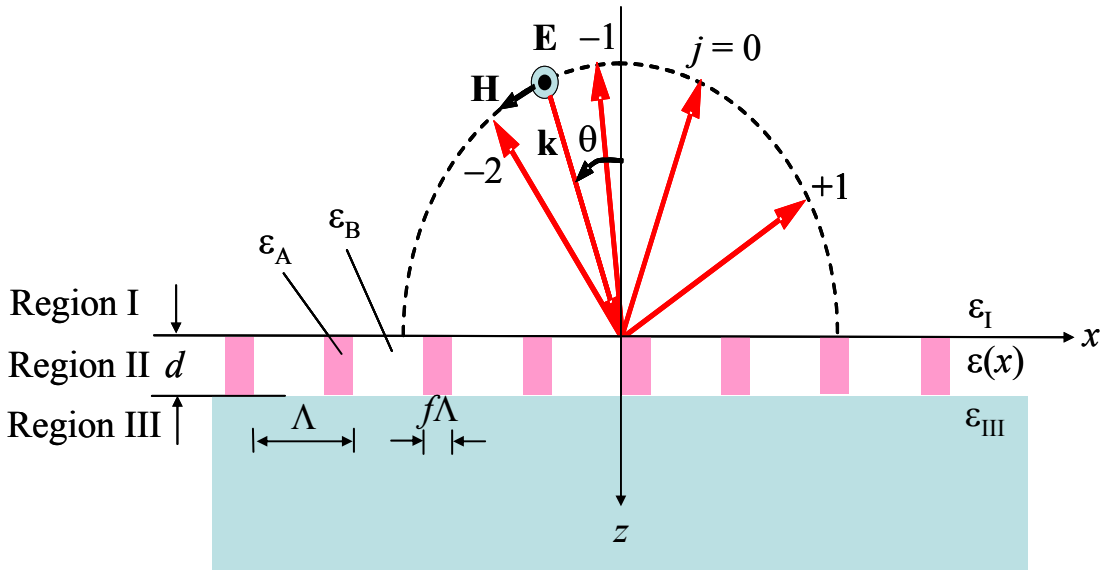

Figure 2.2 Diffraction of the TE wave on a binary grating.

where the superscript *r* is for reflection. Similar criteria can be applied to the transmitted wave *z*-component (k_{zj}^{t}) in region III. The electric field in region I is a superposition of the incident wave and the reflected waves; therefore,

$$\mathbf{E}_{\mathrm{I}}(x,z) = \exp(ik_x x + ik_z z) + \sum_j \mathbf{E}_{rj} \exp(ik_{xj} x - ik_{zj}^{r} z) \tag{2.13}$$

where E_{rj} is the amplitude of the *j*th order reflected wave. Note that E_{rj} equals to the Fresnel reflection coefficient only for this case because the amplitude of the incidence field is assumed to be unity. The normalized electric field in region III is obtained by superimposing all transmitted waves:

$$\mathbf{E}_{\mathrm{III}}(x,z) = \sum_j \mathbf{E}_{tj} \exp(ik_{xj} x + ik_{zj}^{t} z) \tag{2.14}$$

where E_{tj} is the amplitude of the *j*th order transmitted wave. Similarly, $E_{tj} = T_j$, which is the Fresnel transmission coefficient of the *j*th order only if the magnitude of incidence electric field is unity. In Region II, the electric field can be expressed as a Fourier series:

$$\mathbf{E}_{\mathrm{II}}\left(x,z\right) = \sum_j \chi_{yj}(z) \exp(ik_{xj} x)\hat{\mathbf{y}} \tag{2.15}$$

where χ_{yj} is magnitude for the *j*th space-harmonic of electric field in the grating region. The space-harmonic of component of *j*th order in region II matches the *j*th diffraction order in regions I and III. The next step is to substitute the electric fields in Region II given by Eq. (2.15) into Maxwell's equation ($\nabla \times \mathbf{H}_{\mathrm{II}} + i\omega\varepsilon_0 \varepsilon(x)\mathbf{E}_{\mathrm{II}} = 0$) to express in the form of electric field, where ε_0 is the electric permittivity of vacuum:

$$E_{\mathrm{II},y} = \frac{i}{\omega\varepsilon_0 \varepsilon(x)} \left(\frac{\partial H_{\mathrm{II},x}}{\partial z} - \frac{\partial H_{\mathrm{II},z}}{\partial x} \right) \tag{2.16}$$

Furthermore, the two partial derivatives of magnetic field component can also be expressed by the electric field using $\nabla \times \mathbf{E}_{\mathrm{II}} - i\omega\mu_0 \mathbf{H}_{\mathrm{II}} = 0$ such that the electric field in region II should satisfy equations below, where μ_0 is the magnetic permeability of vacuum:

$$-k^2 E_{\mathrm{II},y} = \frac{1}{\varepsilon(x)}\left[\frac{\partial}{\partial x}\left(\frac{\partial E_{\mathrm{II},y}}{\partial x}\right) + \frac{\partial}{\partial z}\left(\frac{\partial E_{\mathrm{II},y}}{\partial z}\right)\right] \tag{2.17}$$

The key is for RCWA is to arrange Maxwell's equations into a summation of $\exp(ik_{xj}x)$ and then set its coefficients to zero for each j. Hence, the above equation is an infinite set of second-order coupled equations while each space-harmonic term is coupled with other components through the multiplication of two Fourier series. However, the summation should be truncated such that the equations can be numerically solved. When approximate the infinite summation with the truncated finite-summation, it is necessary to follow theorems of Fourier Factorization (Li, 1996) to guarantee that the approximation properly converges to the original infinite summation.

Though the theorems are for general purpose, the important parts applicable for RCWA are explicitly explained here. First of all, the product of two functions should be classified into three types:

1. A product of type 1 is from the multiplication of two piecewise-smooth, bounded, periodic functions, that have no concurrent jump discontinuities.
2. A product of type 2 is from the multiplication of two piecewise-smooth, bounded, periodic functions, that only have pairwise-complementary jump discontinuities.

3. A product of type 3 is from the multiplication of two piecewise-smooth, bounded, periodic functions, that have concurrent but not complementary jump discontinuities.

For RCWA, only products of type 1 and type 2 show up in the coupled equations such that their Fourier series are discussed here. For the product of type 1 and type 2, the function should Fourier factorized by Laurent's rule and the inverse rule, respectively. Their mathematical expressions are briefly described. For two piecewise-smooth, bounded, periodic functions of x, $f(x)$ and $g(x)$, with period 2π, their product $h(x) = f(x)g(x)$ is also a piecewise-smooth, bounded, periodic functions of x. The Fourier expansion series of $f(x)$ and $g(x)$ and their inverse can be expressed below:

$$f(x) = \sum_{m=-\infty}^{m=\infty} f_m^{ord} \exp(imx) \text{ and } \frac{1}{f(x)} = \sum_{m=-\infty}^{m=\infty} f_m^{inv} \exp(imx) \tag{2.18a}$$

$$g(x) = \sum_{m=-\infty}^{m=\infty} g_m^{ord} \exp(imx) \text{ and } \frac{1}{g(x)} = \sum_{m=-\infty}^{m=\infty} g_m^{inv} \exp(imx) \tag{2.18b}$$

where the superscript *ord* and *inv* represent ordinary and inverse, respectively. In order to obtain the truncated Fourier series of $h(x)$, a superscript M is enclosed to denote the symmetrically truncated partial summations. That is, the truncated Fourier series is expressed below

$$h^{(M)}(x) = \sum_{m=-M}^{m=M} h_n^{(M)} \exp(inx) \tag{2.19}$$

According to Laurent's rule, the Fourier coefficients of the truncated matrix should be expressed as:

$$h_n^{(M)} = \sum_{m=-M}^{m=M} f_{n-m}^{ord} g_m^{ord} \tag{2.20}$$

But when the inverse rule is valid and applied, the Fourier coefficients of the truncated matrix should be expressed as:

$$h_n^{(M)} = \sum_{m=-M}^{m=M} (f_{n-m}^{inv})^{-1} g_m^{ord} \tag{2.21}$$

The two rules should be applied to RCWA calculation with caution to get fast convergence. For example, $-k^2 E_{\mathrm{II},y}$ is a continuous function while $1/\varepsilon(x)$ has jump discontinuities at the interface between material A and B while. As a result, the right hand side of Eq. (2.17) must be the product of type II, which only have pairwise-complementary jump discontinuities. In this case, the product of the two functions should be factorized by inverse rule. Consequently, the Fourier coefficients of the inverse of one function with those of the ordinary of the other function are necessary and sufficient to express the product of them in Fourier series. Here, the inverse of the function $1/\varepsilon(x)$, which is the ordinary of the dielectric function, is expanded as a Fourier series below:

$$\varepsilon^{ord}(x) = \varepsilon(x) = \sum_p \varepsilon_p^{ord} \exp\left(i \frac{2p\pi}{\Lambda} x \right),\ p = 0, \pm 1, \pm 2, \ldots \tag{2.22}$$

where ε_p^{ord} is the pth Fourier coefficient for the ordinary of $\varepsilon(x)$ that is given by

$$\varepsilon_0^{ord} = f\varepsilon_{\mathrm{A}} + (1-f)\varepsilon_{\mathrm{B}} \text{ and } \varepsilon_p^{ord} = \frac{(\varepsilon_{\mathrm{A}} - \varepsilon_{\mathrm{B}})\sin(pf\pi)}{p\pi} \ (p \neq 0) \tag{2.23}$$

for rectangular gratings shown in Fig. 2.2 with f being the filling ratio of material A. Each ε_p^{ord} is not a physical property of the material and its imaginary part may be negative for a passive medium.

After the inverse rule is applied to Eq. (2.17), the coupled-wave equations can be rearranged in terms of the jth order in $\exp(ik_{xj}x)$ as follows:

$$\sum_j \left(\frac{\partial^2 \chi_{yj}}{\partial z^2} - k_{xj}^2 \chi_{yj} + k^2 \sum_p \varepsilon_{j-p}^{ord} \chi_{yp} \right) \exp(ik_{xj}x) = 0 \tag{2.24}$$

where the coefficients should be zero. Sufficient number of space-harmonic terms $(N = 2q+1)$ should be used for modeling accuracy, and the number should match diffraction orders such that the equations can be expressed in the matrix form as follows:

$$\frac{1}{k^2}\left[\frac{\partial^2 \mathbf{X}^Y}{\partial z^2}\right] = \left[\mathbf{K}^X \mathbf{K}^X - \mathbf{E}\right]\left[\mathbf{X}^Y\right] \tag{2.25}$$

where $\mathbf{X}^Y$ is column vectors formed by χ_{yj}. Note that $\mathbf{K}^X$ is diagonal matrices with the elements $K_{l,l}^X = k_{xj}/k$, where $j = l - q - 1$. Furthermore, $\mathbf{E}$ is the Toeplitz matrices (Li, 1996) generated by the Fourier coefficients of the dielectric function such that $E_{l,m} = \varepsilon_p^{ord}$, where $p = l - m$, and the size of all matrices is $N \times N$. Accordingly, the solutions of χ_{yj} can be expressed by the eigenvalue and eigenvectors of the matrices given by

$$\chi_{yj}(z) = \sum_{l=1}^{N} V_{j,l}^A \left[C_l^{A+} e^{k\xi_l (z-d)} + C_l^{A-} e^{-k\xi_l z} \right] \tag{2.26}$$

where $V_{j,l}^A$ is the elements of the matrices $\mathbf{V}^A$, and it is composed of the eigenvector corresponding to the eigenvalue for the matrix $\mathbf{K}^X \mathbf{K}^X - \mathbf{E}$. The exponential terms in Eq. (2.26) originate from the forward and backward coupled diffracted waves in Region II. Here, C's are their unknown coefficients with superscripts + and –, which signify forward and backward waves. Note that ξ_l is the element of diagonal matrix $\mathbf{Q}$, which are the positive square roots of the eigenvalue for the matrix $\mathbf{K}^X \mathbf{K}^X - \mathbf{E}$.

The magnetic field in grating region can be expressed as:

$$\mathbf{H}_{\mathrm{II}}(x,z) = i\frac{k}{\mu_0\omega}\sum_j [\gamma_{xj}(z)\hat{\mathbf{x}} + \gamma_{zj}(z)\hat{\mathbf{z}}]\exp(ik_{xj}x) \tag{2.27}$$

where γ_{xj} and γ_{zj} are the x- and z-vector component for the jth space-harmonic of electric field in the grating region. The x-component is further expressed in the following:

$$\gamma_{xj}(z) = \sum_{l=1}^{N} W_{j,l}^{A}\left[C_l^{A+}e^{k\xi_l(z-d)} + C_l^{A-}e^{-k\xi_l z}\right] \tag{2.28}$$

where $\mathbf{W}_{j,l}^{A} = \mathbf{Q}\mathbf{V}_{j,l}^{A}$. In order to obtain diffraction efficiencies in regions I, II, and III, one needs to solve for $4N$ (C_l^{A+}, C_l^{A-}, E_{rj}, and E_{tj}) unknown coefficients. Here, $4N$ equations are provided by boundary conditions that the tangential components of the electric and magnetic fields are continuous at region boundaries ($z = 0$ and $z = d$). Furthermore, the field components are consistent for all x once the boundary conditions are satisfied at $x = 0$. Subsequently, the boundary conditions at $z = 0$ are:

$$E_{\mathrm{I}} = E_{\mathrm{II}} \rightarrow \delta_{j0} + E_{rj} = \sum_{l=1}^{N} V_{j,l}^{A}\left[C_l^{A+}e^{-k\xi_l d} + C_l^{A-}\right] \tag{2.29a}$$

$$H_{\mathrm{I},x} = H_{\mathrm{II},x} \rightarrow i\left[\cos\theta\cdot\delta_{j0} - \frac{k_{zj}^{r}}{k}E_{rj}\right] = \sum_{l=1}^{N} W_{j,l}^{A}\left[C_l^{A+}e^{-k\xi_l d} + C_l^{A-}\right] \tag{2.29b}$$

where δ_{j0} is Kronecker delta with $\delta_{j0} = 1$ for $j = 0$ and $\delta_{j0} = 0$ for $j \neq 0$. On the other hand, the boundary conditions at $z = d$ are:

$$E_{\mathrm{II}} = E_{\mathrm{III}} \rightarrow \sum_{l=1}^{N} V_{j,l}^{A}\left[C_l^{A+} + C_l^{A-}e^{-k\xi_l d}\right] = E_{tj} \tag{2.30a}$$

$$H_{\mathrm{II},x} = H_{\mathrm{III},x} \rightarrow \sum_{l=1}^{N} W_{j,l}^{A}\left[C_l^{A+} - C_l^{A-}e^{-k\xi_l d}\right] = i\left(\frac{k_{\mathrm{III},zj}}{k}\right)E_{tj} \tag{2.30b}$$

After the unknowns are solved, the diffraction efficiencies for *j*th order reflected wave and transmitted wave can be obtained by its time-averaged Poynting vector:

$$\eta_{rj} = E_{rj}E_{rj}^{*}\mathrm{Re}\left(\frac{k_{zj}^{r}}{k\cos\theta}\right) \text{ and } \eta_{tj} = E_{tj}E_{tj}^{*}\mathrm{Re}\left(\frac{k_{zj}^{t}}{k\cos\theta}\right) \tag{2.31}$$

where the asterisk is the conjugate of a complex number.

2.4 Rigorous Coupled-Wave Analysis for Transverse Magnetic Wave

For the TM wave incident on 1D structures with the PoI perpendicular to the gratings, the magnetic field is perpendicular to the PoI. That is, the oscillation direction of **E** and **H** are switched with **H** pointing into the PoI (i.e. *p*-polarized or TM wave). The magnetic field in region I is expressed as superposition of the incident wave and the reflected waves; therefore,

$$\mathbf{H}_{\mathrm{I}}(x,z) = \exp(ik_x x + ik_z z) + \sum_j \mathbf{H}_{rj}\exp(ik_{xj}x - ik_{zj}^{r}z) \tag{2.32}$$

H_{rj} is the amplitude of the *j*th order reflected wave magnetic field normalized to the incidence. The *x*- and *z*-components (k_x and k_z) of the wavevector are the same as defined for TE waves. Note that the incidence magnetic field magnitude is assumed to be unity such that H_{rj} equals to R_j, which is the Fresnel reflection coefficient. The normalized magnetic field in region III is the superposition of all transmitted wave and expressed as:

$$\mathbf{H}_{\mathrm{III}}(x,z) = \sum_j \mathbf{H}_{tj}\exp(ik_{xj}x + ik_{zj}^{t}z) \tag{2.33}$$

where H_{tj} is the amplitude of the *j*th order transmitted wave. The normalized magnetic field in region II:

$$\mathbf{H}_{\mathrm{II}}(x,z)=\sum_{j}\gamma_{yj}(z)\exp(ik_{xj}x)\hat{\mathbf{y}} \tag{2.34}$$

where $\gamma_{yj}(z)$ is the amplitude for the *j*th space-harmonic of magnetic field in the grating region. From the Maxwell's equation ($\nabla\times\mathbf{E}_{\mathrm{II}}-i\omega\mu_0\mathbf{H}_{\mathrm{II}}=0$), the magnetic field (only *y*-component existing) can be expressed in the form of electric field:

$$H_{\mathrm{II}}=H_{\mathrm{II},y}=\frac{i}{\omega\mu_0}\left(\frac{\partial E_{\mathrm{II},z}}{\partial x}-\frac{\partial E_{\mathrm{II},x}}{\partial z}\right) \tag{2.35}$$

where the two partial derivatives of electric field components can also be expressed by the magnetic field $\nabla\times\mathbf{H}_{\mathrm{II}}+i\omega\varepsilon_0\varepsilon(x)\mathbf{E}_{\mathrm{II}}=0$, such that the magnetic field in region II should satisfy equations below:

$$\frac{\partial}{\partial z}\left(\frac{\partial H_{\mathrm{II},y}}{\partial z}\right)=-\varepsilon(x)\left\{\frac{\partial}{\partial x}\left[\frac{1}{\varepsilon(x)}\left(\frac{\partial H_{\mathrm{II},y}}{\partial x}\right)\right]+k^2H_{\mathrm{II},y}\right\} \tag{2.36}$$

where the left side of Eq. (2.36) is a continuous function while $\varepsilon(x)$ has jump discontinuities at the interface between material A and B. As a result, the right hand side must be the product of type 2, which only have pairwise-complementary jump discontinuities. Based on the inverse rule, the Fourier coefficients of the inverse of one function with those of the ordinary of the other function are necessary and sufficient to express the product of them in Fourier series. Here, the inverse of the function $\varepsilon(x)$, which is $1/\varepsilon(x)$, is expanded as a Fourier series below:

$$\varepsilon^{inv}(x)=\frac{1}{\varepsilon(x)}=\sum_{p}\varepsilon_p^{inv}\exp\left(i\frac{2p\pi}{\Lambda}x\right) \tag{2.37}$$

where ε_p^{inv} is the *p*th Fourier coefficient for the inverse of $\varepsilon(x)$ and not a physical property for passive medium also. Caution must be taken because $\varepsilon_p^{inv}\neq 1/\varepsilon_p^{ord}$ for most cases.

On the other hand, one should be careful as well when handing the Fourier series of the terms in the brace at the right side of Eq. (2.36). Since the whole terms in the brace should have the complementary discontinuities for $\varepsilon(x)$ and its second term $k^2 H_{\mathrm{II},y}$ is a continuous function, its first term must have the complementary discontinuities. However, the term inside the square bracket for partial derivative should be a continuous function as a product of type 2 because the term originates from $E_{\mathrm{II},z}$ and $1/\varepsilon(x)$ has discontinuity. Hence, the inverse of the function $1/\varepsilon(x)$, which is the ordinary of the dielectric function, is used. Failure of correctly Fourier factorizing functions can result in slow convergence and even erroneous solutions. Consequently, Eq. (2.36) can be rearranged in terms of *j*th order in $\exp(ik_{xj}x)$ as follows:

$$\sum_j \left(\sum_p \varepsilon_{j-p}^{inv} \frac{\partial^2 \gamma_{yp}}{\partial z^2} - \sum_p k_{xj} \left\| \varepsilon^{ord} \right\|_{j,p}^{-1} k_{xp} \gamma_{yp} + k^2 \gamma_{yj} \right) \exp(ik_{xj}x) = 0 \tag{2.38}$$

where $\left\| \varepsilon^{ord} \right\|^{-1}$ is the inverse of matrix **E**, (i.e., $\mathbf{E}^{-1}$). Similar to equations for TE waves, Eq. (2.38) can also be expressed in the matrix form as shown in Eq. (2.39) and be solved.

$$\frac{1}{k^2}\left[\frac{\partial^2 \mathbf{\Gamma}^Y}{\partial z^2}\right] = \left[\mathbf{M}^{-1}(\mathbf{K}^X \mathbf{E}^{-1} \mathbf{K}^X - \mathbf{I})\right]\left[\mathbf{\Gamma}^Y\right] \tag{2.39}$$

where $\mathbf{\Gamma}^Y$ is column vectors formed by γ_{yj} and **M** is the Toeplitz matrices (Li, 1996) generated by the Fourier coefficients of the inverse of dielectric function such that $M_{l,m} = \varepsilon_p^{inv}$, where $p = l - m$. **I** is the unit matrix and matrices $\mathbf{K}^X$ and **E** are previously defined. After substituting the boundary conditions, the diffraction efficiencies of the gratings can be solved.

Though 1D grating geometry is not limited to a binary profile, the RCWA is capable of calculating the diffraction efficiencies for other complicated 1D periodic structures. In fact, any periodic profile can be divided into multiple slices, which are parallel to the substrate. If each slice is thin enough, the modeling results of radiative properties are close to those of the original shape. In order to extend the RCWA to multilayered gratings, an enhanced transmittance matrix approach was proposed (Moharam *et al.*, 1995b). The key of the transmittance matrix approach is to solve equations in matrix form by matching the tangential electric and magnetic components at all boundaries between regions. Except the first and last regions, periodic dielectric functions in other regions can be composed of different materials as well as filling ratios. After obtaining the Fresnel reflection and transmission coefficients, one can calculate the diffraction efficiencies and radiative properties of periodic structures.

2.5 Rigorous Coupled-Wave Analysis for Conical Diffraction

When the PoI is not perpendicular to the grating grooves, diffracted waves do not lie in the PoI except the zeroth order, and all the reflected waves lie on a conical surface (i.e., conical diffraction), whose center line is parallel to the grating grooves (Moharam *et al.*, 1995a). Similarly, all the transmitted waves also lie on the surface of another cone with a radius depending on the refractive index of the medium. Since most RCWA formulations for conical diffraction (Han *et al.*, 1992; Moharam *et al.*, 1995a; Peng and Morris, 1995) were not modified according to Li's work (1996), the modified equations are summarized below.

Figure 2.3 shows a plane wave with wavevector **k** incident on a binary grating with a little tilt in the view angle. The direction of incident wave is expressed by the

azimuthal angle (ϕ) and the zenith angle (θ). For conical diffraction, the PoI is defined by the z-axis and the vector $(\cos\phi, \sin\phi, 0)$. In practice, it is convenient to define the PoI for normal incidence by setting $\sin\phi = 0$. This way, the PoI is perpendicular to the grooves and consistent as the PoI defined for the TE and TM wave incidence earlier. For linearly polarized incident wave, the polarization status is determined by ψ, which is the angle between the electric field vector and the PoI, as shown in Fig. 2.3. In Region I, after omitting the time harmonic term $\exp(-i\omega t)$, the normalized incident electric-field vector $\mathbf{E}$ is given by:

$$\mathbf{E} = \mathbf{E}_i \exp\left(ik_x x + ik_y y + ik_z z\right) \tag{2.40}$$

where $\mathbf{E}_i$ is the incident electric field vector at the origin, and the components of the incident wavevector are given by $k_x = k\sin\theta\cos\phi$, $k_y = k\sin\theta\sin\phi$, and $k_z = k\cos\theta$. The incidence electric field can be normalized so that the unit vector $\mathbf{E}_i$ is expressed as follows:

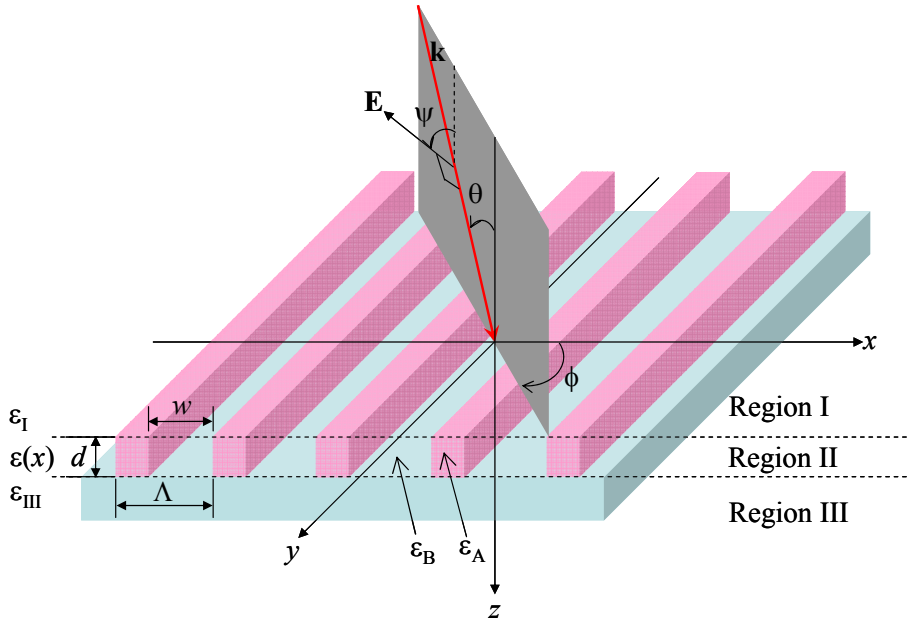

Figure 2.3 Conical diffraction on a binary grating.

$$\begin{aligned}\mathbf{E}_i = &\left(\cos\psi\cos\theta\cos\phi - \sin\psi\sin\phi\right)\hat{\mathbf{x}} \\ &+\left(\cos\psi\cos\theta\sin\phi + \sin\psi\cos\phi\right)\hat{\mathbf{y}} - \cos\psi\sin\theta\,\hat{\mathbf{z}}\end{aligned} \tag{2.41}$$

According to the Bloch-Floquet condition again, the wavevector components of the *j*th diffraction order in Region I are given by

$$k_{xj} = \frac{2\pi}{\lambda}\sin\theta\cos\phi + \frac{2\pi}{\Lambda}j \tag{2.42a}$$

$$k_y = \frac{2\pi}{\lambda}\sin\theta\sin\phi \tag{2.42b}$$

$$k_{zj}^r = \begin{cases}\sqrt{k^2 - k_{xj}^2 - k_y^2}, & k^2 > k_{xj}^2 + k_y^2 \\ i\sqrt{k_{xj}^2 + k_y^2 - k^2}, & k_{xj}^2 + k_y^2 > k^2\end{cases} \tag{2.42c}$$

As required by the phase-matching condition, the parallel components of wavevector k_{xj} and k_y must be the same for the diffracted waves in all three regions. The reflected and the transmitted wavevectors are denoted by $\mathbf{k}_{rj} = (k_{xj}, k_y, k_{zj}^r)$ and $\mathbf{k}_{tj} = (k_{xj}, k_y, k_{zj}^t)$, respectively. For transmitted diffraction, k_{zj}^r can be replaced in the same way as k_{zj}^t that in Eq. (2.42c) except substituting $k_{\mathrm{III}} = k\sqrt{\varepsilon_{\mathrm{III}}}$ for k .

Figure 2.4 shows the wavevectors of the incident wave and diffracted waves in 3D *k*–space and their projections on the $k_x - k_z$ plane. Note that the wavevector magnitude for incident and refracted waves (medium 1) is k. The wavevector magnitude for the transmitted waves is k_{III}, which is assumed to be greater than *k*. From Eq. (2.42b), the *y*-component of the wavevector is the same for all diffraction orders. Hence, the wavevectors for all diffracted wavevectors end on the semi-circles, which are intersects of the plane $k_y = (2\pi/\lambda)\sin\theta\sin\phi$ and hemispherical surfaces in each half plane.

Talking $k_z < 0$ or Region I for example, all the reflected waves lie on a half-conical surface, as illustrated in Fig. 2.4a for conical diffraction. Furthermore, the *x*-components of the wavevectors vary by multiples of $2\pi/\Lambda$ according to Eq. (2.42a). The dashed vertical lines in Fig. 2.4b indicate $2\pi/\Lambda$ difference in k_x among adjacent diffraction orders. For higher diffraction orders, the *z*-component of the wavevector becomes purely imaginary, such that the diffracted waves are evanescent. If the PoI is perpendicular to the gratings, then, both $\sin\phi$ and k_y become zero; subsequently, all the reflected and transmitted diffraction rays lie in the same plane as the PoI.

The electric field in Regions I and III can be expressed as

$$\mathbf{E}_{\mathrm{I}}(x,y,z) = \mathbf{E}_i \exp\left(ik_x x + ik_y y + ik_z z\right) + \sum_j \mathbf{E}_{rj} \exp\left(ik_{xj} x + ik_y y - ik_{zj}^r z\right) \quad (2.43a)$$

$$\mathbf{E}_{\mathrm{III}}(x,y,z) = \sum_j \mathbf{E}_{tj} \exp\left(ik_{xj} x + ik_y y + ik_{zj}^t z\right) \quad (2.43b)$$

where $\mathbf{E}_{rj} = (E_{xj}^r, E_{yj}^r, E_{zj}^r)$ and $\mathbf{E}_{tj} = (E_{xj}^t, E_{yj}^t, E_{zj}^t)$. The magnetic fields in Regions I and III can be obtained from Maxwell's equation, $\nabla \times \mathbf{E} - i\omega\mu_0 \mathbf{H} = 0$ where μ_0 is the magnetic permeability of vacuum. In Region II, the electric and magnetic fields can be expressed as a Fourier series:

$$\mathbf{E}_{\mathrm{II}}(x,y,z) = \sum_j \left[\chi_{xj}(z)\,\hat{\mathbf{x}} + \chi_{yj}(z)\,\hat{\mathbf{y}} + \chi_{zj}(z)\,\hat{\mathbf{z}}\right] \exp\left(ik_{xj} x + ik_y y\right) \quad (2.44a)$$

$$\mathbf{H}_{\mathrm{II}}(x,y,z) = i\sqrt{\frac{\varepsilon_0}{\mu_0}} \sum_j \left[\gamma_{xj}(z)\,\hat{\mathbf{x}} + \gamma_{yj}(z)\,\hat{\mathbf{y}} + \gamma_{zj}(z)\,\hat{\mathbf{z}}\right] \exp\left(ik_{xj} x + ik_y y\right) \quad (2.44b)$$

where χ_{xj}, χ_{yj}, and χ_{zj} are the vector components for the *j*th space-harmonic electric field, and γ_{xj}, γ_{yj}, and γ_{zj} are the vector components for the *j*th space-harmonic

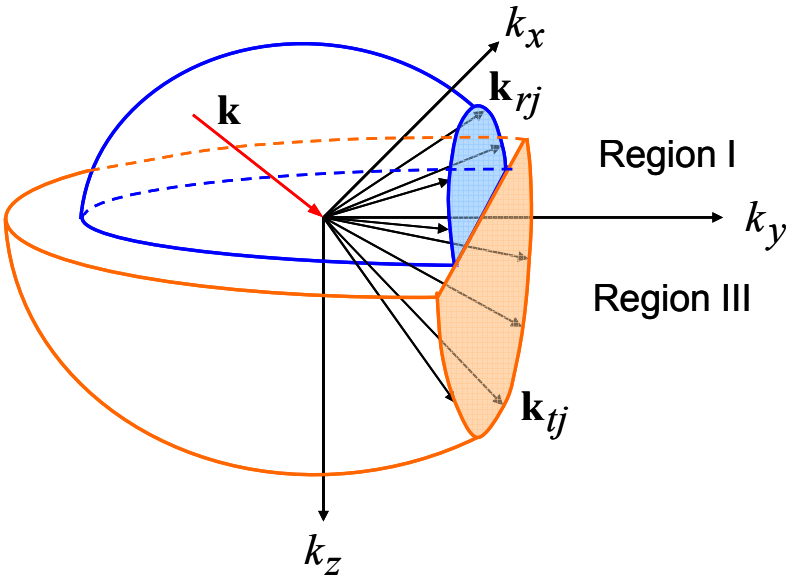

(a) 3D *k*-space

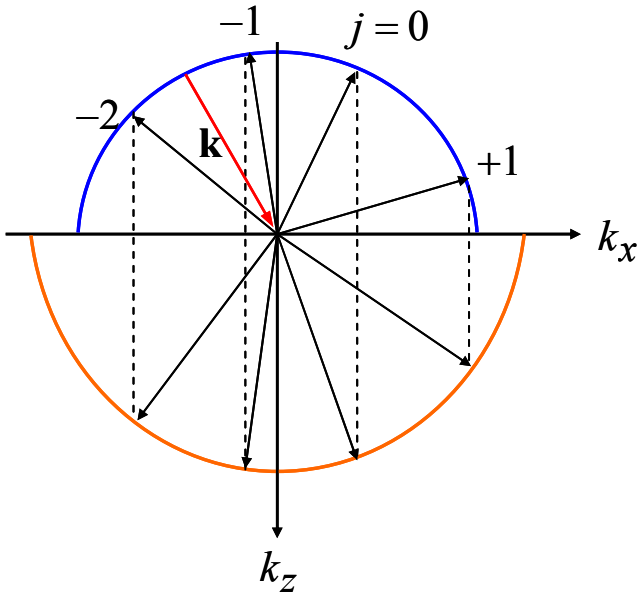

(b) Projected to k_x–k_z plane

Figure 2.4 Illustrations of a conical diffraction from a 1D grating in: (a) 3D *k*-space; (b) projected to the $k_x - k_z$ plane.

magnetic field in the grating region. The next step is to substitute the electric and magnetic fields given in Eqs. (2.44a) and (2.44b), respectively, into Maxwell's equations in Region II: $\nabla \times \mathbf{E}_{\mathrm{II}} - i\omega\mu_0 \mathbf{H}_{\mathrm{II}} = 0$ and $\nabla \times \mathbf{H}_{\mathrm{II}} + i\omega\varepsilon_0 \varepsilon(x) \mathbf{E}_{\mathrm{II}} = 0$. The key is to arrange Maxwell's equations into a summation of $\exp(ik_{xj}x + ik_y y)$ and set its coefficients to zero for every j. However, one must be cautious when factorizing $\exp(ik_{xj}x + ik_y y)$ because both $\varepsilon^{ord}(x)$ and $\varepsilon^{inv}(x)$ are Fourier expansions of $\exp(ik_{xj}x)$. The mathematical theorems emphasized by Li (1996) must be properly applied during the process. Detail solution process is listed below:

$$H_{\mathrm{II}} = \frac{i}{\omega\mu_0}\left[\left(\frac{\partial E_{\mathrm{II},y}}{\partial z} - \frac{\partial E_{\mathrm{II},z}}{\partial y}\right)\hat{\mathbf{x}} + \left(\frac{\partial E_{\mathrm{II},z}}{\partial x} - \frac{\partial E_{\mathrm{II},x}}{\partial z}\right)\hat{\mathbf{y}} + \left(\frac{\partial E_{\mathrm{II},x}}{\partial y} - \frac{\partial E_{\mathrm{II},y}}{\partial x}\right)\hat{\mathbf{z}}\right] \quad (2.45a)$$

$$E_{\mathrm{II}} = \frac{i}{\omega\varepsilon_0\varepsilon(x)}\left[\left(\frac{\partial H_{\mathrm{II},z}}{\partial y} - \frac{\partial H_{\mathrm{II},y}}{\partial z}\right)\hat{\mathbf{x}} + \left(\frac{\partial H_{\mathrm{II},x}}{\partial z} - \frac{\partial H_{\mathrm{II},z}}{\partial x}\right)\hat{\mathbf{y}} + \left(\frac{\partial H_{\mathrm{II},y}}{\partial x} - \frac{\partial H_{\mathrm{II},x}}{\partial y}\right)\hat{\mathbf{z}}\right] \quad (2.45b)$$

The x-component of magnetic field can be expressed by substituting the z-component of Eq. (2.45b) into Eq. (2.45a) to obtain:

$$H_{\mathrm{II},x} = -\frac{i}{\omega\mu_0}\left\{\frac{i}{\omega\varepsilon_0}\frac{1}{\varepsilon(x)}\left[\frac{\partial}{\partial y}\left(\frac{\partial H_{\mathrm{II},y}}{\partial x} - \frac{\partial H_{\mathrm{II},x}}{\partial y}\right)\right] - \frac{\partial E_{\mathrm{II},y}}{\partial z}\right\} \quad (2.46a)$$

Similarly, the y-component of the magnetic field as well as x and y-components of the electric filed can be obtained as below:

$$H_{\mathrm{II},y} = -\frac{i}{\omega\mu_0}\left\{\frac{\partial E_{\mathrm{II},x}}{\partial z} - \frac{i}{\omega\varepsilon_0}\frac{\partial}{\partial x}\left[\frac{1}{\varepsilon(x)}\left(\frac{\partial H_{\mathrm{II},y}}{\partial x} - \frac{\partial H_{\mathrm{II},x}}{\partial y}\right)\right]\right\} \quad (2.46b)$$

$$E_{\mathrm{II},x} = \frac{i}{\omega\varepsilon_0}\frac{1}{\varepsilon(x)}\left\{-\frac{i}{\omega\mu_0}\left[\frac{\partial}{\partial y}\left(\frac{\partial E_{\mathrm{II},y}}{\partial x} - \frac{\partial E_{\mathrm{II},x}}{\partial y}\right)\right] - \frac{\partial H_{\mathrm{II},y}}{\partial z}\right\} \quad (2.46c)$$

$$E_{\mathrm{II},y} = \frac{i}{\omega\varepsilon_0}\frac{1}{\varepsilon(x)}\left\{\frac{\partial H_{\mathrm{II},x}}{\partial z} + \frac{i}{\omega\mu_0}\left[\frac{\partial}{\partial x}\left(\frac{\partial E_{\mathrm{II},y}}{\partial x} - \frac{\partial E_{\mathrm{II},x}}{\partial y}\right)\right]\right\} \tag{2.46d}$$

Therefore, z-component of electromagnetic fields can be replaced by the x- and y-components. Equations (2.46) can be rearranged into Eq. (2.47) below:

$$-i\omega\varepsilon_0\frac{\partial E_{\mathrm{II},y}}{\partial z} = \frac{1}{\varepsilon(x)}\left[\frac{\partial}{\partial y}\left(\frac{\partial H_{\mathrm{II},y}}{\partial x} - \frac{\partial H_{\mathrm{II},x}}{\partial y}\right) - i\omega\varepsilon_0^2\mu_0\varepsilon(x)H_{\mathrm{II},x}\right] \tag{2.47a}$$

$$i\omega\mu_0 H_{\mathrm{II},y} = \frac{\partial E_{\mathrm{II},x}}{\partial z} - \frac{i}{\omega\varepsilon_0}\frac{\partial}{\partial x}\left[\frac{1}{\varepsilon(x)}\left(\frac{\partial H_{\mathrm{II},y}}{\partial x} - \frac{\partial H_{\mathrm{II},x}}{\partial y}\right)\right] \tag{2.47b}$$

$$\frac{\partial H_{\mathrm{II},y}}{\partial z} = i\omega\varepsilon_0\varepsilon(x)E_{\mathrm{II},x} - \frac{i}{\omega\mu_0}\left[\frac{\partial}{\partial y}\left(\frac{\partial E_{\mathrm{II},y}}{\partial x} - \frac{\partial E_{\mathrm{II},x}}{\partial y}\right)\right] \tag{2.47c}$$

$$-i\omega\varepsilon_0 E_{\mathrm{II},y} = \frac{1}{\varepsilon(x)}\left[\frac{\partial H_{\mathrm{II},x}}{\partial z} + \frac{i}{\omega\mu_0}\frac{\partial}{\partial x}\left(\frac{\partial E_{\mathrm{II},y}}{\partial x} - \frac{\partial E_{\mathrm{II},x}}{\partial y}\right)\right] \tag{2.47d}$$

where the left side terms are continuous functions. Before expressing them in matrix form, careful determination of the function product type following the mathematical theorems is necessary. Note that $E_{\mathrm{II},y}$, $H_{\mathrm{II},y}$, $E_{\mathrm{II},z}$, $H_{\mathrm{II},z}$, $\partial E_{\mathrm{II},y}/\partial z$, and $\partial H_{\mathrm{II},y}/\partial z$ are continuous with respect to x. However, $\varepsilon(x)$ and $1/\varepsilon(x)$ have jump discontinuities at the interface between materials A and B.

For example, the right side term is a product of type 2 in Eq. (2.47a). Since $1/\varepsilon(x)$ is not continuous, $\frac{\partial}{\partial y}\left(\frac{\partial H_{\mathrm{II},y}}{\partial x} - \frac{\partial H_{\mathrm{II},x}}{\partial y}\right) - i\omega\varepsilon_0^2\mu_0\varepsilon(x)H_{\mathrm{II},x}$ should have pair-wise complementary jump discontinuities coming from $\varepsilon(x)H_{\mathrm{II},x}$, which is a product of type 1. In this case, the product of the two functions should be factorized by Laurent's rule. As a result, the Fourier coefficients of the ordinary of two functions are necessary and

sufficient to express the product of them in Fourier series. That is, matrices $\mathbf{E}^{-1}$ and $\mathbf{E}$ should be used for $1/\varepsilon(x)$ and $\varepsilon(x)$ in Eq. (2.47a), respectively, matrix equation form. For Eq. (2.47b), $\frac{1}{\varepsilon(x)}\left(\frac{\partial H_{\mathrm{II},y}}{\partial x}-\frac{\partial H_{\mathrm{II},x}}{\partial y}\right)$ is type 2 such that $\mathbf{E}^{-1}$ is used for $1/\varepsilon(x)$. Similarly, $\varepsilon(x)E_{\mathrm{II},x}$ is type 2 such that $\mathbf{M}^{-1}$ is used for $\varepsilon(x)$ in Eq. (2.47c). For Eq. (2.47d), $\frac{1}{\varepsilon(x)}\left[\frac{\partial H_{\mathrm{II},x}}{\partial z}+\frac{i}{\omega\mu_0}\frac{\partial}{\partial x}\left(\frac{\partial E_{\mathrm{II},y}}{\partial x}-\frac{\partial E_{\mathrm{II},x}}{\partial y}\right)\right]$ is type 2 such that $\mathbf{E}^{-1}$ is used for $1/\varepsilon(x)$. Consequentially, Eq. (2.47) can be reformatted in the matrix form as below after some tedious derivations:

$$\frac{1}{k}\begin{bmatrix}\partial\mathbf{X}^{Y}/\partial z\\ \partial\mathbf{X}^{X}/\partial z\\ \partial\boldsymbol{\Gamma}^{Y}/\partial z\\ \partial\boldsymbol{\Gamma}^{X}/\partial z\end{bmatrix}=\begin{bmatrix}\mathbf{0} & \mathbf{0} & \mathbf{K}^{Y}\mathbf{E}^{-1}\mathbf{K}^{X} & \mathbf{I}-\mathbf{K}^{Y}\mathbf{E}^{-1}\mathbf{K}^{Y}\\ \mathbf{0} & \mathbf{0} & \mathbf{K}^{X}\mathbf{E}^{-1}\mathbf{K}^{X}-\mathbf{I} & -\mathbf{K}^{X}\mathbf{E}^{-1}\mathbf{K}^{Y}\\ \mathbf{K}^{X}\mathbf{K}^{Y} & \mathbf{M}^{-1}-\mathbf{K}^{Y}\mathbf{K}^{Y} & \mathbf{0} & \mathbf{0}\\ \mathbf{K}^{X}\mathbf{K}^{X}-\mathbf{E} & -\mathbf{K}^{X}\mathbf{K}^{Y} & \mathbf{0} & \mathbf{0}\end{bmatrix}\begin{bmatrix}\mathbf{X}^{Y}\\ \mathbf{X}^{X}\\ \boldsymbol{\Gamma}^{Y}\\ \boldsymbol{\Gamma}^{X}\end{bmatrix} \quad (2.48)$$

where $\mathbf{X}^{X}$ and $\mathbf{X}^{Y}$ are column vectors formed by χ_{xj} and χ_{yj}, respectively, $\boldsymbol{\Gamma}^{X}$ and $\boldsymbol{\Gamma}^{Y}$ are column vectors formed by γ_{xj} and γ_{yj}, and $\mathbf{I}$ is the unit matrix. Note that $\mathbf{K}^{X}$ and $\mathbf{K}^{Y}$ are diagonal matrices with the elements $K^{X}_{l,l}=k_{xj}/k$, where $j=l-q-1$ and $K^{Y}_{l,l}=k_{y}/k$. Again, $\mathbf{E}$ and $\mathbf{M}$ are the Toeplitz matrices (Li, 1996) generated by the Fourier coefficients of the dielectric function and its inverse, respectively, such that $E_{l,m}=\varepsilon_{p}^{ord}$ and $M_{l,m}=\varepsilon_{p}^{inv}$, where $p=l-m$. Equation (2.48) shows the modified matrix form for conical diffraction, which is different mathematically from previous work (Moharam *et al.*, 1995a) and (Peng and Morris, 1995), because the selection between matrices $\mathbf{E}$ and $\mathbf{M}$. In order to solve Eq. (2.48), $\mathbf{X}^{X}$ and $\mathbf{X}^{Y}$ can be decoupled from $\boldsymbol{\Gamma}^{X}$ and $\boldsymbol{\Gamma}^{Y}$ by

differentiating another time. In a similar way, $\mathbf{\Gamma}^X$ and $\mathbf{\Gamma}^Y$ can be decoupled from $\mathbf{X}^X$ and $\mathbf{X}^Y$. Note that matrix equation in another previous work (Lalanne and Morris, 1996) is consistent with Eq. (2.48); however, the authors did differently in the second derivations. The proper matrix equations for $\mathbf{X}$ and $\mathbf{\Gamma}$ are as follows:

$$\frac{1}{k^2}\begin{bmatrix}\dfrac{\partial^2 \mathbf{X}^Y}{\partial z^2}\\ \dfrac{\partial^2 \mathbf{X}^X}{\partial z^2}\end{bmatrix}=\begin{bmatrix}\mathbf{K}^X\mathbf{K}^X & \mathbf{K}^Y(\mathbf{E}^{-1}\mathbf{K}^X\mathbf{E}-\mathbf{K}^X)\\ \mathbf{0} & \mathbf{K}^Y\mathbf{K}^Y+(\mathbf{K}^X\mathbf{E}^{-1}\mathbf{K}^X-\mathbf{I})\mathbf{M}^{-1}\end{bmatrix}\begin{bmatrix}\mathbf{X}^Y\\ \mathbf{X}^X\end{bmatrix} \tag{2.49a}$$

$$\frac{1}{k^2}\begin{bmatrix}\dfrac{\partial^2 \mathbf{\Gamma}^Y}{\partial z^2}\\ \dfrac{\partial^2 \mathbf{\Gamma}^X}{\partial z^2}\end{bmatrix}=\begin{bmatrix}\mathbf{K}^Y\mathbf{K}^Y+\mathbf{M}^{-1}(\mathbf{K}^X\mathbf{E}^{-1}\mathbf{K}^X-\mathbf{I}) & (\mathbf{K}^X-\mathbf{M}^{-1}\mathbf{K}^X\mathbf{E}^{-1})\mathbf{K}^Y\\ \mathbf{0} & \mathbf{K}^X\mathbf{K}^X+\mathbf{E}(\mathbf{K}^Y\mathbf{E}^{-1}\mathbf{K}^Y-\mathbf{I})\end{bmatrix}\begin{bmatrix}\mathbf{\Gamma}^Y\\ \mathbf{\Gamma}^X\end{bmatrix} \tag{2.49b}$$

Accordingly, the solutions of χ_{xj}, χ_{yj}, γ_{xj}, and γ_{yj} can be expressed by the eigenvalue and eigenvectors of the matrices given by

$$\chi_{xj}(z)=\sum_{l=1}^{N}W_{j,l}^{A}\left[C_l^{A+}e^{k\xi_l(z-d)}+C_l^{A-}e^{-k\xi_l z}\right] \tag{2.50a}$$

$$\gamma_{xj}(z)=\sum_{l=1}^{N}W_{j,l}^{B}\left[C_l^{B+}e^{k\zeta_l(z-d)}+C_l^{B-}e^{-k\zeta_l z}\right] \tag{2.50b}$$

$$\chi_{yj}(z)=\sum_{l=1}^{N}V_{j,l}^{AA}\left[C_l^{A+}e^{k\xi_l(z-d)}+C_l^{A-}e^{-k\xi_l z}\right]+\sum_{l=1}^{N}V_{j,l}^{AB}\left[C_l^{B+}e^{k\zeta_l(z-d)}-C_l^{B-}e^{-k\zeta_l z}\right] \tag{2.50c}$$

$$\gamma_{yj}(z)=\sum_{l=1}^{N}V_{j,l}^{BA}\left[C_l^{A+}e^{k\xi_l(z-d)}-C_l^{A-}e^{-k\xi_l z}\right]+\sum_{l=1}^{N}V_{j,l}^{BB}\left[C_l^{B+}e^{k\zeta_l(z-d)}+C_l^{B-}e^{-k\zeta_l z}\right] \tag{2.50d}$$

where $W_{j,l}^{A}$ and $W_{j,l}^{B}$ are the elements of the matrices $\mathbf{W}^A$ and $\mathbf{W}^B$, and they are composed of the eigenvector corresponding to the eigenvalue of the matrices

$$\mathbf{A}=\mathbf{K}^Y\mathbf{K}^Y+\left(\mathbf{K}^X\mathbf{E}^{-1}\mathbf{K}^X-\mathbf{I}\right)\mathbf{M}^{-1} \tag{2.51a}$$

and

$$\mathbf{B}=\mathbf{K}^X\mathbf{K}^X+\mathbf{E}\left(\mathbf{K}^Y\mathbf{E}^{-1}\mathbf{K}^Y-\mathbf{I}\right) \tag{2.51b}$$

The exponential terms in Equation (2.50) originate from the forward and backward coupled diffracted waves in Region II. Here, C's are their unknown coefficients with superscripts + and – which signify forward and backward waves. Note that ξ_l and ζ_l are the elements of diagonal matrices $\mathbf{Q}^A$ and $\mathbf{Q}^B$, which are composed of the positive square root of the eigenvalue of **A** and **B**. In addition, $V_{j,l}^{AA}$, $V_{j,l}^{AB}$, $V_{j,l}^{BA}$, and $V_{j,l}^{BB}$ are the elements of matrices $\mathbf{V}^{AA}$, $\mathbf{V}^{AB}$, $\mathbf{V}^{BA}$, and $\mathbf{V}^{BB}$, respectively, given by

$$\mathbf{V}^{AA} = \mathbf{K}^Y \left(\mathbf{K}^X \mathbf{K}^X - \mathbf{E} \right)^{-1} \mathbf{K}^X \mathbf{W}^A \tag{2.52a}$$

$$\mathbf{V}^{AB} = \left(\mathbf{K}^X \mathbf{K}^X - \mathbf{E} \right)^{-1} \mathbf{W}^B \mathbf{Q}^B \tag{2.52b}$$

$$\mathbf{V}^{BA} = \left(\mathbf{K}^X \mathbf{E}^{-1} \mathbf{K}^X - \mathbf{I} \right)^{-1} \mathbf{W}^A \mathbf{Q}^A \tag{2.52c}$$

and

$$\mathbf{V}^{BB} = \mathbf{K}^Y \left(\mathbf{K}^X \mathbf{E}^{-1} \mathbf{K}^X - \mathbf{I} \right)^{-1} \mathbf{K}^X \mathbf{E}^{-1} \mathbf{W}^B \tag{2.52d}$$

In order to obtain complete field distributions in Regions I, II, and III, $10N$ unknown coefficients, i.e., $E_{xj}^r, E_{yj}^r, E_{zj}^r, E_{xj}^t, E_{yj}^t, E_{zj}^t, C_j^{A+}, C_j^{A-}, C_j^{B+}$, and C_j^{B-} $(j = 1, 2..., N)$ should be solved. Here, boundary conditions state that the tangential components of the electric and magnetic fields are continuous at region boundaries ($z = 0$ and $z = d$). Application of the boundary conditions yields $8N$ equations. Furthermore, since diffracted waves are assumed to be plane waves, they should be perpendicular to the corresponding wavevector; therefore,

$$\mathbf{k}_{rj} \cdot \mathbf{E}_{rj} = 0 \tag{2.53a}$$

and

$$\mathbf{k}_{tj} \cdot \mathbf{E}_{tj} = 0 \tag{2.53b}$$

which provide additional $2N$ equations. After solving the $10N$ coefficients, one can get the diffraction efficiencies by computing the time-averaged Poynting vector of each diffraction order along the z direction. Furthermore, the field distribution and Poynting vector distribution in the near field are completely obtained. Notice that RCWA can, in principle, achieve accuracy to an arbitrarily specified degree by the use of sufficient numbers of Fourier components to represent the dielectric function in the grating region. In the present study, a total of 81 Fourier terms (i.e., $N = 81$) are used and the results differ from those obtained with 201 terms by less than 0.3%. For a given wavelength and geometric parameters, the calculation of the transmittance using RCWA algorithm takes about 0.5 s of CPU time with a Pentium 4 processor (3.2 GHz speed).

CHAPTER 3

DIFFRACTION EFFICIENCY OF MICROSTRUCTURES

It has been shown that periodic structures have multiple order diffractions at well-defined directions when the incidence wavelength is comparable to the period. This chapter illustrates the diffraction efficiency measurement results from micromachined silicon wafers. Both one- and two-dimensional (1D and 2D) periodical microstructures are fabricated by plasma-assisted anisotropic etching. The method of rotating photomask is employed to produce 2.25×10^6 2D structures in a single sample ($7.5\times7.5\ \text{mm}^2$). Surface topography is characterized using a scanning electronic microscope (SEM) and an atomic force microscope (AFM). A laser scatterometer/diffractometer with high accuracy and angular resolution is used to measure the diffraction patterns at the wavelength of 635 nm. The effects of microstructure geometry and the plane of incidence (PoI) orientation on the diffraction efficiency are demonstrated. The experimental results are in excellent agreement with the predicted diffraction angles.

3.1. 1D and 2D Microstructure Design and Fabrication

The study employs chemical vapor deposition, plasma etching, and other microfabrication techniques to create 1D and 2D microstructures (Chen *et al.*, 2004). The actual may vary from the initial design and can be characterized by their period (Λ), groove width (w), and depth (d). One photomask is used to generate both 1D and 2D patterns. The photomask contains two types of periodic line structures (patterns), which have either 5 μm period and 1 μm line width (pattern A) or 5 μm period and 4 μm line

width (pattern B). Each type of lines is filled up with a 7.5×7.5 mm^2 square and the photomask contains 144 squares. By exposing the wafer once with this photomask, a 1D groove structures with $\Lambda = 5$ μm and $w = 1$ or 4 μm can be fabricated using the standard photolithographic steps. On the other hand, the 2D microstructure fabrication is performed with a unique "double exposure method," in which the wafer being patterned is exposed once with the photomask in place and another time after the mask is rotated by 90° (Heinzel *et al.*, 2000). Rotation of the mask allows for the fabrication of three 2D microstructures: type AA has $w_1 = w_2 = 4$ μm, type BB has $w_1 = w_2 = 1$ μm, and type AB has $w_1 = 1$ μm and $w_2 = 4$ μm. The periods are the same in both directions, i.e., $\Lambda_1 = \Lambda_2 = 5$ μm. As the result, the final microstructures contain 2.25×10^6 microstructures in a single square sample.

The steps used in the 1D and 2D microstructure fabrication process are described as follows. First, the single crystal silicon (100) wafer is cleaned with organic solutions, rinsed with de-ionized water, and then dried with nitrogen gas. A layer of SiO_2, which will eventually serve as an etching mask for silicon, is deposited with plasma-enhanced chemical vapor deposition (PECVD) to a thickness of approximately 0.7 μm. Secondly, a positive photoresist is spun on top of the SiO_2 layer. Ultraviolet (UV) light is then exposed through the photomask, once to make the 1D gratings and twice (by rotating the mask 90° between exposures) to create the 2D structures. The photoresist that was exposed to the UV light is then removed, leaving the desired patterns on top of the SiO_2 layer. The unmasked SiO_2 is anisotropically etched away by reactive iron etching (RIE). Afterwards, the remaining photoresist is removed by acetone. At this point, the desired

patterns are covered by the SiO_2 layer. Third, a Teflon layer is deposited and the plasma is used to anisotropically etch the silicon using a deep reactive ion etching (DRIE) technique, known as the Bosch process (Madou, 1997). Deep etching of the silicon can be achieved by repeating the etching process cycle. Finally, the remaining Teflon layer is burned away using oxygen plasma in the RIE, and the remaining SiO_2 is removed using buffered oxide etchant (BOE). The depth of the grooves depends on the number of Bosch process cycles completed and etching time used in each cycle.

A SEM and an AFM is used to study the morphology of the fabricated structures, as shown in Fig. 3.1. In Figs. 3.1a and 3.1b, typical 1D features (type A, $w = 4$ μm) and their cross-sectional view are shown. It can be seen that the shape and dimension of the structures are uniformly produced with $\Lambda = 5$ μm as expected. The shape is triangular because of the residual nonuniform and thin photoresist. This changes the pattern of the SiO_2 layer such that the thickness is the largest at the center and decreases towards the edge during the RIE process. This SiO_2 pattern results in the triangular shape feature on the Si surface. The width at the feature bottom is approximately 1.3 μm, slightly more than expected, and the height is approximately 0.9 μm. Figures 3.1c and 3.1d show the other type of 1D feature (type B, $w = 1$ μm) and its cross-sectional view. The sample contains valleys with alternatively different depth, which are 2.1 μm (deep) and 1.1 μm (shallow). These valleys are due to defects in the photomask and short exposure and development times. The period of all valleys is 5 μm, while the period of the valleys of the same depth is 10 μm. Furthermore, SEM image shows that the surface is not smooth but wavy, except for one groove shaped feature on the peak of each wave.

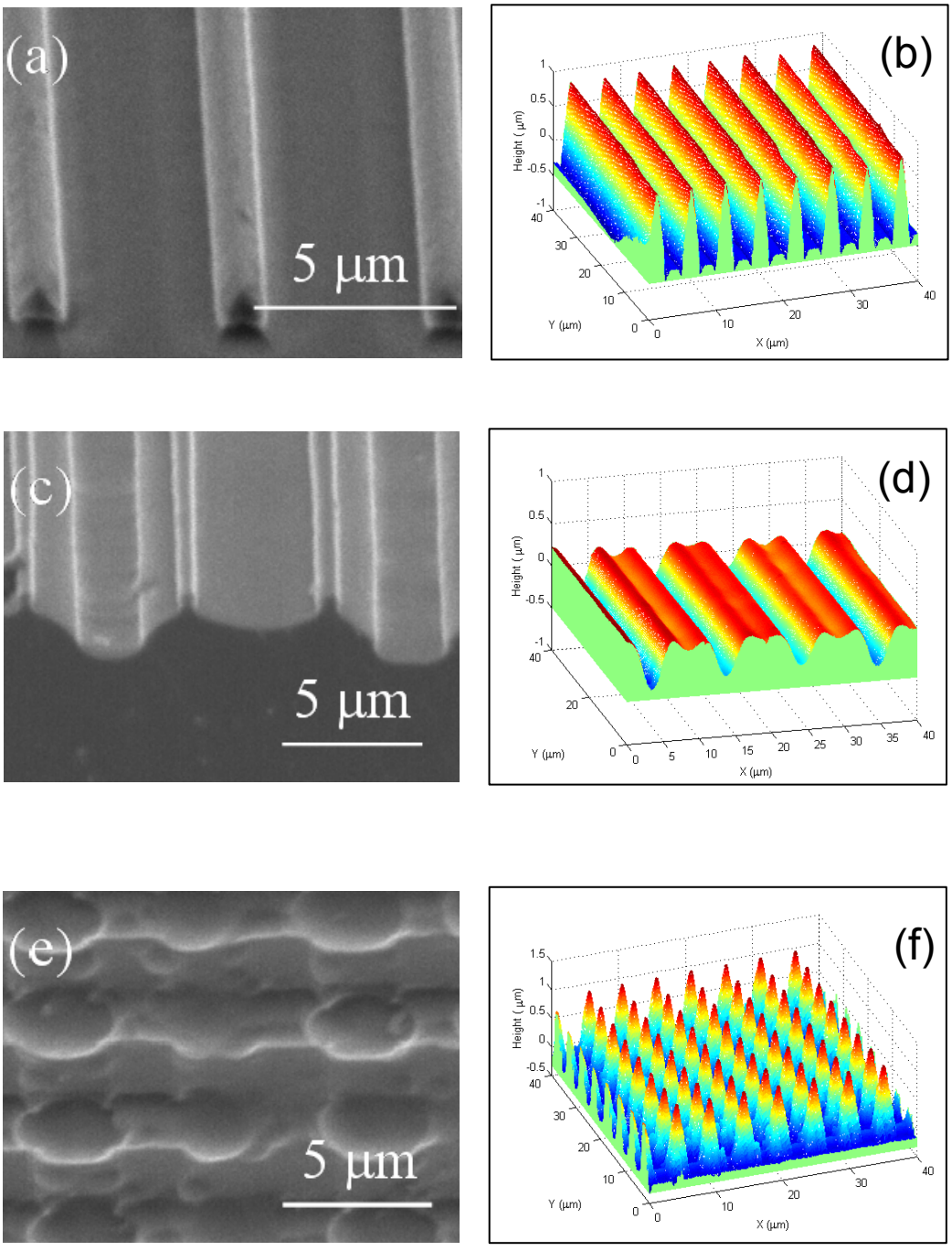

Figure 3.1 SEM and AFM images of three different samples: (a) and (b) are 1D features with $w = 4$ μm; (c) and (d) are 1D features with $w = 1$ μm; (e) and (f) are 2D features with $w_1 = w_2 = 1$ μm.

It can be seen from Figs. 3.1c and 3.1d that the fabricated structures are not the same as the initial design. These differences result from the balancing of the exposing and developing time for both patterns A and B. Features with a smaller linewidth (pattern A) need less exposure and development time than those with a larger linewidth (pattern B) to decrease the nonuniformity caused by the UV light diffraction and photoresist washing. Also, pattern B needs more time for the UV light and the developing chemicals to react with the bottom photoresist with the smaller opening (1 μm) on the photomask. Since the two patterns are on the same wafer for whole fabrication process, a balanced time is selected. As a result, the photoresist of pattern A is overexposed and overdeveloped such that uniform photoresist with smaller linewidth and height is remaining. On the contrary, the photoresist of pattern B is underexposed and underdeveloped so that thicker photoresist still remains some at the bottom. The photoresist has continuous connection resulting in the wave shape but not the groove shape after removing the exposed parts.

Figures 3.1e and 3.1f illustrate the 2D features and their magnification view. It is clearly shown that each feature has almost a square top surface ($2.5 \times 2.5\ \mu m^2$) and is uniformly fabricated. The reduced top surface size might be caused by the overexposure in the lithographic step. The connections among the neighboring squares are caused by the remaining photoresist in the plasma etching process. The silicon surface at the bottom of the structures is not flat because of ditching and trenching, which occur when the side walls of the SiO_2 are not perfectly vertical. During the RIE process, some etchant ions will collide at a glancing angle with the inclined side walls before arriving at the silicon surface (Madou, 1997). This gives a local increase in the etching rate, which leads to an unsmooth bottom surface.

3.2. Instrumentation

High-angular-resolution diffraction efficiency measurements of periodical structures rarely exist in the literature, especially for 2D gratings. In the present work, a newly developed three-axis automated scatterometer (TAAS) (Shen *et al.*, 2003) is employed for measurements of 1D and 2D periodic structures. The measured diffraction angles are compared with theoretical predictions. The TAAS includes a light source, a goniometric table, and a detection and data acquisition system. The light source is a fiber-coupled diode laser while light sources of different wavelengths are available. The laser diode is mounted on a thermoelectrically cooled platform, which is maintained at a constant temperature. A current driver controls the power of the diode laser. This laser system has shown excellent wavelength stability and power stability (0.2% over 24 hours). The fiber power output is 1 to 2 mW. The linear polarizer after the laser allows the selection of different polarizations. Since the sample is vertically mounted, the vertical polarization corresponds to the TE wave while the horizontal polarization corresponds to the TM wave. A beam splitter separates the light into two rays: one is incident on the sample being measured and the other is incident on a reference detector. The ratio of outputs from the two photodetectors is divided by the calibrated beam splitter ratio to obtain the diffraction efficiency η, which is the ratio of the reflected power to the incident power. The incident beam is collimated with a diameter of approximately 4 mm. The diameter of the precision aperture in front of the movable detector is 8 mm, large enough to collect the diffracted radiation at given diffraction order, except when $\theta_r > 60^\circ$. Furthermore, the small collecting solid angle (with a half-cone angle of 0.45°) yields a high angular resolution. The output of each photodiode is amplified by a trans-impedance

amplifier and fed into an input port of the lock-in amplifier. The lock-in amplifier sends an oscillating signal to the laser current controller, so that the output of the laser is modulated at the same frequency as that of the oscillating signal, resulting in a high signal-to-noise ratio. Since a number of samples are on the same wafer, an *x*-*y* translation stage is mounted on the sample holder to manually scan the wafer for measuring different samples.

A schematic drawing of three stages of TASS is shown in Fig. 3.2. Stages 1 to 3 are high-accuracy step-motor controlled rotary stages. Stages 1 and 3 are coaxial, but their rotations are independently controlled. The intersection (O) of the axis of stage 1 and stage 2 is the center point of the goniometric table. The light source is fixed and the incidence angle (θ) is varied by rotating stage 1. A dial rotator is mounted on the sample

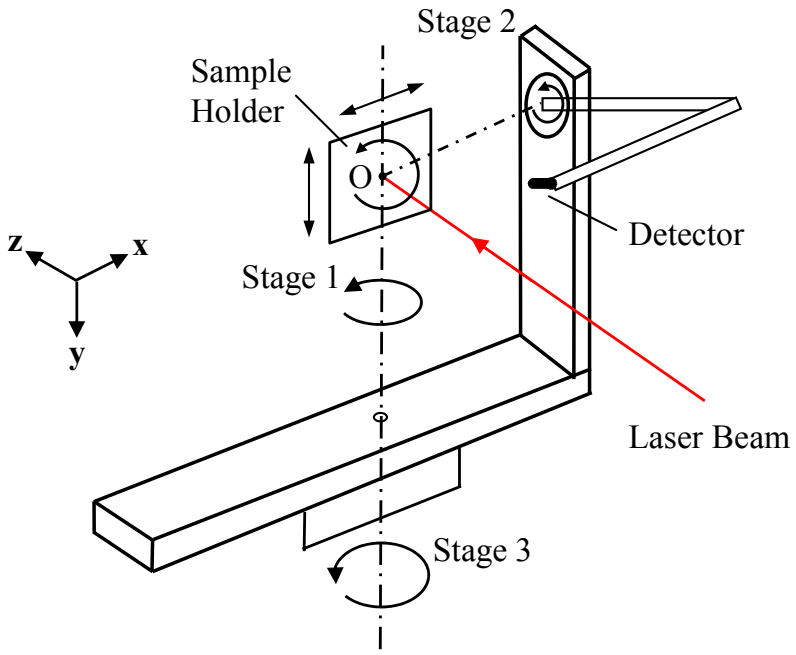

Figure 3.2 Schematic drawings of three automatically controlled stages for the TAAS.

holder for changing change the azimuthal angle (ϕ_i). Stages 2 and 3 are used to move the detector around point O. When stage 2 rotates, the detector arm moves vertically. Here, stage 3 can rotate 360°. Note that some orders of diffraction efficiency cannot be measured because the detector is between the laser and the sample and blocks the beam. For the 2D microstructured surfaces, the diffraction can be measured similarly by varying the azimuthal angle ϕ_i (i.e., rotating the sample holder). Only stages 1 and 3 need to be rotated to vary the angle of incidence and to locate the diffraction peaks along the direction determined by ϕ_i. To measure the hemispherical diffraction distribution, stage 2 needs to be rotated as well. In this case, the detector is manually positioned to each diffraction spot, which is found by observation. The detector tube is covered by a cap with a cross mark at its center. Stages 2 and 3 are changed by manually inputting their values to their controllers. When the reflected spot falls to the middle of the cross mark, the cap is removed and measurements are taken.

3.3. Diffraction Efficiency Measurements

Figure 3.3 shows the measurement results for a 1D microstructured sample, corresponding to Figs. 3.2a and 3.2b. The angles associated with the diffraction peaks are very close to the theoretical values calculated from well known grating equation, which has been mentioned before:

$$\sin\theta_j = \sin\theta + \frac{j\lambda}{\Lambda} \tag{3.1}$$

Within ±2° of the retroreflection angle, the detector blocks the incidence beam, and the reflected power cannot be measured. These angles are marked by an "×" sign in the figure. The diffraction patterns for normal incidence are almost symmetric with respect to

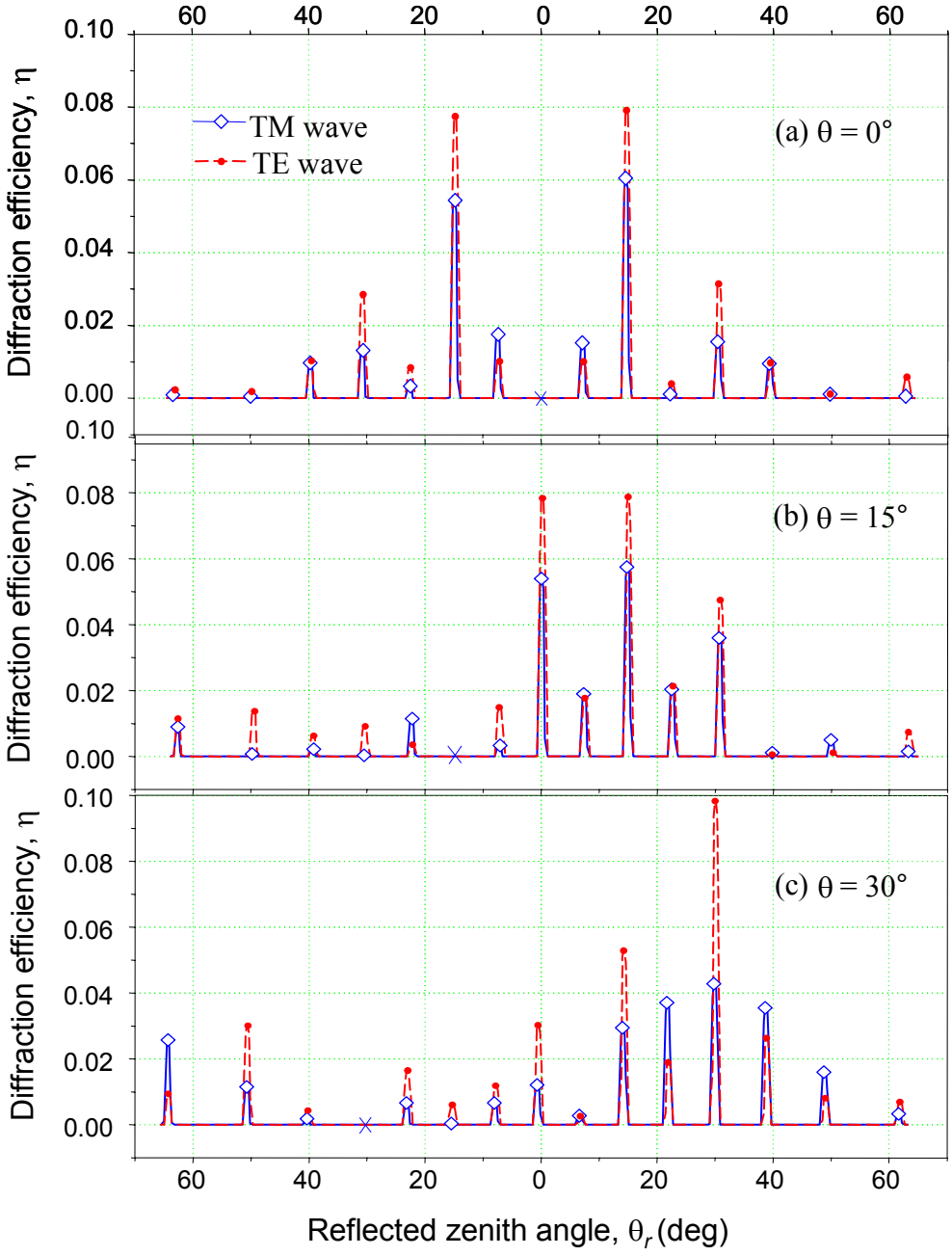

Figure 3.3 Diffraction efficiency of a 1D microstructure with $\Lambda = 5$ μm and $w = 4$ μm. The incidence zenith angles are: (a) $\theta = 0^{\circ}$; (b) $\theta = 15^{\circ}$; (c) $\theta = 30^{\circ}$.

the specular direction. The diffraction efficiency does not always decrease as the absolute value of diffraction order j increases. For example, the power ratios at $j = \pm 2$ are larger than those at $j = \pm 1$. The diffraction efficiency is generally larger for the TE wave than for the TM wave, except when $j = \pm 1$.

At $\theta = 15^\circ$ or 30°, the zeroth-order ($j = 0$) diffraction is in the specular direction, where diffraction efficiency η is the largest. When θ increases from 15° to 30°, the η at $j = 0$ increases for TE waves but decreases for TM waves. This trend is the same as the reflectance of a smooth dielectric surface, which can be predicted by the Fresnel equations. However, the diffraction efficiency is not symmetric with respect to the specular direction, which can not be explained by the grating equations. For example, the η for $j = -2$ is much larger than that for $j = 2$ in Figs. 3.3b and 3.3c. Furthermore, at $\theta = 30^\circ$, η is larger for the TE wave at $j = -2$ but smaller for the TM wave at $j = 2$. In addition, significant diffraction efficiency increment is observed for the highest orders ($j = -10$ and -11) at $\theta = 30^\circ$.

The measurement results for another 1D microstructured sample ($w = 1\ \mu\text{m}$, corresponding to Figs. 3.1c and 3.1d) are plotted in Fig. 3.4. While the angles of the diffraction peaks are very close to the theoretical values, the diffraction efficiency is not symmetric with respect to the specular direction at $\theta = 0^\circ$. For the TM wave, η is the largest at $j = -1$; however, for the TE wave, η is the largest at $j = -7$. This suggests that the structure on the sample is not symmetric. The diffraction efficiency is distributed more evenly for all orders of diffraction. Furthermore, some small peaks were observed between the peaks corresponding to a grating period of 5 μm. Their locations are

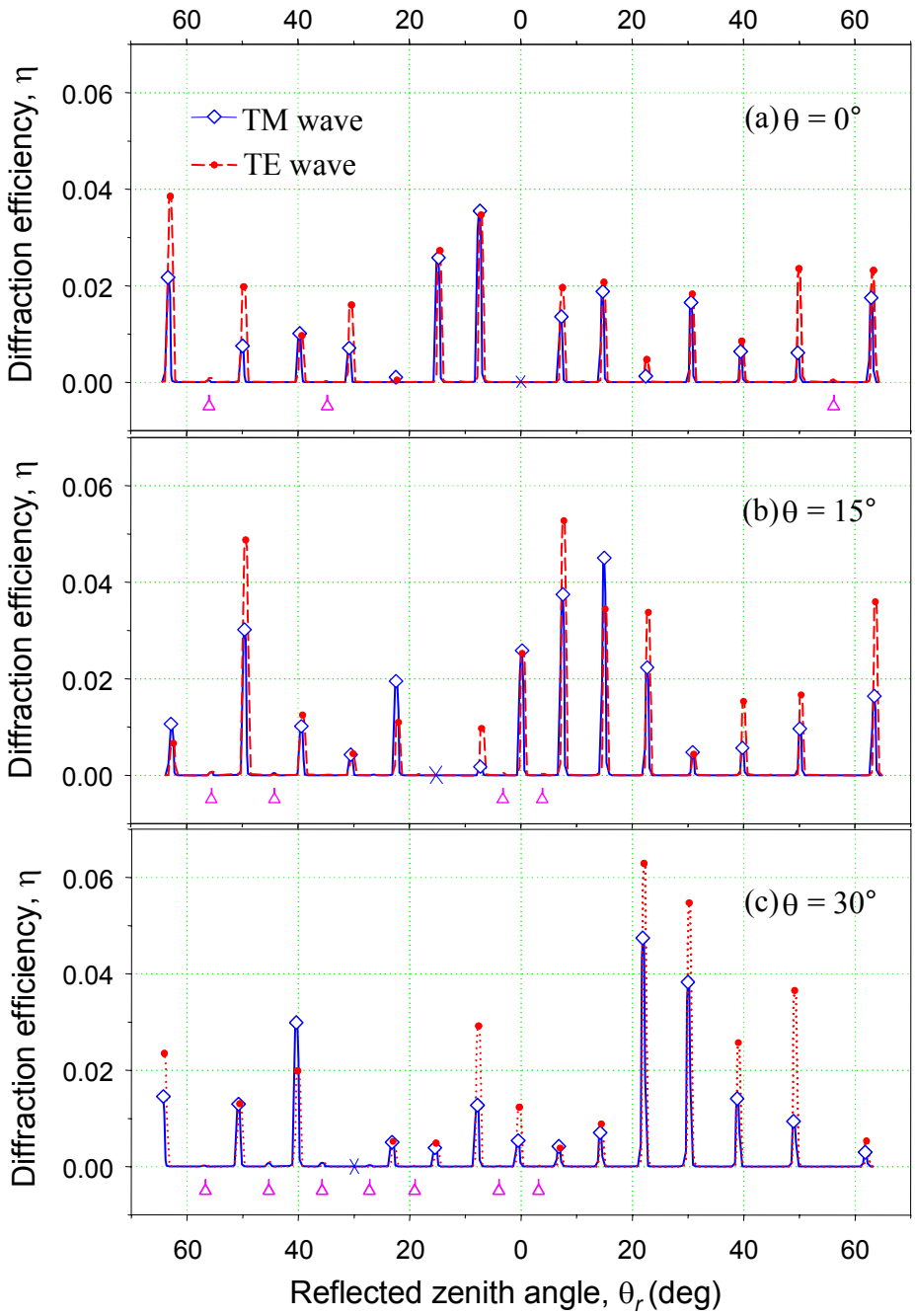

Figure 3.4 Diffraction efficiency of a 1D microstructure with $\Lambda = 5$ μm and $w = 1$ μm. The incidence zenith angles are: (a) $\theta = 0^{\circ}$; (b) $\theta = 15^{\circ}$; (c) $\theta = 30^{\circ}$.

identified by the triangular indicators underneath the curves in Fig. 3.4. These peaks correspond to the microstructures with the 10 μm period. It can be seen from the AFM measured profile in Fig. 3.1d that there exist deep and shallow groove pairs with 10 μm period. The photomask was inspected under an optical microscope, and some defects in the lines for this structure were found. These results suggest that diffraction efficiencies are sensitive to the micro-structural defects and could therefore be used as a non-contact diagnostic tool.

As shown in Figs. 3.4b and 3.4c, the diffraction efficiency for the zeroth-order diffraction is not the highest, except for the TM wave at $\theta = 15^{\circ}$. In fact, η for the TE wave at $\theta = 15^{\circ}$ is smaller at $j = 0$ and 1 than at $j = -8$, -1, and 5. At $\theta = 15^{\circ}$, η is smaller for the TE wave than for the TM wave in the specular direction. This result is the opposite of the reflection from a smooth surface, where the reflectance is slightly higher for the TE wave than for the TM wave. Half of the diffraction orders for the 10 μm period will overlap with those for the 5μm period. Therefore, the peaks may be contributions from the diffraction of both periods. As a result, structures on the surface strongly affect the radiative properties of a sample.

Using the simple 1D grating formula given in Eq. (3.1) can determine the direction of the diffraction. If the structures on the sample have a period along certain direction, there will be diffraction distributed along that direction. For example, if the 2D samples have a period along the $y = x$ direction, there is diffraction along $\phi_r = 45^{\circ}$. In the direction determined by *a* structures along the *x*-axis and *b* structures along the *y*-axis,

$\phi_r = \tan^{-1}(a/b)$. The polar angles of diffraction at normal incidence ($\theta = 0^\circ$) can be calculated by

$$\theta_j^{(a,b)} = \sin^{-1}\left(\frac{\lambda\sqrt{a^2+b^2}}{\Lambda}\right) \tag{3.2}$$

where the integer pair (a,b) may be considered as the 2D diffraction order. Figure 3.5 shows the observed diffraction pattern for a 2D microstructured sample which has features with at normal incidence. Here, φ_x is the angle between the reflection direction projected to the *x*-*z* plane and the *z*-axis, and φ_y is the angle between the reflection direction projected to the *y*-*z* plane and the *z*-axis. Hence,

$$\tan\varphi_x = \tan\theta_j \cos\phi_r \tag{3.3a}$$

$$\tan\varphi_y = \tan\theta_j \sin\phi_r \tag{3.3b}$$

It can be seen that the diffraction pattern is symmetric with respect to $\varphi_x = 0^\circ$ and nearly symmetric along the diagonal. Note that the power ratio is similar for both the TE and TM wave. As a result, the figure shows the average diffraction efficiency of both the TE and TM wave incidence. The diffraction efficiency value is classified into four levels and marked with circular spots. The radiuses of the spots correspond to the four levels and the centers locate the diffraction angular positions. The agreement between the predicted and most measured angular positions of the diffraction orders is within the uncertainty of the experiments ($\pm 0.2^\circ$), except for (*a*, *b*) = (4, 0), (2, 4), (3, 4) and (4, 4). When the diffraction spots on the surface of a unit sphere is projected to the vertical *x*-*y* plane, the distance between adjutant diffraction orders are exactly the same along either axis. This distance is given by λ/Λ.

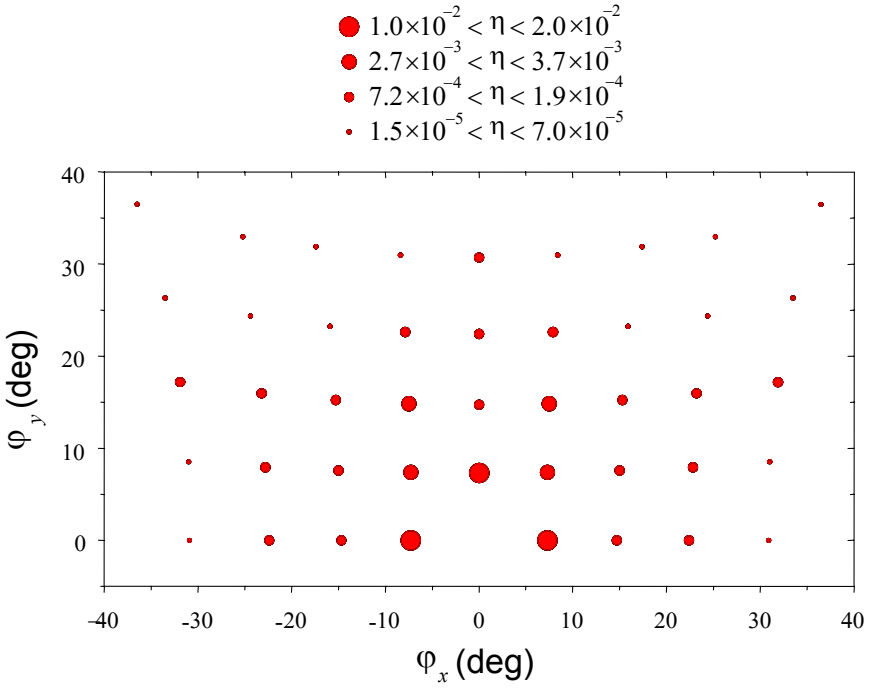

Figure 3.5 Diffraction efficiency of 2D microstructures.

CHAPTER 4

ABSORPTANCE OF NANOSCALE PATTERNED WAFER

Based on the understanding of radiative properties modified by periodic structures, the dissertation explores their application potentials in modern technologies. This chapter will study the first application by investigating absorptance of nanoscale patterned wafers, which are commonly seen in microelectronics. Temperature nonuniformity is a critical problem in rapid thermal processing (RTP) of wafers due to uneven diffusion of implanted dopants and introduces thermal stress. One cause of the problem is nonuniform absorption of thermal radiation, especially in patterned wafers, where the radiative properties vary across the wafer surface. Recent developments in RTP have led to the use of millisecond-duration heating cycle, which is too short for thermal diffusion to even out the temperature distribution. The feature size is already below 100 nm and smaller than the wavelength (200 – 1000 nm) of the flash-lamp radiation. Little is known to the spectral distribution of the absorbed energy for different patterning structures. This chapter will present a parametric study of the radiative properties of patterned wafers with the smallest feature dimension down to 30 nm, considering the effects of temperature, wavelength, polarization, and angle of incidence. The RCWA is employed to obtain numerical solutions of the Maxwell's equations and to assess the applicability of the method of homogenization based on effective medium formulations.

4.1. Model Development and Algorithm Validation

In order to understand the effect of nanostructure on the spectral absorptance, several patterned structures are considered, as illustrated in Fig. 4.1. Case A-1 is a bare Si

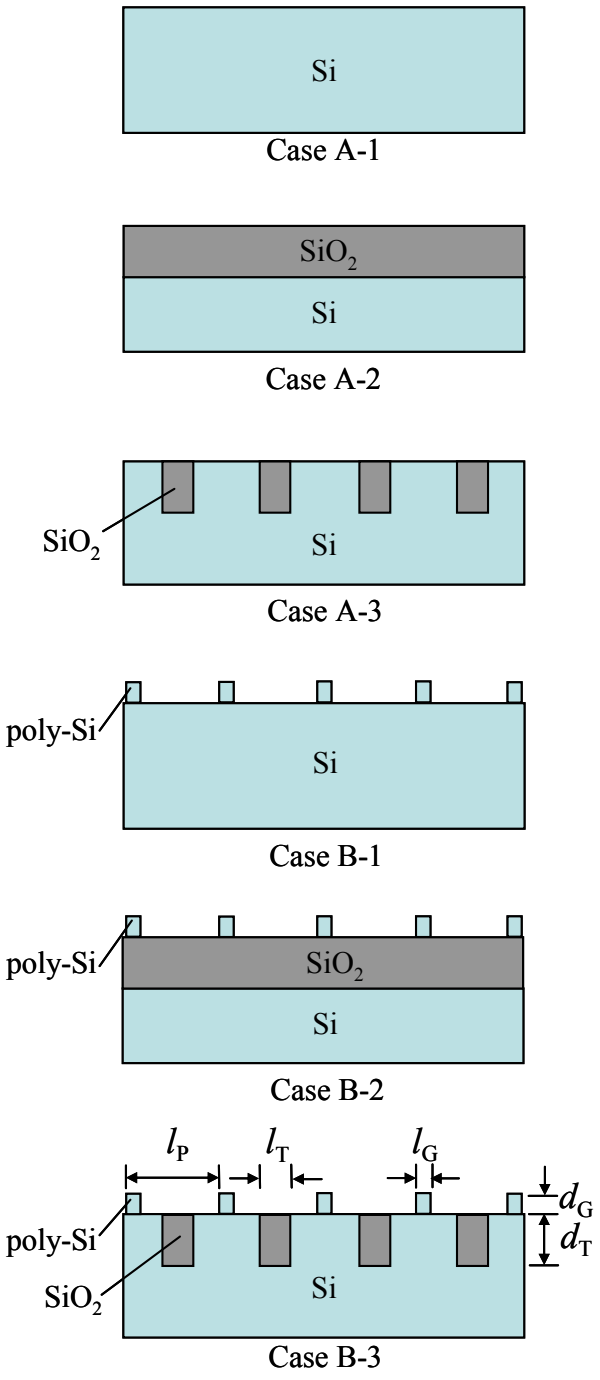

Figure 4.1 Structure sketches of selected cases, where d_G and d_T are the depths of gate and trench, respectively. l_G, l_P, and l_T are the lengths of gate, pitch, and trench, respectively.

wafer and Case A-2 is a SiO_2 thin-film on Si wafer. In Case A-3, an array of SiO_2-filled trenches (350 nm deep) is formed in the Si substrate. Cases B-1, B-2, and B-3 involve polycrystalline silicon (poly-Si) gates (30 nm wide and 50 nm high) on top of the structure that forms a thin grating layer. Case B-3 illustrates a generic pattern of interest for CMOS device technology, in which periodic patterns are formed on a Si wafer that includes trenches filled with SiO_2. These trenches provide electrical insulation between active areas of the device where transistors are formed. In the middle of each active area, there is a strip of poly-Si, representing the gate electrode. In reality, this gate is isolated from the Si substrate by a very thin dielectric film. However, this film is only about 1-nm thick for the 65-nm-node devices, and hence, it can be neglected in the optical models. The features are symmetrically located in a lateral period of l_P = 240 nm. Table 4.1 lists the dimensions of the trench and gate for structures of all cases. Various combinations of these structures can be expected in different parts of the wafer. It is hoped that the simplified structures will also reveal how individual periodic patterning of the isolation oxide and the poly-Si gate film influence the optical properties. While only 1D and 2D structures are studied, the results should be instructive to the more general 3D patterned structures. Similar approximations were also used in previous numerical simulations (Erofeev *et al.*, 1995; Liu *et al.*, 2004). In the remaining of this section, the spectral distribution of the lamp and optical properties of materials are discussed in the following.

Arc lamps filled with Xe or Ar gases emit light by generating an electric arc across a gap between two electrodes. The peak wavelength corresponds to a blackbody temperature around 6000 K. However, the emission is confined to the spectral region for 200 nm $\leq \lambda \leq$ 1000 nm, where λ is the wavelength in vacuum. The actual emission

spectrum is not a smooth curve due to the discrete plasma emission lines. The emission spectrum also varies with the discharge voltage, duration of the pulse, and the optical materials. Therefore, the reported spectral distributions by different manufacturers and researchers have a large variation. To study the total absorptance, the present work assumes a simple trapezoid spectral distribution of the lamp emission. The normalized spectrum distribution $G(\lambda)$ is 1 for $400\ \text{nm} \le \lambda \le 600\ \text{nm}$ and linearly reduces to 0 towards $\lambda = 200$ nm and 1000 nm.

Table 4.1 Feature dimensions of selected cases (Unit: nm)

	A-1	A-2	A-3	B-1	B-2	B-3
d_G	—	—	—	50	50	50
d_T	—	350	350	—	350	350
l_P	240	240	240	240	240	240
l_G	0	0	0	30	30	30
l_T	0	240	60	0	240	60

The input material properties are the optical constants (i.e., refractive index n and extinction coefficient κ) of Si, SiO_2, and poly-Si in the wavelength range of the flash-lamp spectrum. The optical constants are related to the dielectric function $\varepsilon = (n + i\kappa)^2$. In the present study, the optical constants of Si at room temperature are taken from the tabulated values in Ref. (Palik, 1998). Jellison and Modine (1983) measured the dielectric function of silicon from 260 to 840 nm from room temperature to 700°C. In another paper (Jellison and Modine, 1994), these authors developed expressions of n and κ in terms of temperature and wavelength, applicable to the visible and near-infrared region. Optical constants at higher temperatures were measured by Sun et al. (1997). In the

present work, the optical constants from 280 nm to 500 nm at 700°C and 910°C are taken from Ref. (Jellison and Modine, 1983) and Ref. (Sun *et al.*, 1997), respectively. Because the expressions in Ref. (Jellison and Modine, 1994) give good agreement with the measured data in Refs. (Jellison and Modine, 1983; Sun *et al.*, 1997) at wavelengths from 500 to 1000 nm, the optical constants are calculated from the expressions in this spectral range. In the spectral region from 200 nm to about 280 nm, room temperature data are substituted. While the optical constants may be very different at high temperatures, the effect on the total absorbed energy should not be significant because it is near the source cutoff wavelength. The selected dielectric functions of Si at 25°C, 700ºC, and 910ºC are plotted in Fig. 4.2 for comparison. Some interpolations between the data are made to produce smooth curves in the calculation.

For SiO_2, the imaginary part of the dielectric function is negligibly small in the spectral range of interest and absorption can be neglected. Malitson (1965) provided an equation as a fit for n of SiO_2 at 25ºC. Because the relative error of four to seven significant digits in the equation is less than 0.01%, only four significant digits are selected as expressed in the following.

$$n_{SiO_2} = \left(1 + \frac{0.6962\lambda^2}{\lambda^2 - 0.06840^2} + \frac{0.4079\lambda^2}{\lambda^2 - 0.1162^2} + \frac{0.8975\lambda^2}{\lambda^2 - 9.896^2} \right)^{1/2} \tag{4.1}$$

This equation is also believed to represent the values at higher temperatures due to the small temperature coefficient ($1.2\times10^{-5}\,\mathrm{K}^{-1}$) of the refractive index of SiO_2 (Timans, 1996).

The dielectric function of poly-Si is assumed to be the same as that for single-crystal silicon, although in reality differences are expected to arise from the presence of

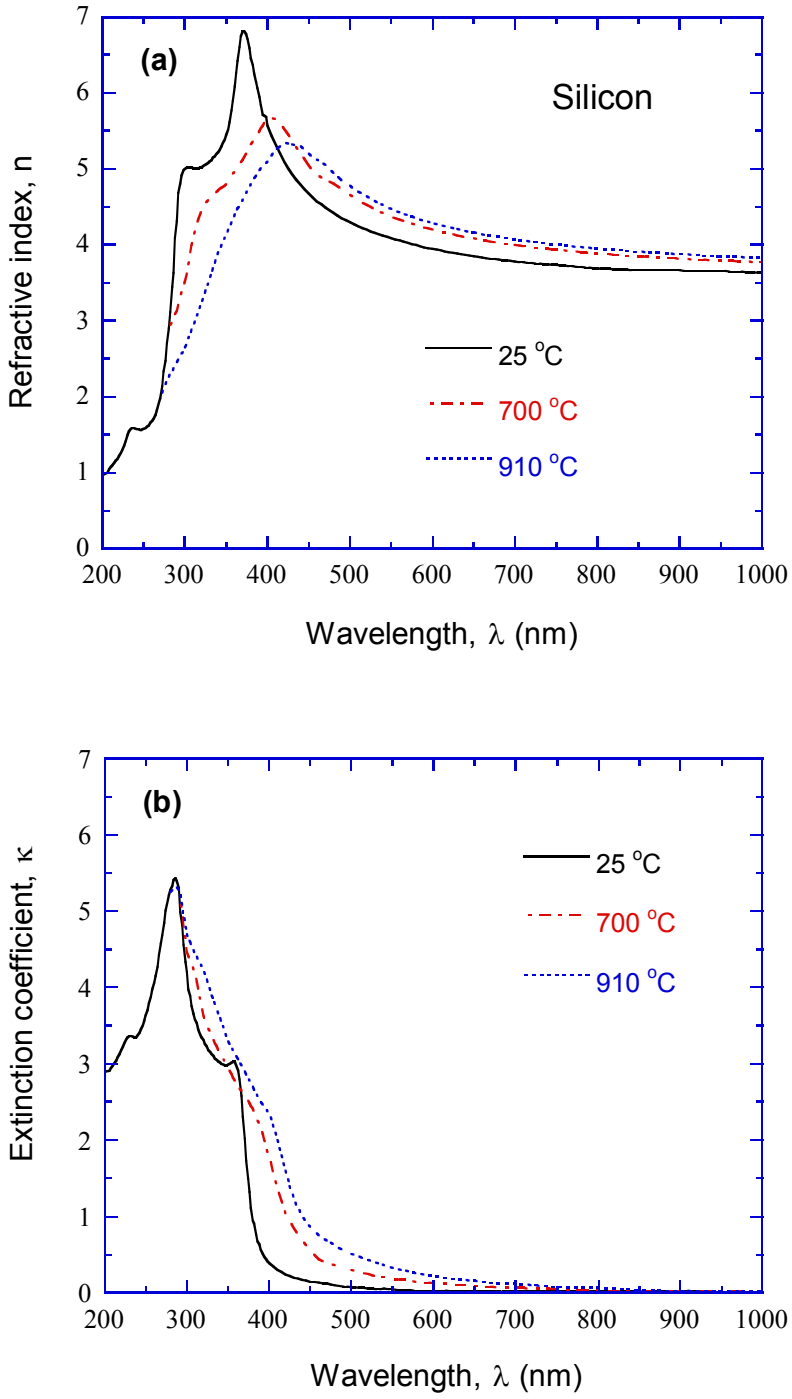

Figure 4.2 Optical constants of silicon at 25°C, 700°C, and 910°C: (a) refractive index; (b) extinction coefficient.

grain boundaries in the material and from variations in grain structure (Lindsay *et al.*, 2004). According to the previous study (Timans, 1996), the difference between the optical constants of poly-Si and Si is not so large in the red to infrared region. Note that doping effects of poly-Si is not taken into consideration here, and electrically active doping may strongly vary the optical properties in the infrared region. On the other hand, in the ultraviolet to visible wavelength region, the structural disorder in the poly-Si could change optical properties somewhat regardless of doping. Since poly-Si occupies a small volume fraction only, the use of the optical constants of silicon should not cause significant errors.

The RCWA algorithm is valid here because the solution converges without inherent numerical instabilities and it always satisfies the energy conservation. The solution is accurate to an arbitrary level of accuracy and depends only on the number of spatial-harmonic terms. The numerical code developed in this work is verified by comparison with the published results (Auslender and Hava, 1995; Moharam *et al.*, 1995a). Some validations are also made by comparison with multilayer grating structures (Moharam *et al.*, 1995b). The convergence is checked by increasing the number of terms $N = 2q + 1$ from 41, 81, 121, to 201. Notice that while most of the orders are evanescent waves that do not contribute to the reflected energy, it is necessary to include them in the RCWA to represent the Fourier expansion of dielectric function in the grating region and to accurately describe the electromagnetic fields around the grating region. The convergence is the slowest for the TM wave at 200 nm wavelength. The reflectance variation is less than 0.001 between $N = 81$ and 121. Therefore, 81 orders of diffraction ($j = 0, \pm1, \pm2, \ldots, \pm40$) are retained in all calculations.

The radiative properties calculated from RCWA are successfully compared with the simulation results of patterned wafers from other numerical methods (Liu *et al.*, 2004). The pattern is a 50-nm-thick Si_3N_4 grating on a Si substrate with a period of $\Lambda = 2$ μm and a filling ratio $\phi = 0.5$. In addition, when the filling ratio is 0 or 1, the grating becomes a homogeneous medium. The RCWA simulation gives the same results as these obtained from thin-film multilayer algorithm (Lee *et al.*, 2005). Recently, another supportive evidence for the numerical algorithm validity is the agreement of absorptance spectrum for Cases A-3 and B-1 by RCWA and finite difference time-domain (Fu *et al.*, 2006).

A Pentium 4 computer with a 3.2 GHz processor and 2 GB memory is used for computation. In order to compare the calculation efficiency of RCWA and EMT programs, Case B-3 is selected due to its complexity. RCWA divides the structure into four regions with two grating layers. On the other hand, EMT approximates the case as two thin films on the Si substrate. The computation speed is 2000 data points per second for EMT and 2-3 data points per second for RCWA. That is to say that EMT algorithm is about 1000 faster than RCWA because of its large number of matrix elements. Additional complexity will arise in RCWA when the wavevector of the incident radiation and the grating vector are not perpendicular to each other. On the other hand, the effective medium formulation can easily be applied to compute the hemispherical properties when the grating region can be approximately isotropic and homogeneous. The validation of the EMT is therefore very important for practical applications.

4.2. Spectral Absorptance

Figure 4.3 shows the spectral absorptance for Cases A-1 (plain Si) and A-2 (350-nm-thick SiO_2 on Si) at normal incidence. Thin-film optics formulation is sufficient for

these calculations without using the RCWA or EMT algorithms. The results are shown in order to see the effect of temperature on the absorptance and to serve as benchmark results for comparison with grating structures later. For plain silicon, it can be seen that the absorptance increases towards longer wavelengths. A common misperception is that a large κ value will give a large absorptance and silicon will have a large absorptance in the ultraviolet region. On the contrary, the absorptance is the smallest when κ is the greatest at around λ = 280 nm. This is because of the high reflectivity of Si in this region, similar to metals in the visible region. For normal incidence, the absorptance of plain Si can be calculated from

$$\alpha_\lambda = \frac{4n_{\mathrm{Si}}}{(n_{\mathrm{Si}}+1)^2 + \kappa_{\mathrm{Si}}^2} \tag{4.2}$$

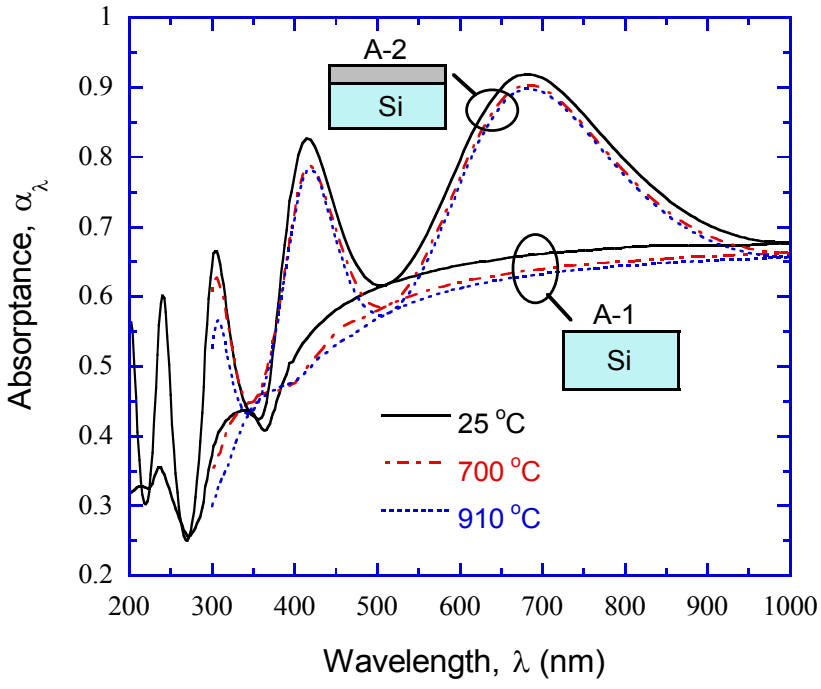

Figure 4.3 Calculated normal, spectral absorptance for plain Si (Case A-1) and SiO_2-coated Si (Case A-2) at 25°C, 700°C, and 910°C.

When the extinction coefficient is small, the absorptance decreases as the refractive index increases. Increasing the extinction coefficient will significantly reduce the absorptance as it becomes large. On the other hand, the extinction coefficient is directly related to the radiation penetration depth, $\delta_\lambda = \lambda/(4\pi\kappa)$. The calculated δ_λ increases from 4 nm for $\lambda = 200$ nm to ≈ 1 μm for λ = 800 nm at 910°C. The absorptance with SiO_2 film oscillates due to interference effects. The phase shift in the SiO_2 film is determined by $\beta = 2\pi d_{SiO_2} n_{SiO_2} / \lambda$ at normal incidence. The absorptance reaches a minimum close to that of plain Si when β/π is a positive integer. The corresponding wavelengths are $\lambda \approx$ 1000, 500, 345, 262, and 214 nm. On the other hand, the absorptance is maximized when $\beta = \pi/2, 3\pi/2, 5\pi/2 \ldots$, corresponding to $\lambda \approx$ 680, 420, 298, 236, and 200 nm. In general, SiO_2 film behaves as an antireflection coating that enhances the absorptance (Born and Wolf, 1999), except near $\lambda \approx$ 214 and 262 nm due to the lower refractive index of silicon at very short wavelengths.

The difference in absorptance at temperatures from 25°C to 910°C is less than 0.05 except near λ = 300 nm, where the maximum difference is 0.08 for a plain Si and 0.12 for a SiO_2 film on a Si substrate. The total absorptance for Case A-1 is 0.59, 0.57, and 0.56 and for Case A-2 is 0.72, 0.70, and 0.69 at 25°C, 700°C, and 910°C, respectively. This suggests that the temperature dependence of the optical constants may not affect the absorption significantly. One should be cautious about a generalization that the temperature dependence is weak to wavelengths longer than 1 μm, where the silicon wafer is semitransparent below 700°C, and consequently, the absorption depends strongly on temperature (Timans, 1996; Zhang *et al.*, 2003). Because of the importance to

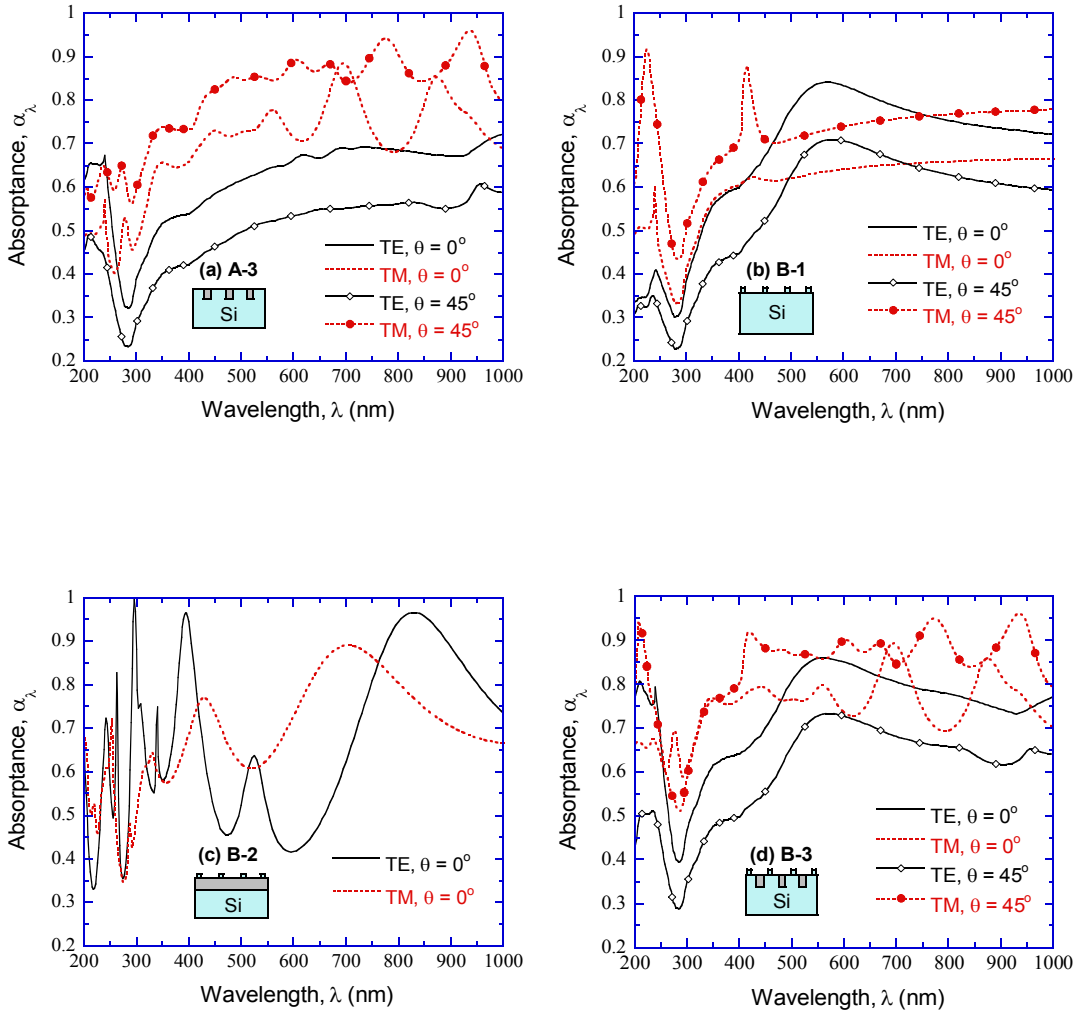

Figure 4.4 Spectral absorptance predicted using RCWA for cases with gratings at 910°C at $\theta = 0^\circ$ and 45°: (a) Case A-3; (b) Case B-1; (c) Case B-2; (d) Case B-3.

high-temperature annealing, all calculations in the following are based on optical constants of Si at 910°C (except in the wavelength region from 200 to 300 nm where room temperature data are substituted).

Figure 4.4 shows the directional, spectral absorptance of Cases A-3, B-1, B-2, and B-3 predicted by RCWA, with different polarizations at incidence angels of 0° and 45°. The absorptance for Case B-2 at $\theta = 45^\circ$ is not presented for the sake of clarity. Because of the gratings, the absorptance depends on the polarization even at normal incidence. When the normal absorptance for Case A-3 shown in Fig. 4.4a is compared to that of plain silicon shown in Fig. 4.3, the absorptance for TE waves increases significantly at short wavelengths, by more than 0.3 from 200 nm to 240 nm, and the enhancement is less than 0.1 at $\lambda > 300$ nm. At wavelengths longer than 280 nm, the absorptance is in general greater for TM waves than for TE waves. Furthermore, the absorption spectrum for TM waves oscillates, but not so much for TE waves. On the contrary, for Case B-1 as shown in Fig. 4.4b, the normal absorptance is greater for TE waves than for TM waves at wavelengths longer than 450 nm, whereas the absorptance for TM waves is enhanced at short wavelengths with a peak at $\lambda = 240$ nm. The effect of gates on the TE wave absorptance is rather surprising because the gates are only 50 nm high with a poly-Si filling ratio of 0.125. It is also interesting to notice different effects on polarized absorptance between the gates and trenches.

The absorptance spectra for Case B-2 are more complicated due to the coupling between the interference effect of the SiO_2 layer and the grating effect of the gates. Nevertheless, the gates have little effect on the absorptance for TM waves in the long wavelength region, as can be seen by comparison of Fig. 4.4c with the absorptance for

Case A-2 shown in Fig. 4.3. However, the absorptance for TE waves is dramatically different with and without poly-Si gates. Here again, the gates affect the TE wave absorptance spectra significantly. Interesting enough, the absorptance spectra for Case B-3 exhibit the combined effects of gates and trenches, as can be clearly seen from Fig. 4.4d. For TE waves, the absorptance spectra are similar to those for Case A-3 at shorter wavelengths and largely modified by features in Case B-1 at longer wavelengths. For TM waves, the absorptance spectra retain features for Case B-1 at shorter wavelengths and resemble features shown for Case A-3 at longer wavelengths.

The total absorptance calculated with different methods at 910°C for all six cases are listed in Table 4.2. The total absorptance of Cases A-1 and A-2 calculated from thin-film optics is also presented for comparison. The total normal absorptance for plain Si is 0.56, and it increases to 0.61 for TE waves and 0.72 for TM waves in Case A-3. On the other hand, the total normal absorptance is 0.71 for TE waves and 0.62 for TM waves in Case B-1. Due to the combined effects of gates and trenches, the total normal absorptance of Case B-3 is increased to 0.75 for TE waves and 0.77 for TM waves. At normal incidence, the total absorptance averaged over the two polarizations for Case B-3 is 0.76, which is 0.20 higher than that of plain Si. The nanoscale gates give rise to the averaged total absorptance by about 0.1 from Case A-1 to Case B-1 and from Case A-3 to Case B-3. Similarly, the trench layer increases nearly 0.1 in the averaged total absorptance from Case A-1 to Case A-3 and from Case B-1 to Case B-3. On the other hand, the total normal absorptance of Case B-2 for the TM wave is only 0.02 higher and that for the TE wave is 0.06 lower than that of Case A-2. Therefore, the effect of gates on the total

absorptance with SiO_2 film is very small. Note that the total absorptance is also a function of the source spectra.

Table 4.2 Total absorptance for different cases at 910°C.

Case No.	A-1	A-2	A-3	B-1	B-2	B-3
Angle of incidence $\theta = 0^\circ$						
TE-rigorous	0.557	0.688	0.614	0.711	0.634	0.747
TM-rigorous	0.557	0.688	0.715	0.615	0.712	0.765
Average	0.557	0.688	0.665	0.663	0.673	0.756
EMA Difference	—	—	0.631 -0.034	0.647 -0.016	0.716 0.043	0.719 -0.037
TE-0 Difference	—	—	0.604 -0.010	0.823 0.112	0.727 0.093	0.842 0.095
TM-0 Difference	—	—	0.774 0.059	0.576 -0.039	0.692 -0.020	0.791 0.026
Average Difference	—	—	0.689 0.024	0.700 0.037	0.710 0.037	0.817 0.061
Angle of incidence $\theta = 45^\circ$						
TE-rigorous	0.441	0.617	0.491	0.580	0.573	0.614
TM-rigorous	0.680	0.737	0.824	0.722	0.757	0.848
Average	0.561	0.677	0.658	0.651	0.665	0.731
EMA-TE Difference	—	—	0.510 0.019	0.539 -0.041	0.659 0.086	0.611 -0.003
EMA-TM Difference	—	—	0.753 -0.071	0.723 0.001	0.764 0.007	0.790 -0.058
Average Difference	—	—	0.632 -0.026	0.631 -0.020	0.712 0.047	0.701 -0.030
TE-0 Difference	—	—	0.485 -0.006	0.710 0.130	0.650 0.077	0.731 0.117
TM-0 Difference	—	—	0.872 0.048	0.683 -0.039	0.739 -0.018	0.873 0.025
Average Difference	—	—	0.679 0.021	0.697 0.046	0.695 0.030	0.802 0.071

Generally speaking, when the incidence angle increases from 0° and 45°, the absorptance for TM waves increases and that for TE waves decreases, as evidenced from Fig. 4.4 and Table 4.2. This is consistent with the Fresnel equation, which predicts that the reflectance of a plain Si for TM waves decreases, until the Brewster angle, and that for TE waves increases when the angle of incidence increases. It should be noticed that the oscillation for TM waves in Cases A-3 and B-3 shifts phase when the angle of incidence is changed. While most of the absorptance spectra have a valley at 280 nm, the absorptance of Case A-3 reaches a peak at $\theta = 0^{\circ}$ and 45° and that of Case B-3 reaches a peak only at $\theta = 0^{\circ}$ for TM wave, see Figs. 4.4a and 4.4c. The above discussions clearly demonstrate the complexity of wave interactions inside the grating regions. Nevertheless, some unique features associated with the grating structures can be identified and are elaborated in the next paragraph.

Absorptance peaks exist in the absorptance spectra at λ = 240 nm for normal incidence, as can be seen from Fig. 4.4 for both polarization. The features in Fig. 4.4c are too complicated to distinguish this peak. While there are shoulders in the optical constants of Si near λ = 240 nm and a peak in the absorptance of plain silicon, the peaks are much sharper and more prominent with gratings, especially for TM waves in Cases A-3 and B-1. The very sharp peaks are caused by the well-known Wood's anomaly in the diffraction grating theory (Hessel and Oliner, 1965). Wood's anomaly can cause an abrupt, asymmetric change in the absorptance spectrum when a diffraction order just appears at the grazing angle. Since the grating period Λ = 240 nm, for normal incidence at λ = 240 nm, the +1 and −1 diffraction order will be at a diffraction angle $\theta_{\pm 1} = \pm 90^{\circ}$. Again, the grating equation as below is used for predicting Wood's anomaly.

$$\sin\theta_j = \sin\theta + \frac{j\lambda}{\Lambda} \tag{4.3}$$

According to the grating equation Eq. (4.3), at 45° incidence, $\theta_{-1} = -90°$ when λ = 410 nm. Wood's anomaly can be clearly seen for the TM wave at $\theta = 45°$ in Fig. 4.4b and in Fig. 4.4d with a little reduced and shifted peak due to the influence of the trench layer.

4.3. Validity Assessment for Effective Medium Formulations

Figure 4.5 compares the normal absorptance spectra for Cases A-3, B-1, and B-3 predicted by RCWA with different formulations of effective medium approaches. In the graphs, 0 and 2 refer to predictions based on EMT-0 and EMT-2, respectively. Note that for normal incidence, the predicted absorptance by EMA is the same for both polarizations. In Fig. 4.5a, the results of both EMA and TE-0 agree well with those of RCWA at $\lambda \geq 250$ nm. While TE-2 follows the RCWA result closer near λ = 1000 nm, it underpredicts the absorptance at shorter wavelengths. The reason of disagreement is due to the second-order correction term of the dielectric function. Because the condition that $\lambda >> \Lambda$ is not satisfied for the present study, the second-order term can be so large to produce a nonphysical dielectric function whose imaginary part is negative at $\lambda \leq 300$ nm for the trench region. In Fig. 4.5b, the absorption spectra calculated from the effective medium formulations are not in phase with that from RCWA and none of them can predict the spectral absorptance well. On the other hand, if the absorptance is averaged over the spectral region or uses the source spectrum to obtain the total absorptance, one should not expect significant deviations from the RCWA if EMA and EMT-0 are used. The insignificant deviation comes from the spectrally periodic behavior though errors are not necessarily averaged out. This is indeed the case as can be seen from Table 4.2,

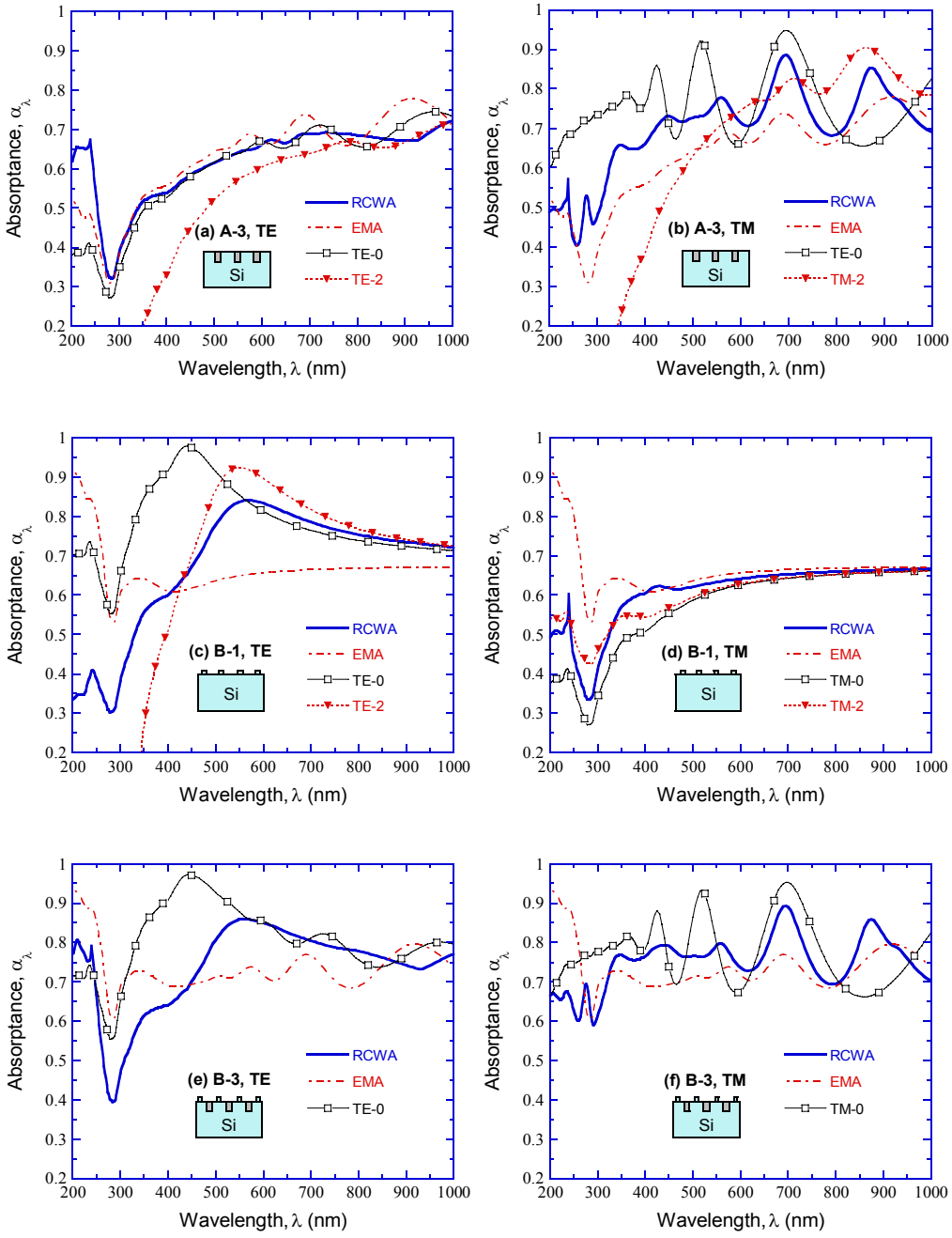

Figure 4.5 Comparison of the absorptance predicted by different methods at 910°C: (a) TE wave for Case A-3; (b) TM wave for Case A-3; (c) TE wave for Case B-1; (d) TM wave for Case B-1; (e) TE wave for Case B-3; (f) TM wave for Case B-3.

where the total absorptance obtained from EMA and EMT-0 is compared with that from the rigorous solutions and the differences are also shown.

Figures 4.5c and 4.5d show absorptance of Case B-1 for both TE and TM waves, respectively. The absorptance predicted by TE-0 and TE-2 are in good agreement with that using RCWA at $\lambda \geq 600$ nm. In addition, TE-0 can capture some of the features in RCWA results at short wavelengths, except that it largely overpredicts the absorptance. TE-2 again failed at shorter wavelengths completely. Compared with the RCWA prediction, EMA significantly overpredicts the absorptance at $\lambda \leq 400$ nm and underpredicts the absorptance at $\lambda \geq 400$ nm than that of RCWA. Figure 4.5d shows that all the effective medium formulations give good agreement with results from RCWA, except EMA overestimates the absorptance at $\lambda \leq 300$ nm. This behavior may arise because the absorptance at longer wavelengths changes a lot for the TE wave but very little for the TM wave when the gates are present. Similar observations can be made based on the absorptance spectra for Case B-2, which is not shown. When comparing different models for Case B-3, the spectra using TE-2 and TM-2 are not shown in Figs. 4.5e and 4.5f, because the results are not as good as those of TE-0 and TM-0. The spectra from RCWA clearly show features that arise from the behavior seen in the absorptance for Cases A-3 and B-1. Because the pattern of Case B-3 includes two layers of periodic structure, none of the effective medium formulations can predict the complex absorptance spectra of the two-layer grating structures.

Although the effective medium formulations failed to describe the spectral behavior of the gratings studied here over the whole wavelength range, they may provide reasonable values for the total absorptance because the spectral absorptance oscillates and

crosses one another in some regions. The absorptance from EMT-2 is not shown in Table 4.2 because adding the second-order term can only cause EMT to fail at short wavelengths. EMA gives good agreements with the total absorptance for most cases at both normal and oblique incidence. The average difference between two polarizations is less than 0.05. On the other hand, EMA predictions often have a larger disagreement for one polarization. For EMT-0, the averaged total absorptance has a slightly larger difference for Cases B-1 and B-3 compared with EMA. Though EMT-0 deals different polarized wave separately, the average difference for Case B-3 is 0.06 and 0.07 at $\theta = 0^\circ$ and 45°, respectively. In addition, the difference for the TE wave is greater than 0.1 for Case B-1. It is interesting that EMT-0 always gives a higher estimate of the averaged total absorptance than RCWA. Based on the studied cases, EMA gives a better approximation for calculating the total absorptance, and can also be easily applied to compute the hemispherical properties. However, one must carefully assess the error introduced by EMA for different nanostructures, polarization, and source spectral distribution.

4.4. Directional Absorptance

The effects of incidence angle on the absorptance are presented in Figs. 4.6 and 4.7, for all cases, at representative wavelengths, i.e., 200, 400, 600, and 800 nm. In the calculation, the RCWA algorithm is used for all cases with gratings. In Figs. 4.6a and 4.6b, Si behaves like a dielectric in the long wavelength region, and the absorptance reaches unity for TM waves at the Brewster angle, where the reflectance is zero. However, the peak absorptance for TM waves at wavelengths of 200 and 400 nm does not reach one because of the large extinction coefficient of Si at these wavelengths (2.9

and 3.6, respectively). For lossy materials such as a metal or Si in the ultraviolet region, there exists a (nonzero) minimum when the reflectance for the TM wave is plotted against the incidence angle. The angle at which the ratio of the reflectance for the TM wave and TE wave is minimized is called the principal angle (Born and Wolf, 1999). Therefore, the absorptance for the TM wave reaches a peak near the principal angle. As shown in Figs. 4.6c and 4.6d, the absorptance for a thin SiO_2 film on top of a Si substrate exhibits a large variation with the angle, especially at short wavelengths. The absorptance oscillation can be explained by interference effects. The phase shift in the SiO_2 film is determined by $\beta = 2\pi d_{SiO_2}\sqrt{n_{SiO_2}^2 - \sin^2\theta}/\lambda$. At $\lambda = 200$ nm, the absorptance minimum is around $\theta = 37^\circ$ that corresponds to $\beta = 5\pi$ and the maximum is around $\theta = 60^\circ$ that corresponds to $\beta = 9\pi/2$. The exact peak and valley locations depend on the polarization.

As can be seen from Figs. 4.6e and 4.6f, the angular dependence of the absorptance for Case A-3 is similar to that for Case A-1. The Brewster angles and principle angles can be clearly seen. Case A-3 also exhibits some distinctly different features from Case A-1. For example, the absorptance at 200 nm is greater than that at 400 nm for TE wave, and the absorptance of 600 nm is greater than that of 800 nm at $\theta < 30^\circ$ and $\theta > 70^\circ$. Other significant difference can be seen in the abrupt changes of absorptance at 200 nm and 400 nm due to Wood's anomaly. When λ = 200 nm, the predicted j = +1 diffraction order from Eq. (4.3) becomes $\theta_{+1} = 90^\circ$ at incidence angle $\theta = 9.6^\circ$. The j = –2 diffraction order becomes $\theta_{-2} = 90^\circ$ at $\theta = 41.8^\circ$. These anomalies are clearly seen in the angular dependent absorptance. Likewise, at $\theta = 41.8^\circ$, the j = –1 diffraction order for λ = 400 nm also appears at the grazing angle.

Figure 4.7 shows the absorptance for cases with poly-Si gates. First of all, the Wood's anomalies also clearly show up for Cases B-1 and B-3 because of the same grating periods used. However, it is difficult to identify Wood's anomaly for Case B-2 because of the complex structures in the angular-dependent absorptance. Next, the B-cases can be compared with the A-cases to examine the effects of the periodic gates. When Case B-1 is compared with Case A-1, the absorptance for TE waves at all four wavelengths increases, especially at λ = 600 nm, which exceeds that at λ = 800 nm. The absorptance for TM waves does not reach unity at the Brewster angle for λ = 600 and 800 nm and the principal angles become obscure for λ = 200 and 400 nm. Figures 4.7c and 4.7d reveal the most complicated behaviors for Case B-2, due to the coupling between the diffraction effects with the interference effect inside SiO_2. A peak absorptance close to unity occurs for the TE wave at $\theta \approx 40^{\circ}$ and λ = 800 nm. On the other hand, the absorptance for the TE wave is the lowest at λ = 600 nm. For the TM wave, the peak absorptance at λ = 600 nm exists at a different angular position compared with that for Cases B-1 and B-3. Although the structure is more complex than that of Case B-2, the absorptance trends for Case B-3 are much simpler than those for Case B-2, as can be seen from Figs. 4.7e and 4.7f. In fact, except the much larger enhancement in the absorptance for Case B-3, the features in Case B-3 are comparable to those shown in Cases A-3 and B-1.

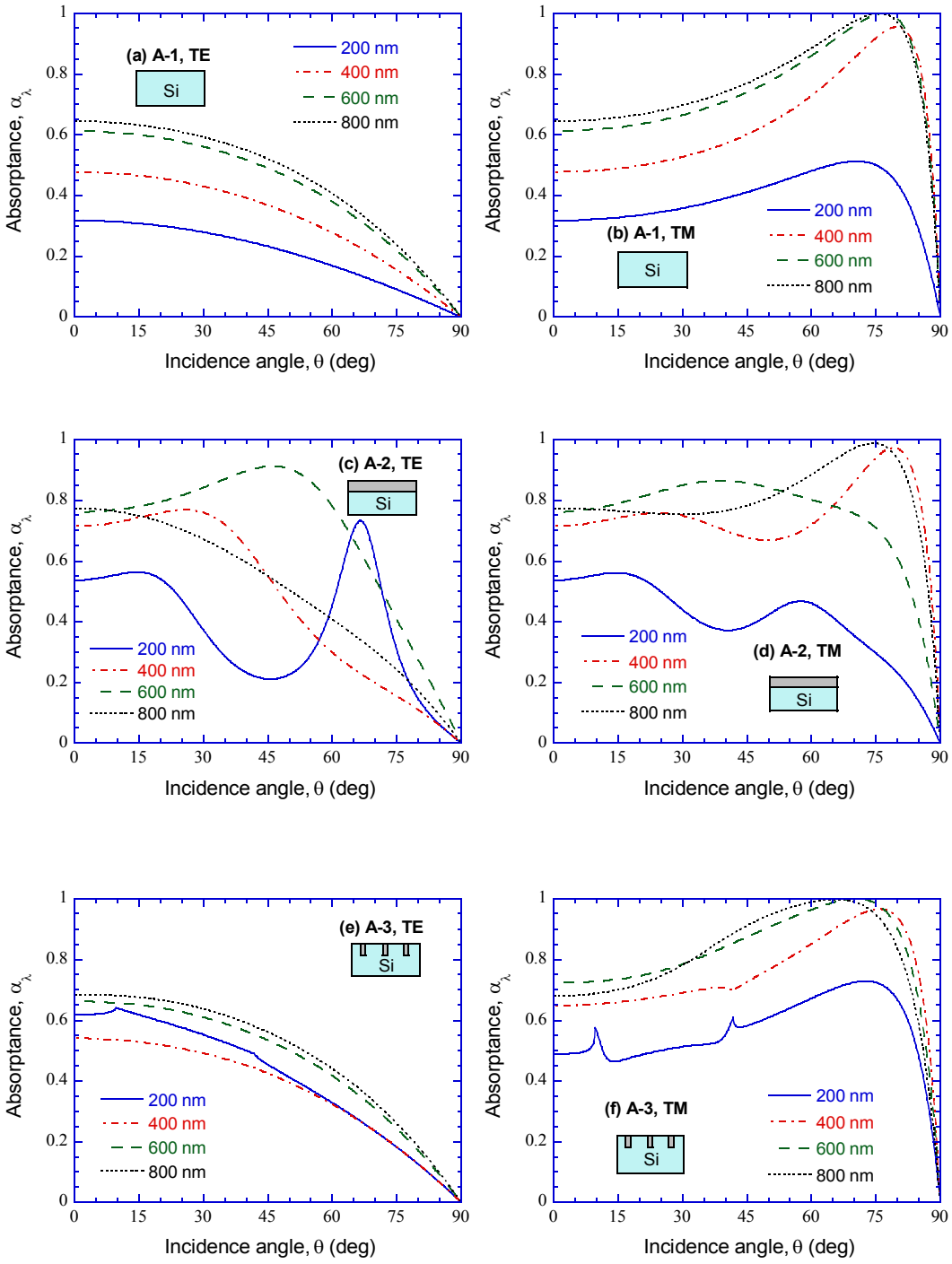

Figure 4.6 Effect of incidence angle on the absorptance at 910°C for cases without gates: (a) TE wave for Case A-1; (b) TM wave for Case A-1; (c) TE wave for Case A-2; (d) TM wave for Case A-2; (e) TE wave for Case A-3; (f) TM wave for Case A-3.

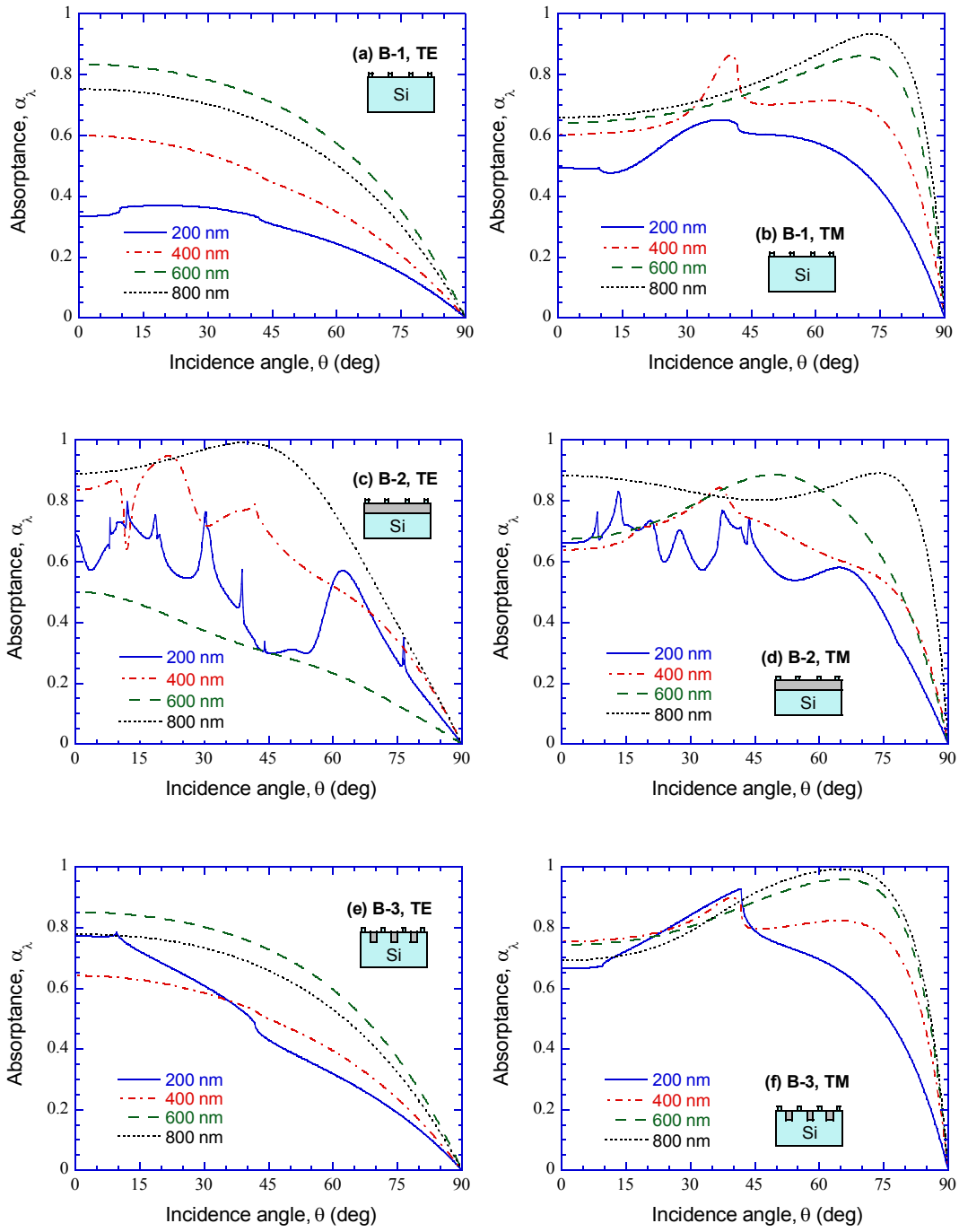

Figure 4.7 Effect of incidence angle on the absorptance at 910°C for cases with gates: (a) TE wave for Case B-1; (b) TM wave for Case B-1; (c) TE wave for Case B-2; (d) TM wave for Case B-2; (e) TE wave for Case B-3; (f) TM wave for Case B-3.

CHAPTER 5

SPECTRAL AND DIRECTIONAL EMITTANCE CONTROL

The second application of micro/nanostructure radiative properties is to actively tailor spectral and directional emittance for energy conversion enhancement. Hence, Chapter 5 will start with a brief review of some micro/nanostructures which have been used for potential application as thermophotovoltaic (TPV) devices. Next, this chapter will propose the concept of a kind of complex grating based on superposition of two simple binary gratings for TPV radiators. The grating with one-dimensional (1D) structured surface is relatively easy to fabricate and the predicted directional-spectral emittance exhibits apparent enhancement over simple grating structures. Specifically, the emittance of the complex grating has a wider peak in the spectral region where the quantum efficiency of TPV cells is high. This enhancement can be explained by the excitation of surface plasmon polaritons coupled with the grating structures. At longer wavelengths, the emittance remains low to reduce the radiative heat transfer from the radiator to the TPV cells by low-energy photons that do not produce any photocurrent. Calculations using the rigorous coupled-wave analysis (RCWA) demonstrate that the emittance peak is insensitive to the direction, suggesting that the proposed structure may be very suitable for TPV applications.

5.1. Micro/Nanostructures for Thermophotovoltaic System

Though responsible for 85% of the world wide energy consumption, fossil fuels have certain drawbacks. Apart from emitting poisonous gases like carbon monoxide, sulphur dioxide and other oxides of nitrogen, they are responsible for increasing the

global concentration of carbon dioxide, which is a primary greenhouse gas. Besides, the fossil fuel reserves are diminishing at an alarming rate. The use of alternative energy sources, recycling of waste heat, and enhancement in the energy conversion efficiency, is therefore critical for reducing the reliance on fossil fuels. TPV devices have been considered as energy conversion systems which allow recycling of the waste heat as well as increasing the conversion efficiency. TPV systems operate on the principle of photovoltaic effect, in which photons whose energy is greater than the band gap of the TPV cell can create electron-hole pairs. The photons come from the radiant energy emitted by the high temperature TPV source, which is called a radiator or emitter. A junction between dissimilarly doped semiconductor layers sets up a potential barrier in the cell and separates the photo-generated charge carriers. This separation induces an electromotive force in the cell and results in electric current (Green, 1982; Fahrenbruch and Bube, 1983; Messenger and Ventre, 2004). Depending on the emitter temperature, the performance of TPV systems can be optimized by selectively filtering the thermal radiation using a wavelength-selective emitter/filter, according to the bandgap of TPV cells.

The key advantages of the TPV systems over other energy conversion devices are the versatility of the heat source and the absence of any moving parts. Utilization of the waste heat, dumped into the atmosphere by different industries, as energy sources in TPV generators can result in considerable energy savings. Portability, quiet operation, and absence of moving parts have made TPV systems promising for power generation in military applications (Nelson, 2003). Moreover, the spectrum of the emitted radiation can match the bandgap of the cells and reduce the amount of unusable radiation, as compared

to conventional PV systems, thereby achieving higher efficiencies. A variant of TPV systems called microthermophotovoltaic (MTPV) devices has been developed in recent years as power devices for microelectromechanical systems (MEMS) (Yang *et al.*, 2002). Miniaturization of electronic gadgets such as notebook computers, cell phones, iPods, etc., have resulted in increasing demands on the power sources which have necessitated the development of such micro power generators (Xue *et al.*, 2005). However, the most obvious drawbacks of TPV devices are their low conversion efficiency and low throughput due to a large amount of unusable radiation. One possible solution of increasing the power output is the application of the principles of microscale radiation to TPV systems. For example, the efficiency can be increased by using micro/nano structured emitters and filters (Chen and Zhang, 2007).

Recent progress in micro- and nanotechnology has resulted in the use of periodic structures as wavelength-selective emitters in TPV systems. Tungsten is used for most TPV emitters because it is corrosion resistant and can withstand high temperatures. One example is a 2D tungsten grating emitter, which has period of 1.4 μm and depth of 0.18 μm (Heinzel *et al.*, 2000). The normal emittance of the fabricated structure shows emittance of 0.7 at 1200 K and $\lambda = 1.6$ μm. 2D gold grating emitters were fabricated by coating 0.15 μm thick gold on top of a microstructured surface, which has 5.0 μm deep holes and 2.0 μm period (Pralle *et al.*, 2002). The measurement results showed a sharp reflectance dip at 2.0 μm due to the coupling of light with discrete surface plasmon states. Besides, a kind of 2D tungsten gratings for TPV emitters was also studied (Sai *et al.*, 2003). The period and the depth of the structure are 1.0 and 0.75 μm, respectively, while the inner cavity is 0.8×0.8 μm wide. The emittance peak at near infrared region is

caused by confined modes inside the cavities and is promising for TPV emitters. Moreover, 3D tungsten photonic crystals can serve as TPV emitters (Lin *et al.*, 2003). The 3D structure composed of multilayered 1D periodic tungsten rods exhibits high spectral emittance (>0.8) in the range from 1.5 to 1.9 μm. Each rod is 0.5 μm wide and ~0.75 μm high and is spaced 1.5 μm apart.

Unlike the emitter, a wide variety of materials can be used as filters because the filter does not need to sustain very high temperatures. Development of filters for TPV systems originated from metallic meshes. For example, three types of 2D periodic copper grid arrays with square, circular-loop, and cross apertures on thin dielectric films were studied (Wu, 1997). The periods of the three arrays were 2, 0.55, and 0.41 μm and the filter exhibited high transmittance in the spectral region from 1.6 to 2.0 μm while filtering out photons at other wavelengths. This kind of wavelength-selective filters takes advantages of electrical current induced in the periodic array to modify its optical properties. Another type of metal grid filters was also proposed recently (Kristensen *et al.*, 2004). The filter was composed of 800 nm thick SiO_2 with 100 nm thick aluminum multiple ring apertures buried in silicon substrate. The rings are in a hexagonal-array with inner diameter of 380 nm and the transmittance of the filter shows a peak of 0.9 at wavelength of 1.5 μm.

Many pure dielectric materials and transparent conducting oxides can also be used as wavelength-selective filters. Silica window has been used as filters in TPV systems (Fraas *et al.*, 2003). A cascaded inhomogeneous dielectric substrate with different refractive index was tailored as wavelength-selective structure (Kiziltas *et al.*, 2005). The free carrier concentration and the thickness effects on the spectral transmittance and

reflectance of the filter have also been studied (Vigil *et al.*, 2005). A filter may be sometimes attached on top of the TPV cells to save space. 1D filter composed of dielectric stack layers mounted on top of a TPV cell is one example (Celanovic *et al.*, 2004). This 1D structure can be optimized for applications in both TPV and MTPV systems with high efficiency and power throughput. The filter has a ten-layer quarter-wave periodic structure, and is based on Si/SiO_2 and Si/SiON material systems. In case of Si/SiO_2 structure, the Si and SiO_2 layers were optimized to be 170 and 390 nm thick respectively (O'Sullivan *et al.*, 2005). These filters were designed for a GaSb TPV cell and exhibited high transmittance at wavelengths below 1.78 μm, while reflecting the photons at longer wavelengths. More recently, a tandem filter in series with highly doped, epitaxially-grown layers was proposed for TPV applications as well (Fourspring *et al.*, 2006). Note that the tandem filter blocks photons of wavelength in the range from 2 to 6 μm, while the epitaxial layer under the filter reflects the photons with longer wavelengths.

5.2. Complex Grating Design for Thermophotovoltaic Radiators

The complex grating design is oriented from the operating conditions and fabrication easiness of TPV radiators. The radiators usually work at an elevated temperature and their spectral emittance should be high at wavelengths between 0.8 and 1.7 μm, where GaSb-related TPV cells have high quantum efficiency (Bett and Sulima, 2003). The high emittance peaks of 1D gratings can be generated by either cavity resonance modes or the excitation of surface plasmon polariton (SPP). For resonance modes, the grooves of the grating should be deep for multiple peaks or a broadband peak. On the other hand, 1D shallow gratings can excite SPP so that the emittance has a peak, which can be further tailored by the surface profile. Because the depth increment can

bring difficulty in microfabrication, SPP is more appropriate than resonance modes for high emittance generation. In order to sustain high temperature and support SPP in the wavelength region of interest, tungsten is selected as the material for the complex grating. Besides, tungsten has been widely used as thermal source with good corrosion resistance.

Since the emittance peak by SPP excitation is usually sharp (Laroche *et al.*, 2005), further broadening of the peak is needed to match the spectral selective criteria of TPV radiators, without significant angular variation. SPP is a coupled, localized EM wave that propagates along the interface between two different media due to charge-density oscillations (Raether, 1988). At the SPP resonance frequency, the EM field can be greatly enhanced near the interface, yielding a strong absorption and a sharp reduction in the reflectance within a narrow spectral band (Park *et al.*, 2005). In other words, the emittance increases steeply because the directional-spectral emittance is the same as the absorptance according to Kirchhoff's law. The requirement of SPP excitation can be met by the incident radiation with a magnetic field component parallel to the grooves. Generally, such a magnetic field component exists in TE waves and TM waves when the PoI is not perpendicular to the grooves (Elston *et al.*, 1991). In the present study, only cases with plane of incidence perpendicular to the grooves are considered for simplicity. Hence, SPP can merely be excited by TM waves to enhance the emittance.

Figure 5.1 shows that a TM wave with wavevector **k** is incident from air on a binary 1D grating. The material of the substrate and the grating ridges is tungsten. The wavevector can be decomposed into two components, k_x and k_z, along the x- and z-axis, respectively. The magnetic field **H** oscillates perpendicular to the plane of incidence and parallel to the grating grooves. The binary grating can be depicted by its period (Λ),

filling ratio (f), and ridge height (h). Although the ridge height is the same as the groove depth (d), the height is adopted here for the understanding easiness of grating profile generation with the base of $h = 0$. In the RCWA model, the reflectance for incident plane waves is calculated by taking a Fourier expansion of the permittivity in the grating region. The angle θ is the corresponding emission angle because the emittance is calculated from the reflectance based on Kirchhoff's law. In order to understand and tailor the emittance spectrum, dispersion curves of 1D gratings are needed.

The variation of the dispersion curves is negligible for small h values compared with the grating period. Hence, the continuous dispersion curve of bulk material in air is a good approximation and the dispersion curve can be expressed as (LeGall *et al.*, 1997):

$$\frac{c^2 k_x^2}{\omega^2} = \frac{\varepsilon(\omega)}{\varepsilon(\omega)+1} \tag{5.1}$$

where ω represents frequency, c the light speed in vacuum, and ε the relative permittivity or dielectric function. The relative permittivity corresponds to optical constants by

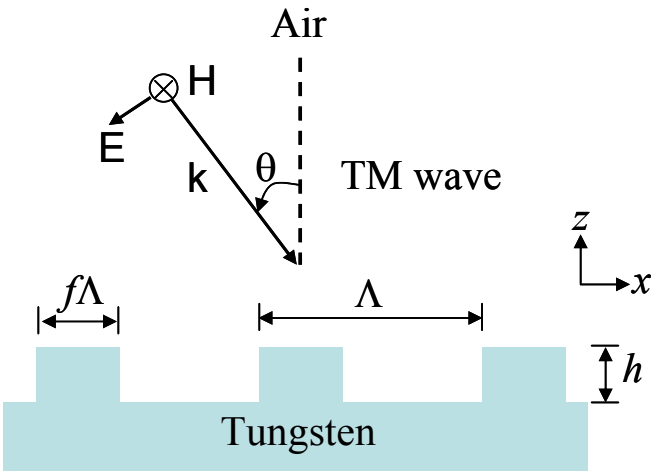

Figure 5.1 Schematic of a binary 1D tungsten grating for a TM wave incident from air at an incidence angle θ, where **k** is the wavevector, **H** is the magnetic field, and **E** is the electric field. The geometry of the binary grating is determined by its period (Λ), filling ratio (f), and ridge height (h).

$\varepsilon = (n + i\kappa)^2$, where n is the refractive index and κ is the extinction coefficient of tungsten. To demonstrate the concept, the room-temperature optical constants of tungsten are taken from Ref. (Palik, 1998) in the present study. Solutions of Eq. (5.1) can be obtained by assuming either k_x or ω to be a real number, and the two solutions are almost identical in the low frequency region. Figure 5.2 shows the dispersion curves of two 1D binary gratings with period Λ_1 = 1.6 μm (solid line with squares) and Λ_2 = 3.2 μm (dashed line with open circles). The present curves are for solutions with a real ω and the real part of k_x. In the figure, the units of ω and k_x are converted to cm^{-1} by dividing $2\pi c$ and 2π, respectively. The dispersion curve of the grating $\omega = f(k_x)$ can be bent into a region $0 \le k_x \le \pi/\Lambda$ due to the periodicity and symmetry. The bending to the reduced

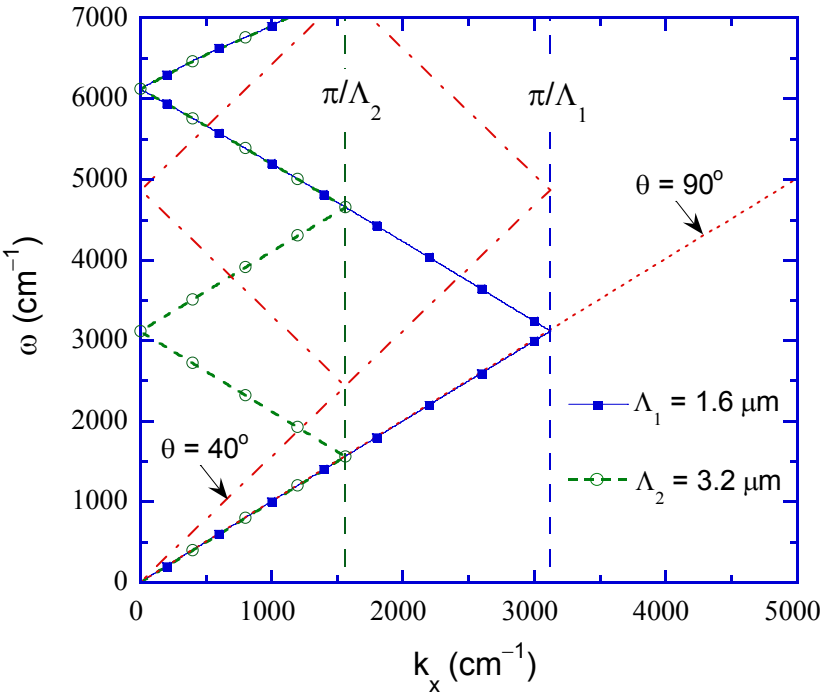

Figure 5.2 Dispersion curves of tungsten shallow gratings for two periods: Λ_1 = 1.6 μm (solid line with squares) and Λ_2 = 3.2 μm (dashed line with open circles).

zone scheme for the even function $f(k_x)$ is given by:

$$f_{j\text{th}}(k_x) = f\left(\sigma k_x + \frac{2\pi}{\Lambda}|j|\right) \tag{5.2}$$

where j is the diffraction order and $\sigma = 1$ for $j \geq 0$ and $\sigma = -1$ for $j < 0$. The branches from the bottom follow the diffraction orders 0, −1, +1, −2, +2, etc. The two vertical dashed lines are $k_x = \pi/\Lambda$ for each period. Note that the dispersion curves come from the same line with partial overlapping due to different periods (Λ_1 and Λ_2) of the gratings. The dashed line corresponds to the light line of $\theta = 90^\circ$, which is not bent to avoid confusion. The dashed-dotted line sections correspond to the light lines of $\theta = 40^\circ$ for the two grating periods. Note that the light line of $\theta = 0^\circ$ overlaps the *y*-axis. The dispersion curve with Λ_1 = 1.6 μm intersects with the light lines of $\theta = 0^\circ$, 20°, and 40° at frequencies of 6120, 4610, and 3830 cm^{-1}, respectively, although the light line of $\theta = 20^\circ$ is not shown in the figure. Hence, one can expect SPP excitation and emittance peaks near the corresponding wavelengths $\lambda =$ 1.63, 2.17, and 2.61 μm. Because the dispersion curve with Λ_2 = 3.2 μm intersects the light line of $\theta = 0^\circ$ at frequencies of 3120 and 6120 cm^{-1}, one can also expect emittance peaks near $\lambda = 3.21$ and 1.63 μm, respectively.

Figure 5.3 shows the spectral emittance of 1D binary gratings of different configurations. The emittance spectra for Λ = 1.6 μm and h = 0.2 μm are presented in Fig. 5.3a with different filling ratios, f = 0.5 and 0.8, at the emission angles $\theta = 20^\circ$ and 40°. Very sharp emittance peaks can be seen at λ = 2.21 μm for $\theta = 20^\circ$ and λ = 2.67 μm for $\theta = 40^\circ$ due to SPP excitation. These wavelengths are within 0.06 μm of those obtained from the dispersion relation as mentioned above. The filling ratio f does not

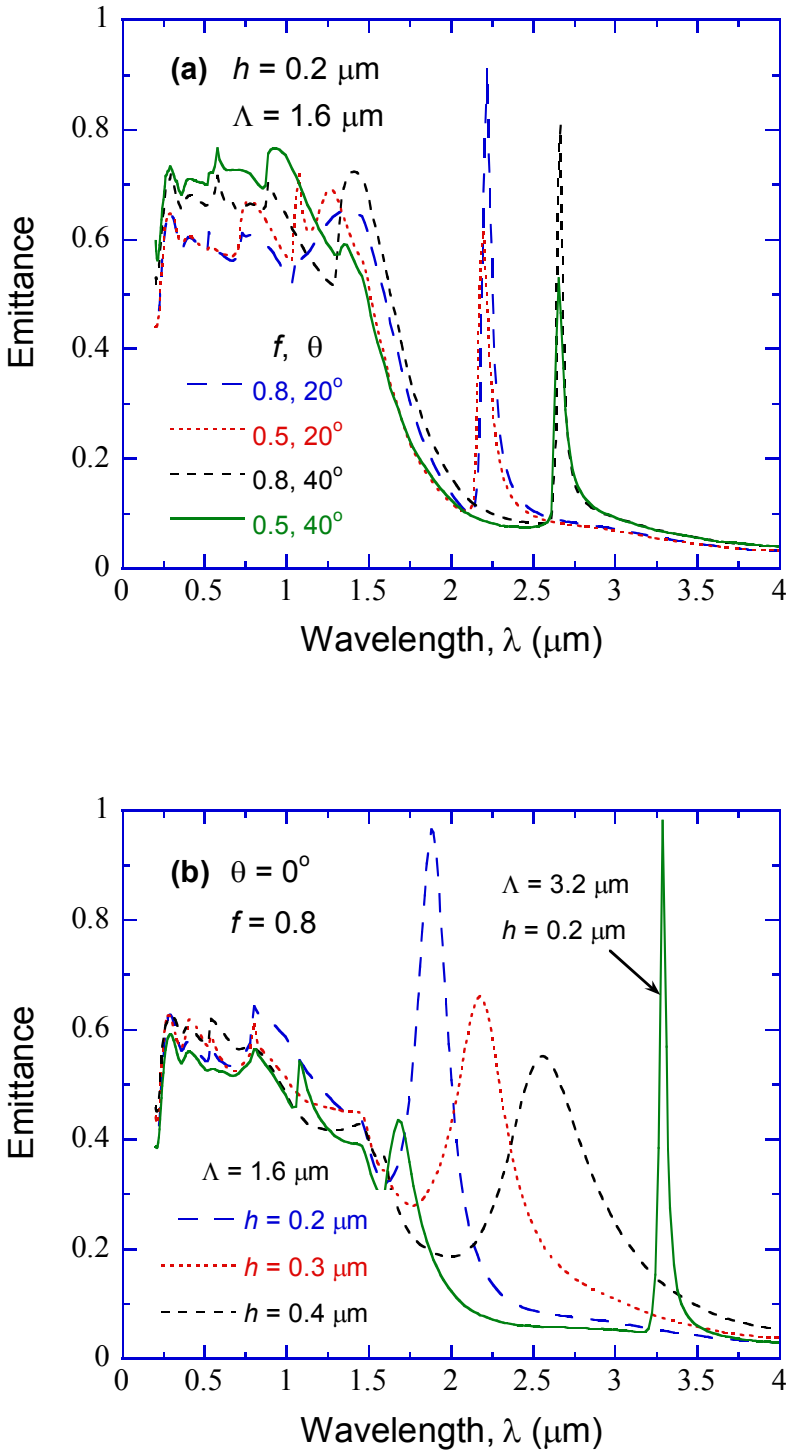

Figure 5.3 Emittance of 1D tungsten binary gratings for TM waves: (a) effects of filling ratio and emission angle for h = 0.2 μm and Λ = 1.6 μm; (b) effects of grating period and height for normal emittance.

affect the peak location but influences the maximum value significantly. There are some variations in the emittance spectra for $\lambda < 1.6$ μm. The reasons are complicated because (i) the variation of the optical constants of tungsten is not monotonic; (ii) there exist cavity resonance modes in this wavelength region; (iii) SPP with higher orders can also be excited. The coupling of these effects makes it difficult to identify their contributions individually.

Figure 5.3b shows the normal emittance with Λ = 1.6 μm and h = 0.2, 0.3, and 0.4 μm. The result with Λ = 3.2 μm and h = 0.2 μm is also shown for comparison. The filling ratio is the same for all four gratings, i.e., f = 0.8. For Λ = 3.2 μm, a sharp peak occurs at $\lambda = 3.29$ μm and a small peak at 1.68 μm, which are very close to those predicted by the SPP dispersion. For Λ = 1.6 μm and h = 0.2 μm, the peak is broader for normal incidence and the location of is 1.88 μm, which is 0.25 μm longer than that predicted by the SPP dispersion curve. The emission peaks are further broaden and shifted towards long wavelengths when h is increases to 0.3 and 0.4 μm. Rigorously speaking, the dispersion curve given in Eq. (5.1) is between two semi-infinite media and may not be applicable for very deep gratings. Laks et al. (1981) showed that the increasing amplitude of sinusoidal gratings can result in split dispersion curves. The influence of filling ratio on the location and width of the emission peak is also complicated. Note that peaks at λ > 1.5 μm cannot attribute to cavity resonance modes because their wavelengths are longer than the maximum resonance wavelength determined by the geometry (Sai *et al.*, 2005).

Though most emittance peaks in Fig. 5.3 can be explained by the dispersion curve of bulk tungsten in vacuum as shown in Fig. 5.2, it can only provide a little hint but cannot provide complete insight information about the emittance peak wavelength and

amplitude shift with grating ridge height. The hint is that the emittance peak corresponds to the cross between the light line and any dispersion curve bending due to the diffraction order. For the spectral range and grating structures of the present work, the emittance peak corresponds to $j = +1/-1$ and $j = -1$ at normal and oblique incidence, respectively. These orders are usually the most dominant diffraction orders with the evanescent fields, which can excite the SPP (Laroche *et al.,* 2005). As a result, the emittance peak wavelength and magnitude may strongly depend on the peak wavelength and magnitude of these diffraction order magnitudes.

Figure 5.4 plots the amplitude of these diffraction orders for detail investigation of the emittance peaks shown in Fig. 5.3. Note that the amplitudes maybe much higher than that of the incidence, but the field magnitude decays exponentially from grating surface and its far-field diffraction efficiency is still zero. Figure 5.4a shows the amplitude of the −1 order diffraction for grating structures with emittance spectra shown in Fig. 5.3a. It is clear that the emittance peaks at wavelength longer than 2 μm matches the peaks of the amplitude very well. In order words, such emittance peaks indeed are caused by SPP excitation due to the −1 order diffraction. On the other hand, the −1 order diffraction is a propagating wave at short wavelengths such that the amplitude peaks do not show high peaks. In Fig. 5.4b, the amplitude of the +1/−1 order diffraction is plotted for grating structures with emittance spectra shown in Fig. 5.3b. Unlike only one diffraction order dominating the SPP excitation at oblique incidence, both the +1 and −1 diffraction orders are identical at normal incidence and excite SPP together. Indeed, the amplitude of those orders shows peaks corresponding to the emittance peaks at the same wavelength. Furthermore, the amplitude peak of the diffraction order shifts to the long

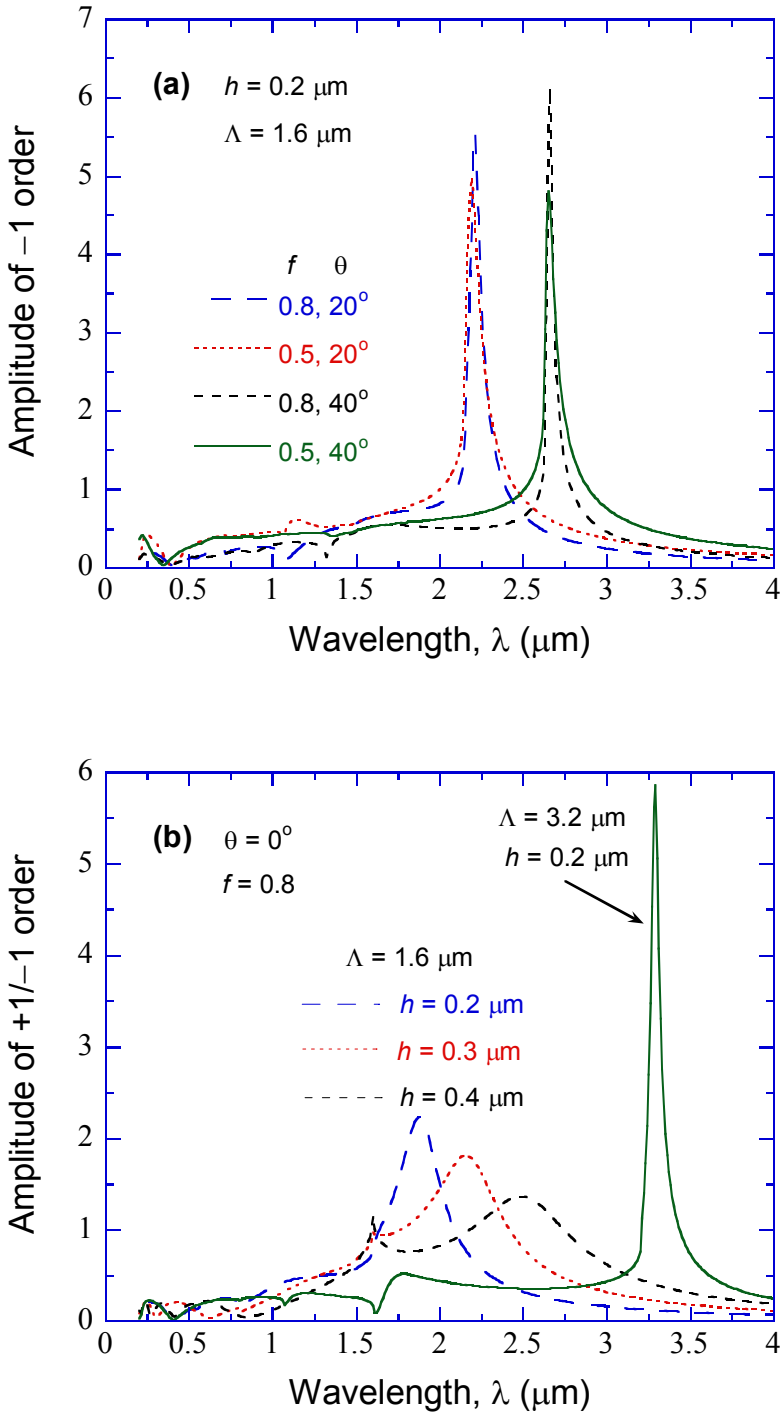

Figure 5.4 Amplitudes of the diffraction order with dominant evanescent fields at different wavelengths: (a) amplitude of –1 order at oblique incidence; (b) amplitude of +1/-1 orders at normal incidence.

wavelength and the peak amplitude decreases as the grating ridge height increases. The similar features are also shown in the emittance spectrum, which provides a clear explanation for the SPP excitation condition modified by the grating ridge height. Actually, the dispersion curve for deep gratings may be generated based on the same principle and employed for radiative property manipulation.

The dispersion curve of a binary grating needs further tuning for a broadband spectral emittance peak with little angular dependence. A broadband emittance can be enabled by multiple intersections between dispersion curves and the light line, while little angular dependence can be enabled by flat dispersion curves at the corresponding frequency. It has been shown that very flat dispersion curves outside the light cone can be formed by the coupling between two opposite sides of the grating on a short-period metal grating (Laks *et al.*, 1981). The introduction of a long-period grating can bend the dispersion curves into the reduced zone with many flat branches, yielding a series of SPP modes (Tan *et al.*, 1999). A broadband emittance peak can thus be achieved and it is less directional dependent. This is the central idea of the proposed complex grating, which is essentially a superposition of a short-period grating and a long-period grating, for application as a TPV radiator. Marquier et al. (2004) used a SiC shallow grating to achieve diffuse emission in a narrow band close to the longitudinal optical phonon frequency of 969 cm^{-1}, where the dispersion curve is flat. The mechanism and operation frequency range are different from the complex tungsten grating proposed here.

Figure 5.5 shows the method of forming a complex grating from a short-period grating, namely simple grating I, and a long-period grating, namely, simple grating II. For clarity, the profiles of the two simple gratings and the complex grating are described by

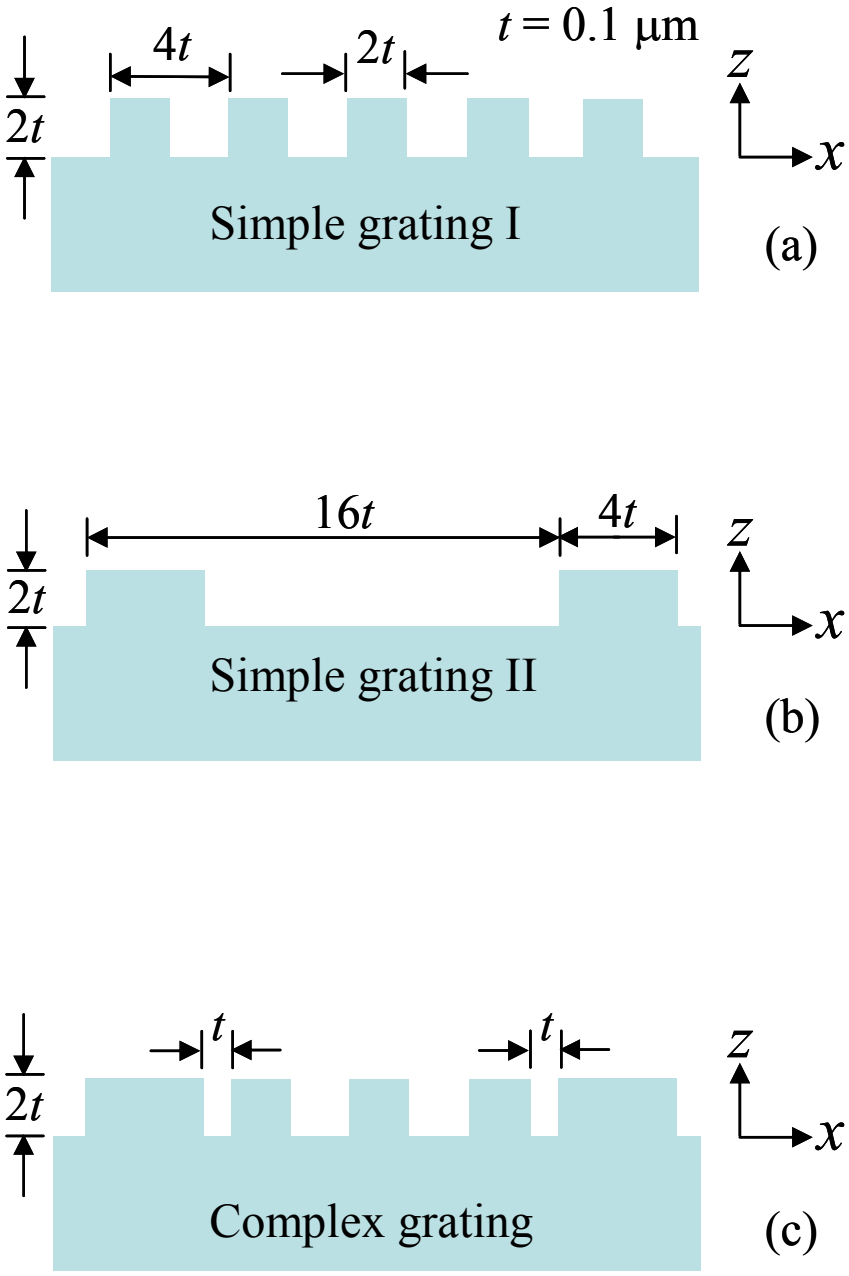

Figure 5.5 Tungsten complex grating formed by superposition of two simple gratings: (a) short-period (Λ = 0.4 μm) simple grating I; (b) long-period (Λ = 1.6 μm) simple grating II; (c) the generated complex grating with Λ = 1.6 μm and ridges of the same height (0.2 μm).

$$z_{\mathrm{I}}(x)=\begin{cases} h_{\mathrm{I}}, & p\Lambda_{\mathrm{I}} \le x < (p+f_{\mathrm{I}})\Lambda_{\mathrm{I}} \\ 0, & (p+f_{\mathrm{I}})\Lambda_{\mathrm{I}} \le x < (p+1)\Lambda_{\mathrm{I}} \end{cases} \tag{5.3a}$$

$$z_{\mathrm{II}}(x)=\begin{cases} h_{\mathrm{II}}, & p\Lambda_{\mathrm{II}} \le x+\phi < (p+f_{\mathrm{II}})\Lambda_{\mathrm{II}} \\ 0, & (p+f_{\mathrm{II}})\Lambda_{\mathrm{II}} \le x+\phi < (p+1)\Lambda_{\mathrm{II}} \end{cases} \tag{5.3b}$$

$$z_C(x)=\max(z_{\mathrm{I}}, z_{\mathrm{II}}) \tag{5.3c}$$

where p is an integer, and ϕ is the lateral shift between grating I and II, and subscripts I, II, and C denote gratings I and II and the resultant complex grating, respectively. Note that the period of the complex grating is the least common multiple of the periods of two simple gratings. After a parametric study, the following geometric parameters are selected. For grating I, $\Lambda_{\mathrm{I}}=4t$, $f_{\mathrm{I}}=0.5$, and $h_{\mathrm{I}}=2t$, where t = 0.1 μm; thus the height-to-period ratio $h_{\mathrm{I}}/\Lambda_{\mathrm{I}}=0.5$. For grating II, $\Lambda_{\mathrm{II}}=16t$, $f_{\mathrm{II}}=0.25$, $h_{\mathrm{II}}=2t$, and $h_{\mathrm{II}}/\Lambda_{\mathrm{II}}=0.125$. A small lateral shift (ϕ = 0.1 μm) is induced so that the complex grating contains ridges of both simple gratings. This way, the dispersion curves of the two gratings may not change significantly and can be coupled to excite multiple SPPs.

Since TPV radiators mostly work at elevated temperatures, the geometry and relative permittivity variations need to be considered. The thermal expansion coefficient of tungsten is low (4.5×10^{-6} K^{-1}). Accordingly, the geometry of the tungsten complex gratings remains almost the same for a large temperature range. The optical constants and emittance of plain tungsten at high temperatures are very similar to those at room temperature for wavelengths shorter than 1.7 μm (Roberts, 1959). Therefore, the predicted spectral emittance peak (0.8 μm ≤ λ ≤ 1.7 μm) of the complex gratings should be applicable at high temperatures also. Due to the data availability, the optical constants of tungsten at room temperature from λ = 0.2 to 4.0 μm are used for the simulation.

5.3. Emittance Modeling

Since the profile of the complex gratings comes from two binary gratings, the normal spectral emittance may have features in common with either of them, whereas the band-folding will form very different emittance features. Figure 5.6 shows the spectral emittance of simple tungsten gratings and the complex grating at emission angle $\theta = 0^\circ$ and 60° for TM waves; the emittance of plain tungsten is also shown for comparison. The normal emittance of plain tungsten is not high enough at short wavelengths such that it cannot be a good TPV radiator. The emittance of the gratings has peaks within the spectral region of interest (0.8 μm ≤ λ ≤ 1.7 μm). Because grating I is a short-period grating with a large h/Λ, the dispersion curve can form multiple branches at a wide frequency range and the corresponding emittance is high in a broad spectral region. The emittance of grating II exhibits a sharp peak and a wide peak. The sharp peak at $\lambda = 1.61$ μm comes from the excited SPP and can be predicted from the dispersion curve. The other peak at λ = 0.99 μm may come from the cavity resonance modes inside the grating grooves. The emittance peak of the complex grating at normal emission is wider than those of simple gratings, especially at long wavelengths. The peak value is higher than 0.8 at $0.8\ \mu\text{m} \le \lambda \le 1.6\ \mu\text{m}$ and lower than 0.2 at λ ≥ 2.2 μm. The emittance of the complex grating is a little higher than that of the plain tungsten at short wavelengths due to the surface structures. However, the emittance is still much lower than the peak and the performance as TPV radiators may not degrade much. In short, the normal emittance of the complex grating gives promising results.

Figure 5.6b shows the emittance at $\theta = 60^\circ$ to express the spectrum at large emission angle. The emittance at short wavelengths (λ ≤ 1 μm) is higher than that at

$\theta = 0^\circ$ for plain tungsten and tungsten gratings. In the wavelength region of interest, the emittance of plain tungsten and two simple gratings are close to one another. The only significant difference is the peak at λ = 1.53 μm for grating II due to the SPP excitation. The peak is very close to the wavelength λ = 1.52 μm, which can be predicted from the intersection of the dispersion curve and the light line of $\theta = 60^\circ$ (not shown here). Another emittance peak for grating II occurs at wavelength λ = 3.01 μm, which is also close to the predicted wavelength of 2.99 μm due to SPP excitation. For the complex grating, however, the peak at λ = 1.53 μm is merged into a shoulder due to multiple SPP excitations. Furthermore, the emittance of the complex grating is the highest at $\lambda > 0.75$ μm with values exceeding 0.7 at λ < 1.5 μm. Note that the groove depth of the two simple gratings is the same and each dispersion curve may jointly contribute to SPP excitations. For example, the emittance has features different from those of other gratings due to the bending of dispersion curves for simple grating I. Another example is the sharp peak at λ = 3.06 μm, which is close to that for simple grating II due to SPP excitation with a slight shift. Except of the peak, the emittance of the complex grating at long wavelengths ($\lambda \geq$ 2.2 μm) is lower than 0.2. Hence, the complex grating is also advantageous for TPV radiators at large emission angles.

The directional emittance is compared at fixed wavelengths to examine the angular dependence in more detail. Figure 5.7 shows the directional emittance of the plain tungsten, simple gratings I and II, and the complex grating. The selected wavelengths are 1.0, 1.6, and 2.2 μm, which are represented by the short dashed line, long dashed line, and solid line, respectively. For a TPV radiator, wavelengths of 1.0 and

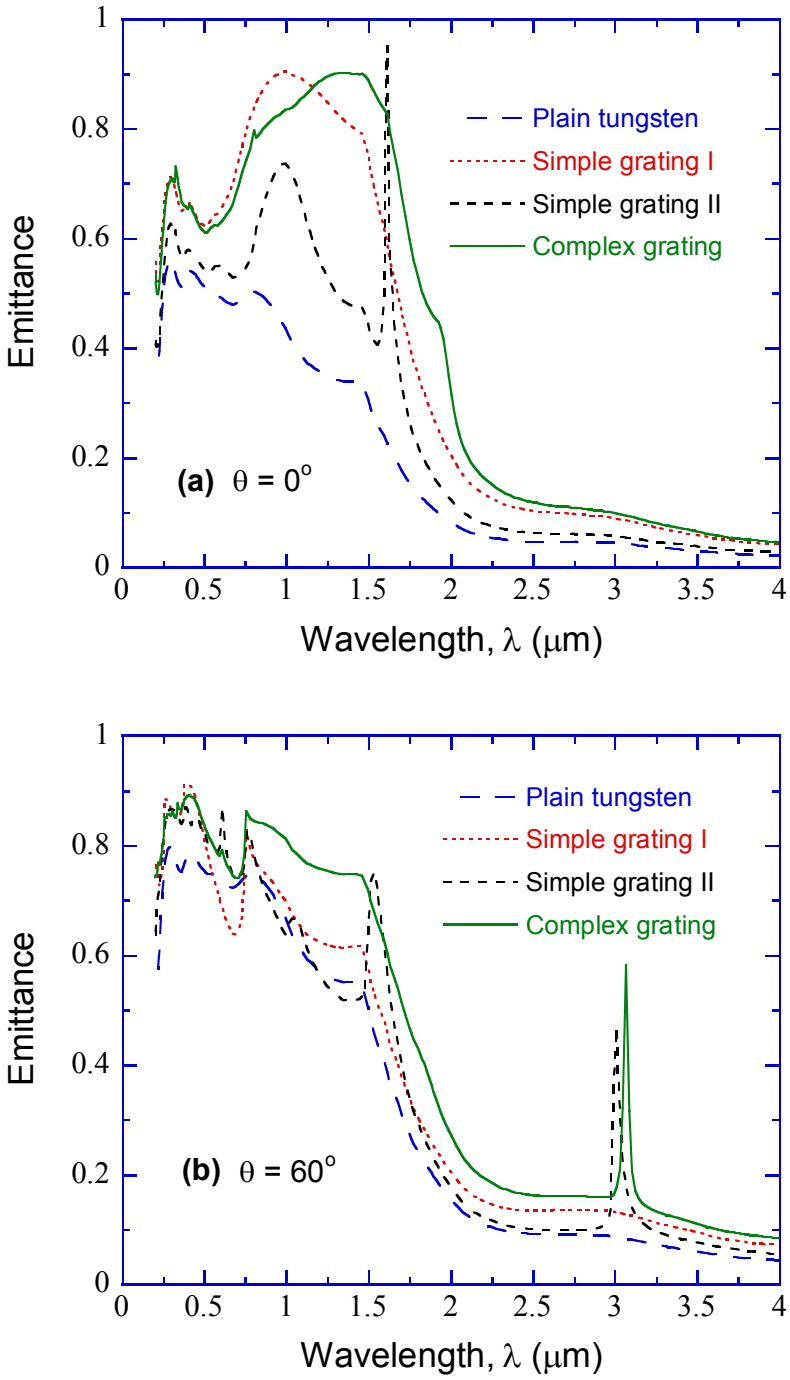

Figure 5.6 Spectral emittance of plain tungsten and tungsten gratings for TM waves at (a) $\theta = 0^{\circ}$ and (b) $\theta = 60^{\circ}$.

1.6 μm symbolize the emission peak edges at the wavelength region of interest. On the other hand, the wavelength of 2.2 μm may represent the behavior at longer wavelengths. Hence, the emittance at 1.0 and 1.6 μm should be high but that at 2.2 μm should be low; moreover, the emittance should be insensitive to angle. Figure 5.7a shows that the emittance of plain tungsten decreases as the wavelength increases, but increases with the emission angle up to a maximum and then drops fast to zero when the angle is close to 90°. In Fig. 5.6b, the emittance of grating I at 1.0 μm is the highest with values greater than 0.7 from $\theta = 0^{\circ}$ to 60°. The emittance at 1.6 μm within the same angles is higher than 0.5, while the emittance at 2.2 μm is lower than 0.2. Based on Fig. 5.7b, one may expect an emittance peak at $\lambda = 1.0$ μm for single grating I, but the peak is not wide enough to cover wavelengths up to 1.6 μm.

Figure 5.7c shows the directional emittance of simple grating II with some interesting features due to the SPP excitation and Wood's anomaly (Hessel and Oliner, 1965). For example, SPP excites at $\theta = 0^{\circ}$ for λ = 1.6 μm and at 20° for λ = 2.2 μm, respectively. The two sharp peaks can be predicted from intersections between the dispersion curve and the light lines as previously discussed. On the other hand, several abrupt changes in emittance show up due to Wood's anomaly. The anomaly can cause an abrupt and asymmetric change in the emittance spectrum when a diffraction order appears at the grazing angle. The grating equation in another form is listed below for the anomaly prediction:

$$\frac{\omega}{c}\sin\theta = \frac{\omega}{c}\sin\theta_j + j\frac{2\pi}{\Lambda} \tag{5.4}$$

where θ_j is the diffraction angle. The anomaly happens when the *j*th diffraction order shows up at grazing angle, i.e., $\theta_j = \pm 90^\circ$. Both grating II and the complex grating have a period Λ = 1.6 μm, the anomalies can show up at λ = 1.0 and 2.2 μm at different angles. At λ = 1.0 μm, three anomalies happen for at $\theta = 14^\circ$, 22°, and 61°, corresponding to $j = 2, -1,$ and 3, respectively. When the two anomalies are close enough, the abrupt changes may merge together, such as at $\theta = 14^\circ$ and 22°. At λ = 2.2 μm, an anomaly happens at $\theta = 22^\circ$ (j = 1), which cannot be clearly seen because of the dominant SPP excitation at $\theta = 20^\circ$. For λ = 1.6 μm, which is the same as the grating period, the change of emittance at $\theta = 0^\circ$ is a combined effect of Wood's anomaly and the SPP excitation. Figure 5.7d shows the directional emittance of the complex grating. The directional behavior of the emittance is quite different from that of simple grating II, but the anomalies are at the same angles due to the same period. The values of the emittance of the complex grating are closer to those of simple grating I because their profiles are similar. However, the emittance of the complex gratings is higher than that of either simple grating at the wavelength of 1.6 μm. As a result, the complex grating has a higher and wider peak from 1.0 to 1.6 μm that is also more diffuse. Consequently, the complex grating is more suitable for TPV radiators than other 1D gratings.

Though the emittance spectrum of complex grating is suitable for TPV radiators, fabrication flexibility is also important and may affect its performance in reality. One critical issue in grating fabrication is the control of the ridge height *h*. The emittance of the complex grating with different *h* is also modeled to examine the fabrication flexibility. Note that *h* of the ideal complex grating is 0.2 μm and ±15% variation in *h* is modeled

but not plotted due to high similarity of the spectral features. The peak at normal emission angle shifts to long wavelengths as *h* increases but is still higher than 0.7 at wavelengths from 0.8 μm to 1.6 μm and lower than 0.2 at wavelengths longer than 2.5 μm. Moreover, the emittance at large emission angle $(\theta = 60^{\circ})$ is almost identical to each other. As a result, the proposed complex grating withstands at least ±15% height variation without much performance degradation.

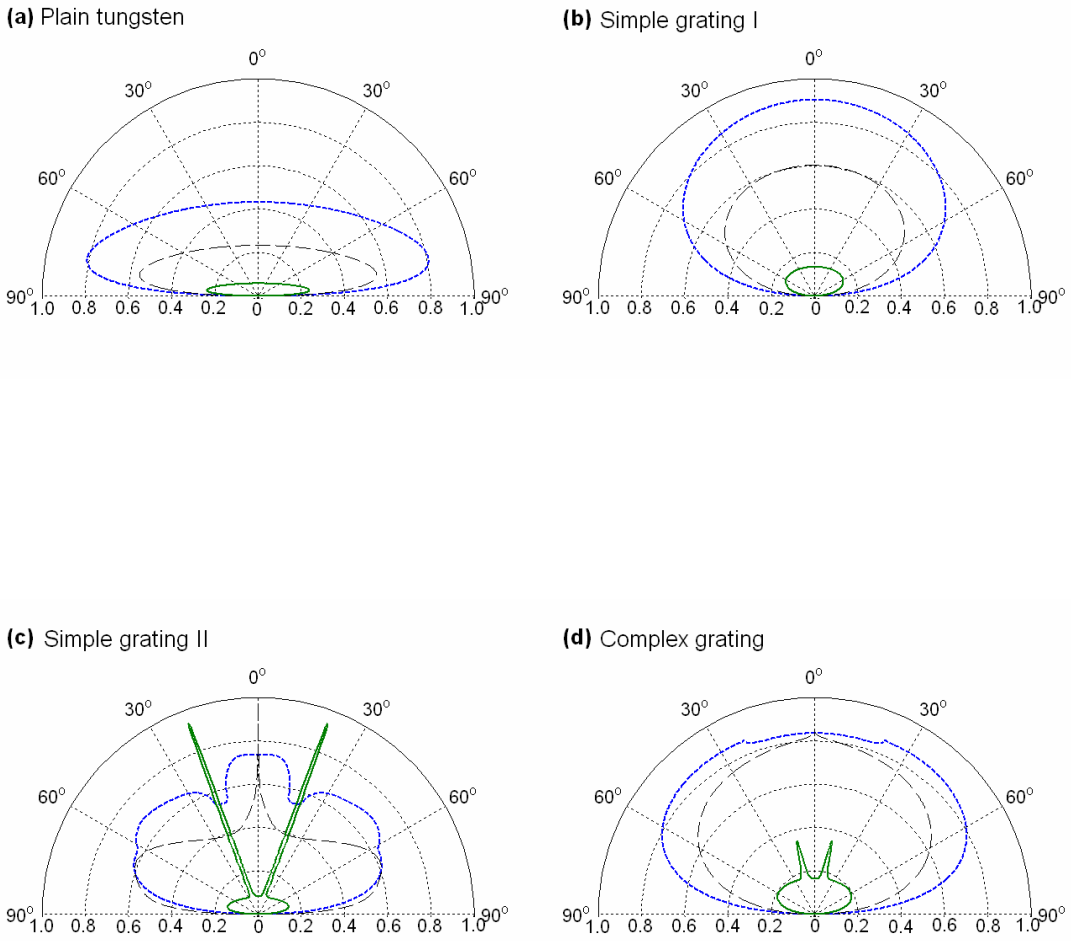

Figure 5.7 Directional emittance for TM waves of $\lambda = 1.0$ μm (short dashed line), 1.6 μm (long dashed line), and 2.2 μm (solid line): (a) plain tungsten; (b) simple grating I; (c) simple grating II; (d) complex grating.

CHAPTER 6

TRANSMITTANCE THROUGH NANOSCALE SLIT ARRAYS

The third application of nanostructure radiative properties is to play more active roles as a mother to generate other nanostructures in a way of nanothermal manufacturing, nanolithography. Nanolithography overcomes the diffraction limit of traditional lithography to generate nanoscale patterns through a photomask with the help of radiation. The success of nanolithography is built on two criterions for incident light, high transmission and local energy confinement.

In Chapter 6, the first part is to systematically investigate the transmission enhancement through nanoscale metallic slit arrays in the wavelength range from visible to mid-infrared. The electromagnetic (EM) field distribution in the near-field regime is analyzed to elucidate three mechanisms for transmission enhancement. Depending on the spectral region, the enhanced transmission can be attributed to Wood's anomaly, cavity resonance, and the effective-medium behavior. The second part of this chapter is to further explore the confinement of mid-infrared radiation into nanometer scales. The confinement shows in a wavelength-independent manner for an aluminum slit array. The Poynting vector and energy density explain the strong localization of electromagnetic energy in the near-field regime. The third part of this chapter is to demonstrate the far-field transmission enhancement experimentally. Different samples of 1D periodic gold (Au) metal slits, with submicrometer period, were fabricated and their transmission was measured using a Fourier transform infrared spectrometer with linear polarizers. The TM

(transverse magnetic) wave transmittance is enhanced in the mid-infrared range, while the TE (transverse electric) wave transmittance is highly suppressed.

6.1. Transmission Enhancement

In order to discuss the transmission mechanism, a vacuum is assumed for the media surrounding the 1D metallic gratings for simplicity, unless specifically mentioned. The transmission enhancement is demonstrated by selecting silver (Ag) as the metal. It should be noted that for practical applications, a dielectric substrate can be used to support the metallic grating structure, and the discussion presented here will still be applicable. The nanoscale metallic grating can be fabricated by lithography (deep UV, X-ray, or electron beam), nano-imprinting, or focused ion beam machining. Metals can be evaporated onto the space patterned by the photoresist and the desired structures remain after stripping the photoresist. Besides silver, gold, and aluminum can be used for a metallic grating with very similar transmission characteristics in the infrared.

Figures 6.1a and 6.1b show the spectral transmittance for a free-standing Ag grating at normal incidence. The grating geometric parameters are set such that Λ = 400 nm, d = 800 nm, and $w = 200$ nm (i.e., the Ag filling ratio $f = 0.5$). The azimuthal angle ϕ is set to 0° such that the plane of incidence (PoI) is perpendicular to the grating grooves. The transmittance is plotted against the wavelength from 0.3 to 9.0 μm for both the TE wave ($\psi = 90^\circ$) and the TM wave ($\psi = 0^\circ$). The tabulated optical constants of Ag in Ref. (Palik, 1985) are used with interpolation. An 800-nm-thick Ag film is essentially opaque in the wavelength region considered, because the radiation penetration depth is less than 50 nm; however, a large transmittance is observed from the Ag slit array at

certain wavelengths for both TE and TM waves. For the TE wave as shown in Fig. 3a, the large transmittance is obtained in the spectral band from 300 to 500 nm. This is due to Wood's anomaly ($\lambda = \Lambda = 400$ nm) and cavity resonance, such that the transmittance peaks are closely located and partly overlap with each other. The transmittance in the IR region is close to zero with the absorptance value less than 0.05; thus, most of the incident energy is reflected back by the Ag grating. On the contrary, the spectral transmittance for the TM wave as shown in Fig. 6.1b exhibits strong enhancement over the wavelength range from the visible to the mid-IR spectral region. Wood's anomaly and cavity resonance result in considerable transmission enhancement, especially at wavelengths less than 2 μm. More cavity resonance peaks are observed for TM waves and their transmittance values are greater than those for TE waves. The peak wavelengths from the cavity resonance shift to the longer wavelength region for TM waves. Interestingly, when the wavelength is greater than 4 μm, the transmittance for TM waves increases monotonically and reaches 0.85 at $\lambda = 9$ μm, suggesting that enhancement is not due to resonance phenomena. The large transmittance enhancement in the mid-IR for TM waves can be explained by the effective medium behavior when $\lambda >> \Lambda$ and will be discussed in detail later.

It should be noted that for the considered Ag slit array, SPP plays an insignificant role in terms of the transmission enhancement. Because the thickness of grating is much greater than the radiation penetration depth, SPPs at two region boundaries (i.e., $z = 0$ and $z = d$) are decoupled. In this case, SPP can only be excited at one boundary since the diffracted evanescent wave cannot reach the other boundary. Accordingly, the excitation of SPP at $z = 0$ mainly contributes to absorption rather than transmission. Here, surface

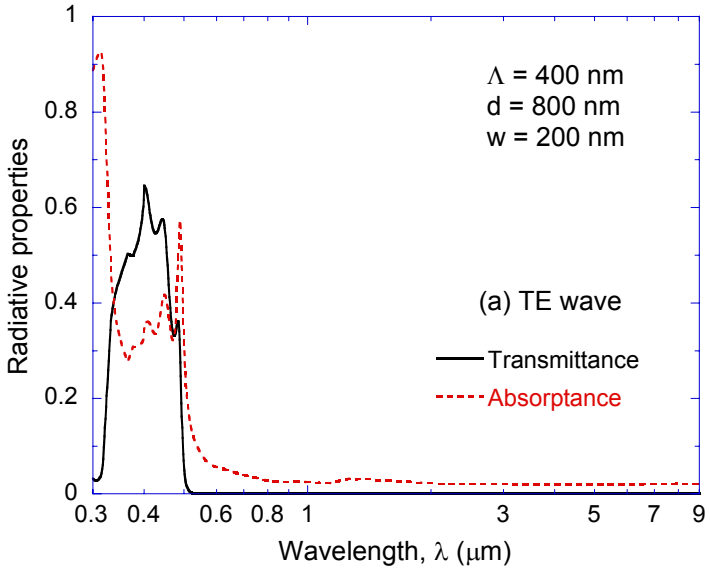

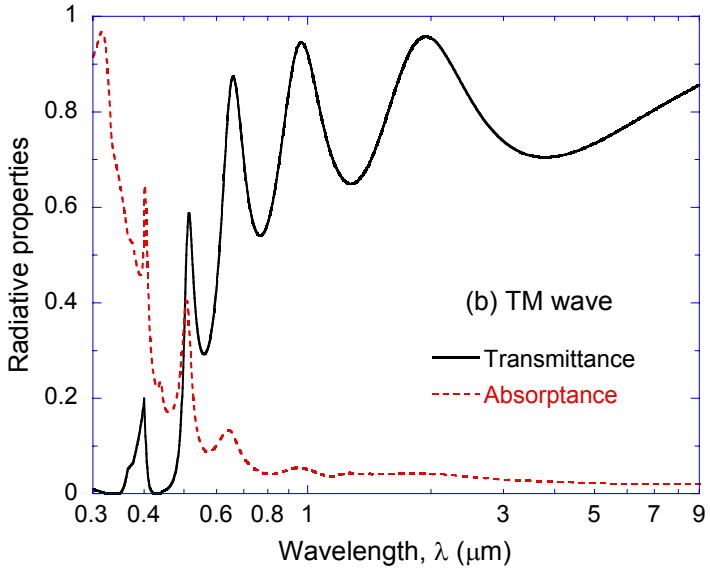

Figure 6.1 Transmittance and absorptance of the free-standing Ag grating with $\Lambda = 400$ nm, $d = 800$ nm, and $w = 200$ nm when the plane of incidence is perpendicular to the grating grooves for: (a) TE wave; (b) TM wave.

plasmon polariton (SPP) occurs at the wavelength very close to that of Wood's anomaly, because the dispersion curve is close to the light line in vacuum (Chen and Zhang, 2007). Consequently, the transmittance at 400 nm for TM waves is less than that for TE waves due to the absorption accompanied with the excitation of SPP, as can be seen from Fig. 6.1b. Therefore, the effect of SPP on the transmission enhancement is not further considered in the present study. Detail discussions about Wood's anomaly, cavity resonance, and the effective medium behavior and their role in modulating the radiative properties are provided below.

6.1.1. Wood's Anomaly

Wood's anomaly occurs when a diffraction order shows up at the grazing angle. The radiative properties abruptly change at the wavelength corresponding to Wood's anomaly because the light intensity will be redistributed when a new propagating diffraction order appears. Originally, Wood's anomaly was studied for grating structures on a semi-infinite substrate, such that its effects were prominent in the reflectance spectrum (Hessel and Oliner, 1965), and a few studies dealt with Wood's anomaly on the transmittance (Ghaemi *et al.*, 1998; Azad *et al.*, 2005). In this case, the anomalies in both Regions I and III may affect the spectral transmittance of periodic slit arrays.

For conical diffraction, the *j*th diffraction order appears at the grazing angle (i.e., $k_z = 0$) in Regions I and III when $k_{xj}^2 + k_y^2 = k^2$ because both regions are set to be vacuum. Recall that the *x*- amd *y*-component of the wavevector for arbitrary azimuthal angle ϕ and zenith angle should satisfy the equations below:

$$k_{xj} = \frac{2\pi}{\lambda}\sin\theta\cos\phi + \frac{2\pi}{\Lambda}j \tag{6.1a}$$

$$k_y = \frac{2\pi}{\lambda}\sin\theta\sin\phi \tag{6.1b}$$

where j is the diffraction order, Λ is the grating period, and λ is the wavelength. Using Eqs. (6.1a) and (6.1b), Wood's anomaly can be predicted from the following equation:

$$\left(\frac{\lambda}{\Lambda}j\right)^2 + 2\frac{\lambda}{\Lambda}j\sin\theta\cos\phi - \cos^2\theta = 0 \tag{6.2}$$

Since Wood's anomaly occurs due to diffraction, it is obvious that Eq. (6.2) only depends on the grating period regardless of its thickness and filling ratio. Equation (6.2) can be further simplified if the PoI is perpendicular to the grating grooves (i.e., $\phi = 0^\circ$). In this case, ± 1 diffraction orders appear when the wavelength is equal to the grating period at normal incidence as shown in Figs. 6.1a and 6.1b when $\lambda = 400$ nm. Since the considered Ag grating is relatively deep (i.e., $\Lambda / d = 0.5$), Wood's anomaly can be clearly seen for both TE and TM waves. If the grating is relatively shallow, the effects of Wood's anomaly on radiative properties may not be obvious for TE waves as compared to TM waves (Chen *et al.*, 2007). In order to further understand the characteristics of Wood's anomaly, the square of the magnitude of complex magnetic field is plotted in logarithmic scale (i.e., $\log_{10}\left|H_y\right|^2$) for TM waves at two wavelengths very close to that associated with Wood's anomaly. For TE waves, a very similar field distribution will be obtained if the electric field is plotted.

Figures 6.2a and 6.2b show the magnetic field distribution over two grating periods at $\lambda = 398$ nm ($T = 0.180$) and $\lambda = 402$ nm ($T = 0.141$), respectively, in the vicinity of the Ag grating. The grating geometry is the same as that in Fig. 6.1. The slit regions are located in $0.1\ \mu\text{m} \le x \le 0.3\ \mu\text{m}$ as well as $0.5\ \mu\text{m} \le x \le 0.7\ \mu\text{m}$, and a plane

wave is incident from the below the grating at normal incidence. Wood's anomaly occurs at λ = 400 nm and the transmittance is 0.199. In Fig. 6.2a, the wavelength of 398 nm is a little shorter than the grating period such that the diffraction orders of $j = \pm 1$ propagate to the far field. Since there exists no energy loss in vacuum, the field distribution in Region I (below the grating in Fig. 6.2a) shows very similar patterns in the near field as well as in the far field. In fact, the periodic interference patterns are found in the field distribution in both *x* and *z* directions. Here, the periodic pattern of the field along the *x* direction results from the $j = \pm 1$ diffracted waves, which are propagating nearly along the region boundary (i.e., $k_{xj} \approx k$). Since the plane wave has an infinite wave front, the periodic interference patterns in the *x* direction are observed even if *z* approaches negative infinity from the grating surface. On the other hand, the periodic pattern along the negative *z* direction is due to the interferences among diffracted waves, whose orders are 0 and ±1, as well as the incident wave. The transmitted waves in Region III show very similar interference patterns as in Region I. Notice that when Wood's anomaly occurs (i.e., $k_{xj} = k$ for $j = \pm 1$), the field distribution should be very similar to Fig. 6.2a.

On the contrary, at the wavelength of 402 nm, the ±1 diffraction orders are evanescent waves. As can be seen from Fig. 6.2b, when the distance from the surface is less than 1.5 μm, the interference patterns in Region I are very similar to those in Fig. 6.2a, with periodicity in both *x* and *z* directions. However, the periodic interference pattern in the *x* direction is due to evanescent waves along the boundary. Since the imaginary part of the *z* component of the wavevector is very small for $j = \pm 1$ diffracted waves, the periodic patterns in the *x* direction appear even when $|z|/\lambda \approx 4$. If the

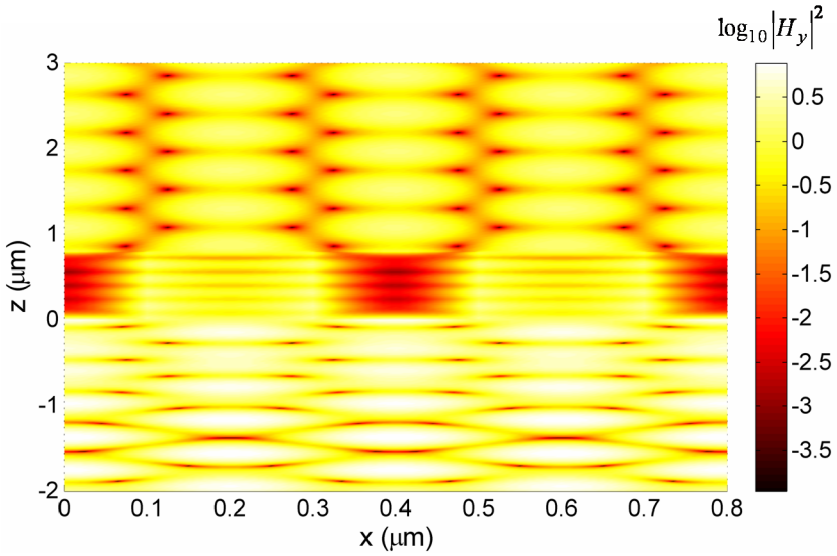

(a) TM wave, λ = 398 nm

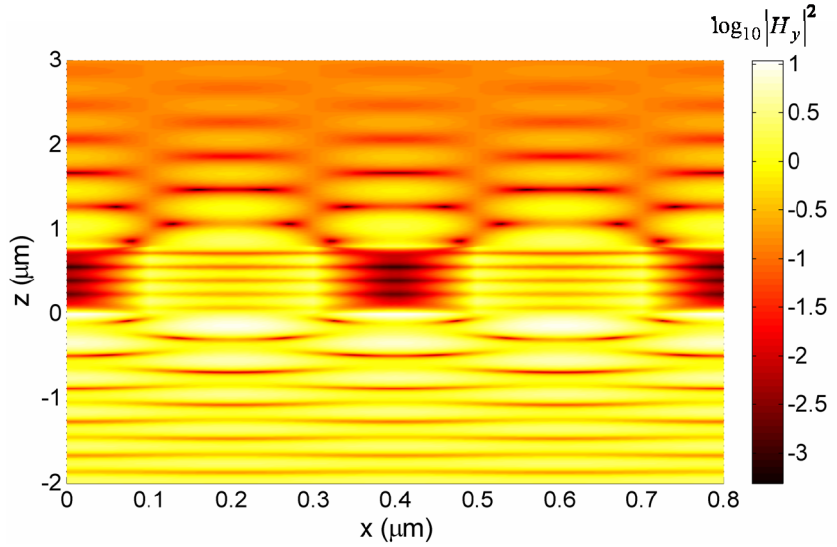

(b) TM wave, λ = 402 nm

Figure 6.2 Square of the magnitude of complex magnetic field in logarithmic scale for TM waves over the two grating periods: (a) $\lambda = 398$ nm; (b) $\lambda = 402$ nm.

distance from the surface further increases, only interference patterns in the z direction remain. In fact, the magnetic field of Region I is greatly affected by evanescent waves in the near field regime and is quite different from that in the far field, where evanescent waves disappear. The magnetic field pattern in the far field is the interference of the zeroth-order diffracted wave and the incident wave. Likewise, the transmitted fields show very similar distributions as in Region I. Consequently, the field distribution in the near-field and far-field regimes clearly indicates that $j = \pm 1$ propagating orders disappear at a wavelength slightly longer than that corresponding to Wood's anomaly. In addition, the near-field distribution reveals very rich features due to the interference between evanescent waves and propagating waves. It should be noted that Wood's anomaly may not always enhance the transmission, and other studies showed that the transmittance could be suppressed (Ghaemi *et al.*, 1998). The effects of Wood's anomaly on the transmittance also depend on the angle of incidence according to Eq. (6.2).

6.1.2. Cavity Resonance

When the cavity resonance occurs, standing waves exist in cavities formed by the grating. At the resonance condition, a strong electromagnetic field exists inside the cavity or slit; it is the confined and enhanced field that subsequently enhances transmission through the gratings. Therefore, several peaks can be observed from the far-field transmittance spectra as shown in Fig. 6.1. Notice that each cavity formed by the grating has two open ends at $z = 0$ and $z = d$. However, the boundary condition requires that tangential field components be continuous, enabling electromagnetic waves to be confined inside the cavity. Consequently, the resonance condition strongly depends on

the geometric parameters of the cavity as well as the boundary conditions. Furthermore, the boundary conditions are complicated functions of geometric parameters. The cavity resonance is not the same as an 1D Fabry-Pérot resonance, whose resonance condition is simply given by $n_c d_c = \text{multiples of } \lambda/2$, where n_c and d_c are respectively the refractive index and thickness of the medium inside the 1D cavity (Born and Wolf, 1999). Therefore, the resonance condition suggested by Refs. (Maruyama *et al.*, 2001) and (Sai *et al.*, 2005) does not properly predict the cavity resonance condition of the gratings studied here. In fact, the standing wave in the cavity is a superposition of all diffracted waves including evanescent waves, and it is not necessary for a single diffraction component to contribute to the cavity resonance. As Lezec and Thio (2004) pointed out for 2D hole arrays, interferences of diffracted evanescent waves must be fully considered to predict the transmittance peak position. To further understand the cavity resonance of 1D gratings, the field distribution is plotted by RCWA in the near-field regime and discussed next.

At selected peak wavelengths, the squares of magnetic and electric fields are plotted for TM and TE waves, respectively, over two grating periods in Fig. 6.3. The grating geometry is again the same as that in Fig. 6.1. Figure 6.3a plots the magnetic field distribution for TM waves when the wavelength is 1950 nm at which the transmittance $T = 0.957$. The slit regions are for $0.1\ \mu\text{m} \le x \le 0.3\ \mu\text{m}$ and $0.5\ \mu\text{m} \le x \le 0.7\ \mu\text{m}$, and the wave is incident from the bottom of the grating at normal incidence. The magnetic field distribution clearly indicates that one anti-node (i.e., maximum of the field intensity) is formed at the center of the cavity. As the wavelength further increases, no cavity mode exists, and thus, the transmittance does not show such peaks. This suggests that the

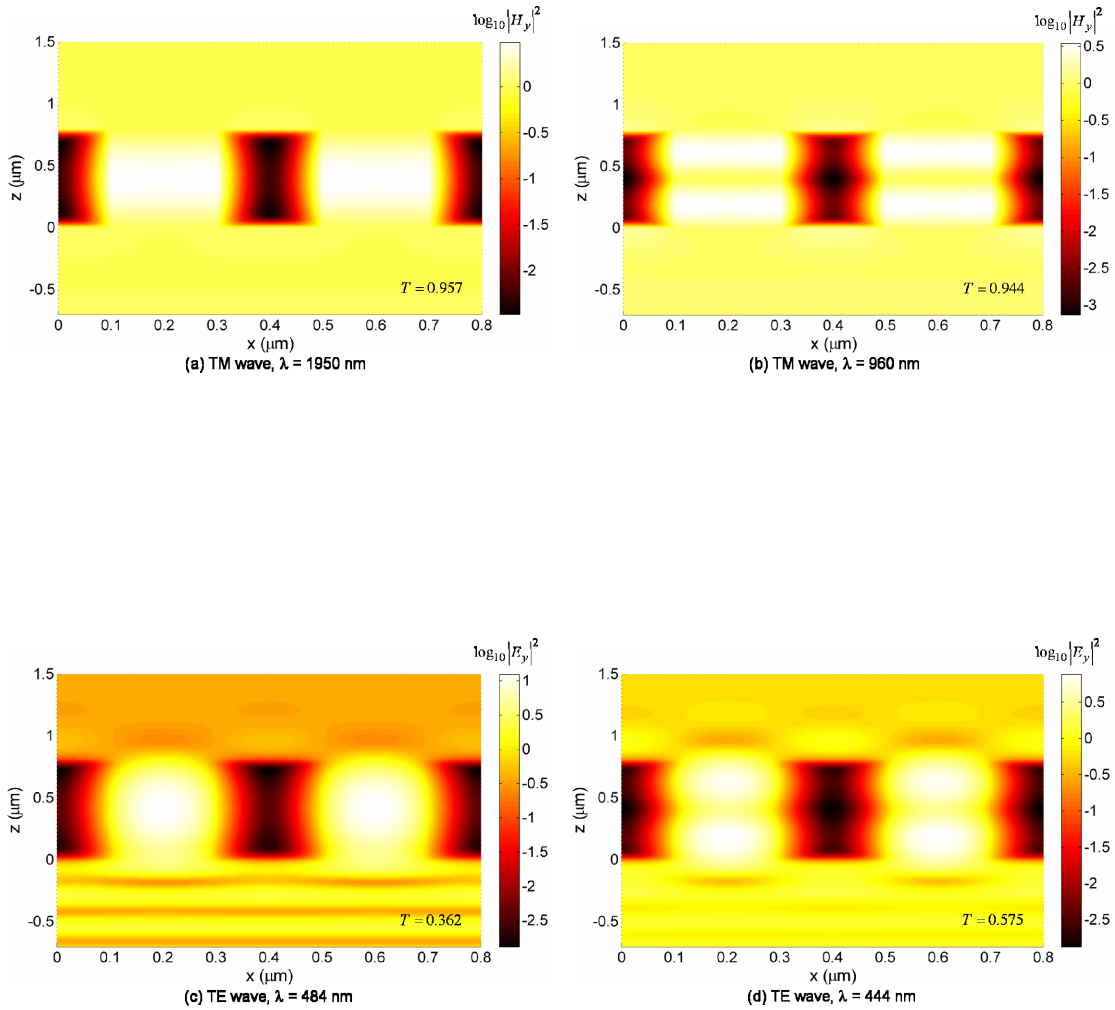

Figure 6.3 Square of the magnitude of complex magnetic field when the cavity resonance occurs for TM waves over the two grating periods: (a) $\lambda = 1950\,\text{nm}$; (b) $\lambda = 960$ nm and that of complex electric field for TE waves: (c) $\lambda = 484$ nm; (d) $\lambda = 444$ nm.

wavelength of 1950 nm corresponds to the cutoff wavelength (upper limit) of the cavity resonance. When the wavelength decreases to 960 nm where the transmittance $T = 0.944$, two anti-nodes are formed in the cavity as illustrated in Fig. 6.3b. The wavelength at which two anti-nodes occur slightly varies from half of the wavelength at which a single anti-node occurs. Such variation comes from the complex coupling of diffracted waves. Even though it is not shown, if the magnetic field is plotted at 1260 nm, where the transmittance dip exists, one-and-a-half anti-nodes are formed in the cavity region. Accordingly, multiple anti-nodes will be found inside the cavity when the wavelength further decreases, corresponding to higher modes (or overtones) of the cavity resonance. However, only low-order cavity resonance modes contribute to the high transmittance peaks, and the transmittance for high-order modes may not necessarily show a high peak.

For TE waves, very similar field distributions are obtained when the transmittance shows peaks as illustrated in Figs. 6.3c and 6.3d. The cutoff wavelength for the TE wave occurs at $\lambda = 484$ nm, which is about one-quarter of the cutoff wavelength for the TM wave. In fact, there are four anti-nodes at 514 nm in the TM wave due to cavity resonance, which is not shown in Fig. 6.3. Interestingly, the wavelength associated with two anti-nodes for the TE wave occurs at 444 nm; this is very close to the cutoff wavelength of 484 nm, suggesting that the frequency at which two anti-nodes occur is far from twice the frequency at which only one anti-node occurs. In addition, the grating becomes almost opaque for TE waves when the wavelength is longer than 500 nm. It can be seen from Figs. 6.3a and 6.3b that, while cavity resonance can enhance the transmittance for both polarizations, the peak locations and the number of anti-nodes are polarization dependent. The enhancement of transmittance for TE waves by cavity

resonance is not as significant as in the case for TM waves. In the following, the effects of geometric parameters, such as the grating thickness, period, and slit width on the resonance condition are separately investigated only for TM waves.

Figure 6.4a shows the transmittance spectra when $\Lambda = 400$ nm and $w = 200$ nm are fixed for $d = 400$ nm, 800 nm, and 1600 nm. As the grating thickness increases, more transmittance peaks are found in the considered wavelength range; and furthermore, the cutoff wavelength shifts to the longer wavelength region. This is related to the standing wave formation with one anti-node similar to what is seen in Fig. 6.3a. The wavelength of the standing wave with one anti-node should be longer when the cavity thickness increases. Though the thickness changes by factor of two, no transmittance peak occurs at the same wavelength for three cases. This supports that the cavity resonance is much more complicated than a Fabry-Pérot resonance.

The effects of the slit width are considered in Fig. 6.4b when the period is 400 nm and the thickness is 800 nm. Although the field distribution in Fig. 6.3 mainly shows node and anti-node formations in the vertical direction, the resonance condition can be affected by the lateral size of the cavity as well. In fact, the x-component of the wavevector of diffracted waves is modified by the grating equation, resulting in nonzero values even at normal incidence. Hence, the standing wave formation in the lateral direction can occur with the presence of diffracted waves. Furthermore, boundary conditions at $z = 0$ and $z = d$ will also be modified as the lateral dimension of the cavity changes. Figure 6.4b clearly shows that the peak wavelengths shift to the shorter wavelength region when the slit width changes from 100 nm to 300 nm. Interestingly, even for the narrow slit when the aspect ratio w/d is 0.125, the cavity resonance still

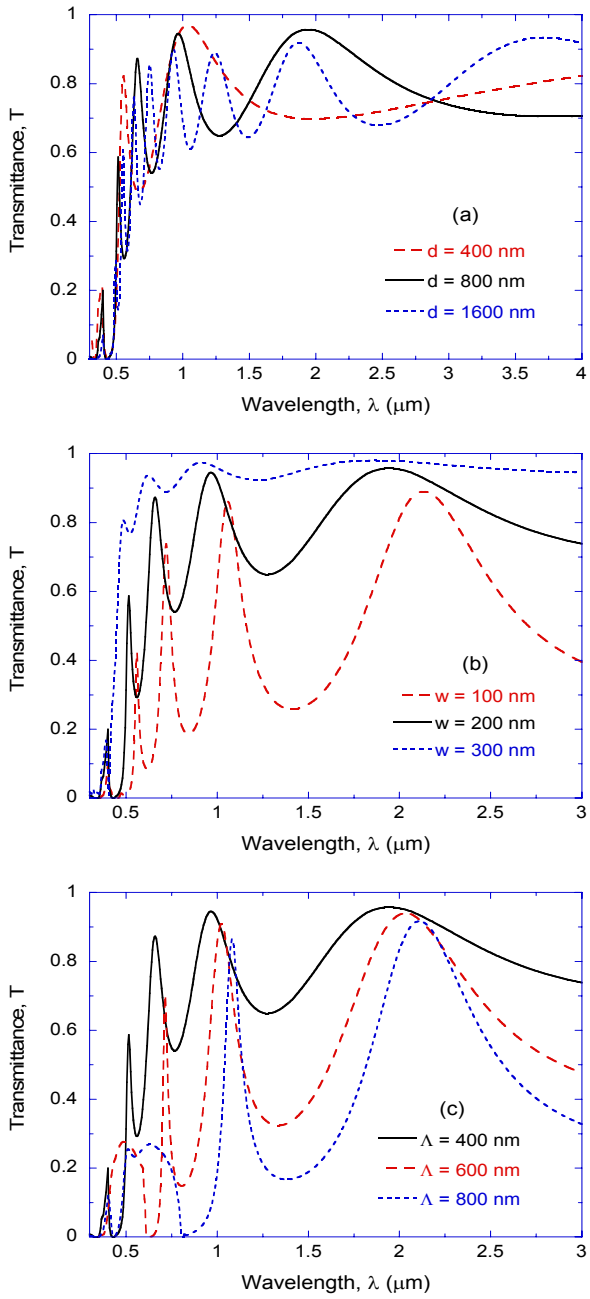

Figure 6.4 Effects of the geometric parameters on the cavity resonance of Ag gratings for TM waves. The geometric parameters of the base case are $\Lambda = 400$ nm, $d = 800$ nm, $w = 200$ nm, and $\phi = 0^{\circ}$. Only one of the parameters is varied in each of the following cases: (a) different thicknesses; (b) different slit widths; (c) different periods.

enhances the transmission through the slit array, allowing the transmittance to be over 0.85. When $w = 300$ nm, the overall transmittance is already very high, such that the cavity resonance does not considerably enhance the transmission. The number of peaks does not change as the slit width changes. Again, the transmittance peak due to Wood's anomaly does not shift in Figs. 6.4a and 6.4b since the grating period remains the same.

Figure 6.4c shows the transmittance of gratings when the grating period is either 400 nm, 600 nm, or 800 nm while $d = 800$ nm and $w = 200$ nm. Unlike the previous structures, the physical size of individual cavity remains the same, and only the lateral size of metal strips changes. Since the grating period changes, the wavelength corresponding to Wood's anomaly accordingly shifts as seen from Fig. 6.4c. The effects of the grating period on the resonance condition are very similar to those of the slit width, such that the transmittance peak wavelength shifts to longer wavelengths as the period increases. As mentioned earlier, standing waves in the lateral direction formed by diffracted waves also contributes to the resonance condition. In terms of the standing wave formation in the x direction, increases in w or k_{xj} (i.e., decreases in Λ) while keeping the other constant have the same effects because the phase shift in the cavity of each diffracted wave is proportional to the product of $k_{xj}w$. Hence, Figs. 6.4b and 6.4c show very similar trends in the transmittance peak wavelengths as w increases or as Λ decreases. Furthermore, the transmittance peak around $\lambda = 600$ nm becomes broader when $\Lambda = 800$ nm. In this case, additional propagating orders $j = \pm 1$ exist based on Eq. (6.1a) because the wavelength 600 nm is shorter than the period. In Figs. 6.4a and 6.4b, however, only the zeroth-order diffracted wave is propagating when the cavity resonance occurs. The existence of the additional propagating diffraction orders may affect the far-

field transmission characteristics, such that the transmittance at cavity resonance becomes broader.

The transmittance of the Ag grating with the same geometric parameters as in Fig. 6.1 is plotted with respect to the wavelength and incidence angle for $\phi = 30^\circ$, i.e., conical diffraction, in Fig. 6.5 for TM ($\psi = 0^\circ$) and TE ($\psi = 90^\circ$) waves, respectively. The inset in Fig. 6.5a depicts the solutions of Wood's anomaly obtained from Eq. (6.2) with a minor (short) branch (j = 1) on the lower-left corner and a major (long) branch (j = –1) that across all zenith angles. Since the excitation of SPP is at wavelengths very close to Wood's anomaly, a reduction of the transmittance due to enhanced absorptance can be seen in the major branch and especially for TM waves. On the other hand, the minor branch of Wood's anomaly may enhance the transmittance for TE waves, as can be seen from the bright region at the lower-left corner of Fig. 6.5b. As can be seen from Fig. 6.5a, oscillations of the transmittance due to the cavity resonance are obvious along the wavelengths for different θ values less than 45°, and the transmittance peak positions are close to those in Fig. 6.1b for $\phi = 0^\circ$. for $60^\circ < \theta < 70^\circ$, the spectral transmittance is greater than 0.8 at wavelengths longer than 1 μm, without visible oscillations. Even when $\theta > 80^\circ$, there exists considerable transmission through the Ag grating with $T \approx 0.6$ at the wavelengths of 875 and 1750 nm. As can be seen from Fig. 6.5b, the transmittance for TE waves exhibits quite different features with much lower values compared with those for TM waves. As shown in Figs. 6.1 and 6.2, the cutoff wavelength of cavity resonance for TE wave is around 500 nm at normal incidence. When $\phi = 30^\circ$, the transmittance values are much higher than those in Fig. 6.1a because H_y is not zero.

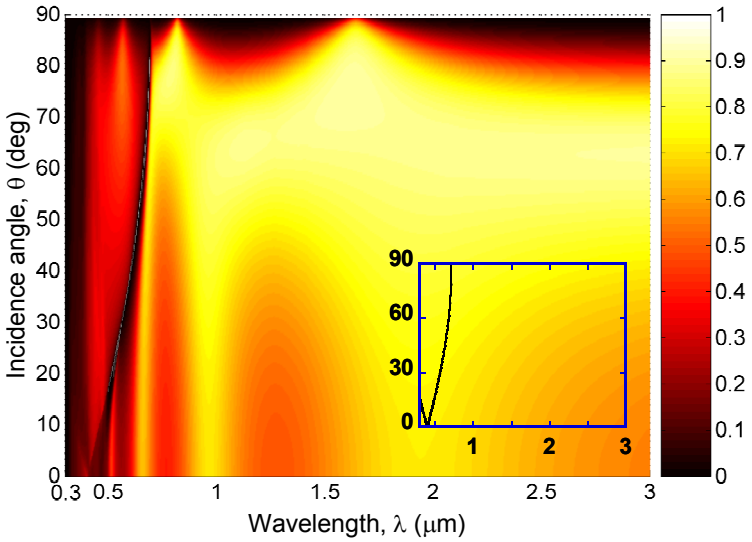

(a) $\phi = 30^\circ$, $\psi = 0^\circ$

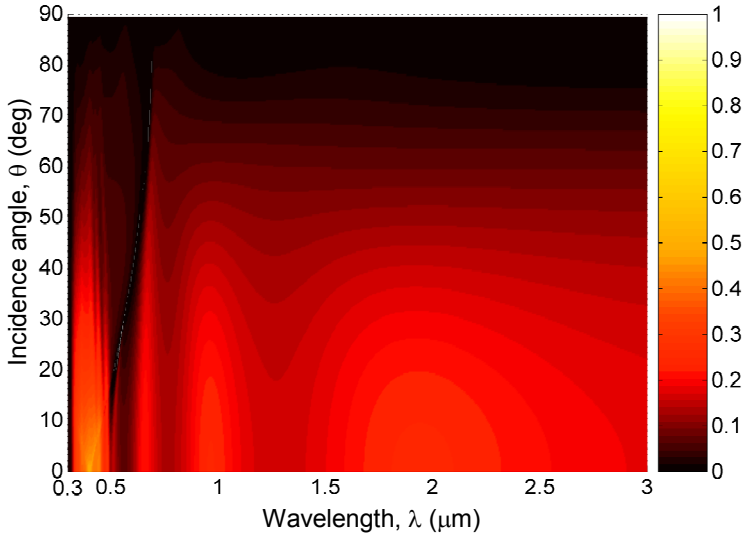

(b) $\phi = 30^\circ$, $\psi = 90^\circ$

Figure 6.5 Contour plot of the transmittance with respect to the wavelength and the incidence angle for the grating with the same geometric parameters as in Fig. 6.1: (a) $\phi = 30^\circ$ and $\psi = 0^\circ$; (b) $\phi = 30^\circ$ and $\psi = 90^\circ$. The inset shows the solution of Wood's anomaly determined by Eq. (6.2).

6.1.3. Effective Medium

A mixture of multiple media or a complicated structure can be homogenized into an effective medium with a specific material property to reduce the computational time with reasonably approximate results (Lalanne and Lemercier-Lalanne, 1996). For 1D gratings, the EMT is applicable only when all diffraction orders are evanescent except the zeroth order (Chen *et al.*, 2007) . Since the grating period in the present work is much shorter than the wavelength in the mid-IR spectral region, the grating (Region II) can be modeled by a homogeneous film of thickness *d*. The zeroth-order effective medium expression has been used for the design of periodic gratings with antireflection effects (Sentenac and Greffet, 1994) or wavelength-selective radiative properties (Glytsis and Gaylord, 1992). However, expressions containing high-order terms of Λ/λ often failed for metallic gratings, resulting in negative values in the imaginary part of the effective dielectric function (Chen *et al.*, 2007). Therefore, the zeroth-order expression is adopted in the present section, and the dielectric functions are given below for both polarizations when the PoI is perpendicular to the grating grooves:

$$\varepsilon_{TE} = f\varepsilon_A + (1-f)\varepsilon_B \tag{6.3a}$$

$$\varepsilon_{TM} = \left(\frac{f}{\varepsilon_A} + \frac{1-f}{\varepsilon_B} \right)^{-1} \tag{6.3b}$$

where f is the filling ratio of medium A, which is Ag in the present study. It is important to note that the dielectric functions depend on the polarization of the incident wave so that the effective medium behaves differently for different polarizations. Furthermore, the grating filling ratio is the only geometric parameter affecting the dielectric function.

Figure 6.6a shows the effective refractive index and extinction coefficient for the TM wave when the filling ratio of the Ag grating is 0.5. The effective extinction coefficient becomes three orders smaller than that of Ag and thus behaves like a dielectric material. On the contrary, the effective extinction coefficient for the TE wave (not shown in the figure) has the same order of magnitude as that of bulk Ag. Consequently, grating behaves like a metal film for the TE wave so that most radiation is reflected. Figure 6.6b shows the transmittance spectra calculated by EMT for Ag gratings with a thickness $d = 800$ nm and filling ratio f = 0.5. Note that the result from EMT (solid line) is independent of the grating period. The transmittance spectra, calculated by RCWA, of two Ag gratings (i.e., $\Lambda = 400$ nm; dashed line and $\Lambda = 800$ nm; dash-dotted line) with the same filling ratio and the thickness are also plotted for comparison. The trend of transmittance predicted from EMT agrees well with those calculated from RCWA, especially at long wavelengths. On the other hand, the deviation becomes large at short wavelengths especially for $\Lambda = 800$ nm. While EMT predicts oscillations due to thin-film interference, it fails to describe the cavity resonance of the gratings in the near-infrared region. The effect of filling ratio on the TM wave transmittance of the Ag slit array is examined with $\Lambda = 400$ nm and d = 800 nm with $f = 0.25$ and 0.75, as shown in Fig. 8c. Though the transmittance by the EMT shows a similar trend as that by RCWA for different filling ratios, the deviation becomes larger as the filling ratio increases. In general, EMT overpredicts the transmittance and the error becomes larger as the filling ratio increases. For the TE wave, the transmittance is very close to zero in the mid-IR region when the filling ratio is greater than 0.05.

The effects of θ are further investigated in the long wavelength region with the

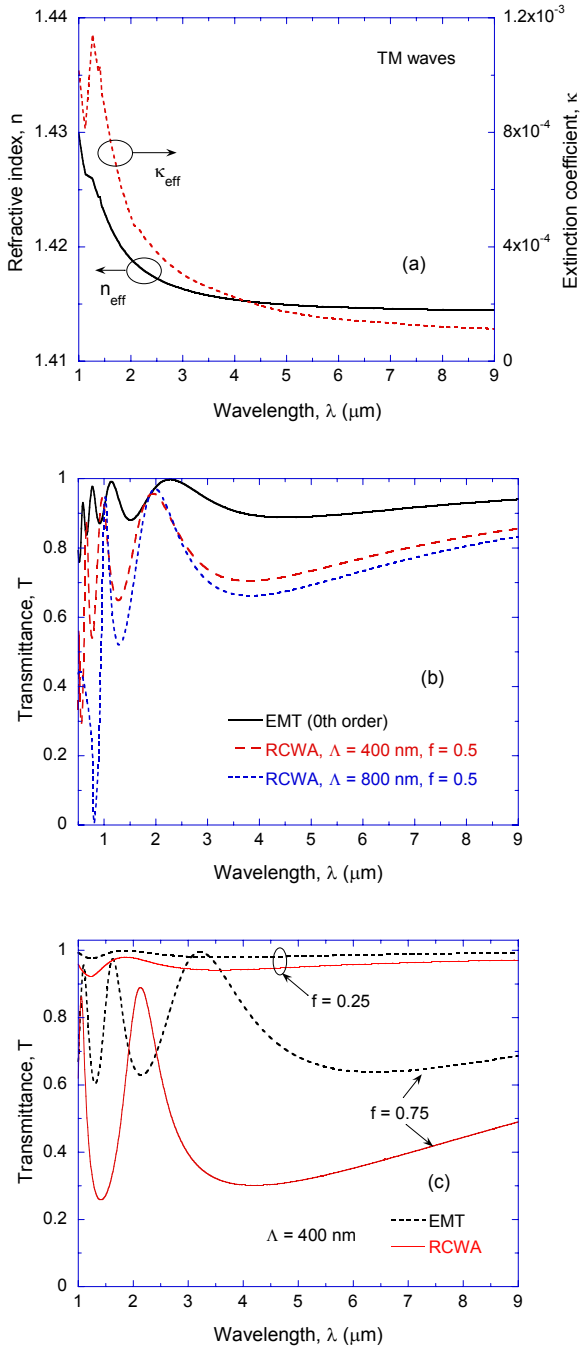

Figure 6.6 Effective medium behavior of the grating structure in the mid-IR spectral region for the TM wave: (a) effective optical constants of the Ag grating with $f = 0.5$; (b) transmittance based on the EMT (solid line) when $\Lambda = 400$ nm , $d = 800$ nm , and $f = 0.5$, and those from RCWA for gratings (dashed line for $\Lambda = 400$ nm ; dash-dotted line for $\Lambda = 800$ nm) with the same f and d; (c) transmittance from the EMT (dotted lines) and RCWA (solid lines) with different filling ratios when $\Lambda = 400$ nm and $d = 800$ nm .

same geometric parameters as those in Fig. 6.1 using RCWA. Figure 6.7 plots the transmittance spectra of the free-standing grating when the PoI is either perpendicular or parallel to the grating grooves. Note that the transmittance spectra for $\theta = 0^\circ$ are identical in Figs. 6.7a and 6.7b. In Fig. 6.7a, with $\phi = 0^\circ$ and $\psi = 0^\circ$, the magnetic field is always parallel to the grooves. Furthermore, k_x increases with θ but k_y remains zero. As θ increases, the transmittance increases in the mid-IR. Similar variations in the transmittance can also be predicted by EMT based on the TM wave, although it is not shown here. The transmittance at large incidence angles ($\theta \geq 60^\circ$) is close to unity in the whole spectrum. It appears that the transmittance peak due the cavity resonance at $\lambda \approx$ 2.0 μm is independent of θ when $\theta \leq 45^\circ$. Notice that only E_x and E_z change as θ varies but H_y remains the same, suggesting that the *y*-component of the magnetic field plays a dominant role in the cavity resonance for TM waves. On the other hand, if H_y changes, the wavelength corresponding to the cavity resonance varies somewhat as shown in Fig. 6.7b, and the spectral transmittance decreases as θ increases. Although Fig. 6.7b is for TE incidence with $\phi = 90^\circ$ and $\psi = 90^\circ$, the electric field is always perpendicular to the grooves. Furthermore, $k_x = 0$ and k_y increases with θ. The situation corresponds to conical diffraction. The magnetic field has a component H_y that is parallel to the grooves. Hence, the transmittance is relatively large in the mid-IR but decreases with increasing θ due to the reduction of the ratio H_y / H_z as θ increases. Therefore, the dependence of transmittance on θ has opposite trends in Figs. 6.7a and 6.7b. In the case of Fig. 6.7b, the EMT formula is not applicable because of conical

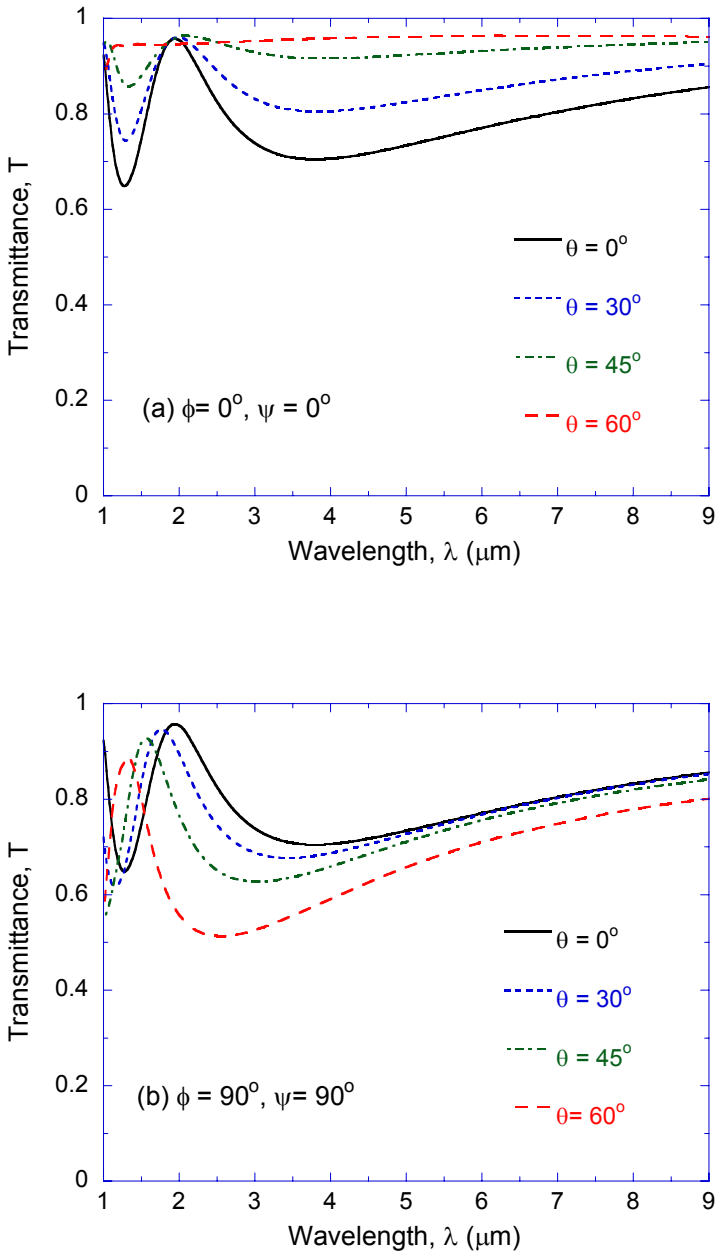

Figure 6.7 Transmittance of the Ag grating with the same geometric parameters as in Fig. 6.1: (a) the PoI is perpendicular to the grating grooves; (b) the PoI is parallel to the grating grooves.

diffraction. When there is a nonzero electric field component E_y ($\phi = 90^\circ$ and $\psi = 0^\circ$), the transmittance becomes very small in the long wavelength region.

Figure 6.8 shows the magnetic field distribution at $\lambda = 8$ μm when the TM wave is incident on the same structure considered in Fig. 6.1. At $\lambda = 8$ μm, the wavelength-to-period and wavelength-to-slit ratios are 20 and 40, respectively. When the grating exhibits an effective medium behavior, the magnetic field in the vicinity of grating does not contain rich features like those of Wood's anomaly and the cavity resonance. Instead, the magnetic-field intensity is nearly uniform around the grating, except the Ag strips where it decays very fast. Figure 6.8 also arrows the time-averaged Poynting vector, defined as $\mathbf{S} = 0.5\,\mathrm{Re}[\mathbf{E} \times \mathbf{H}^*]$, where Re represents the real part of complex quantity.

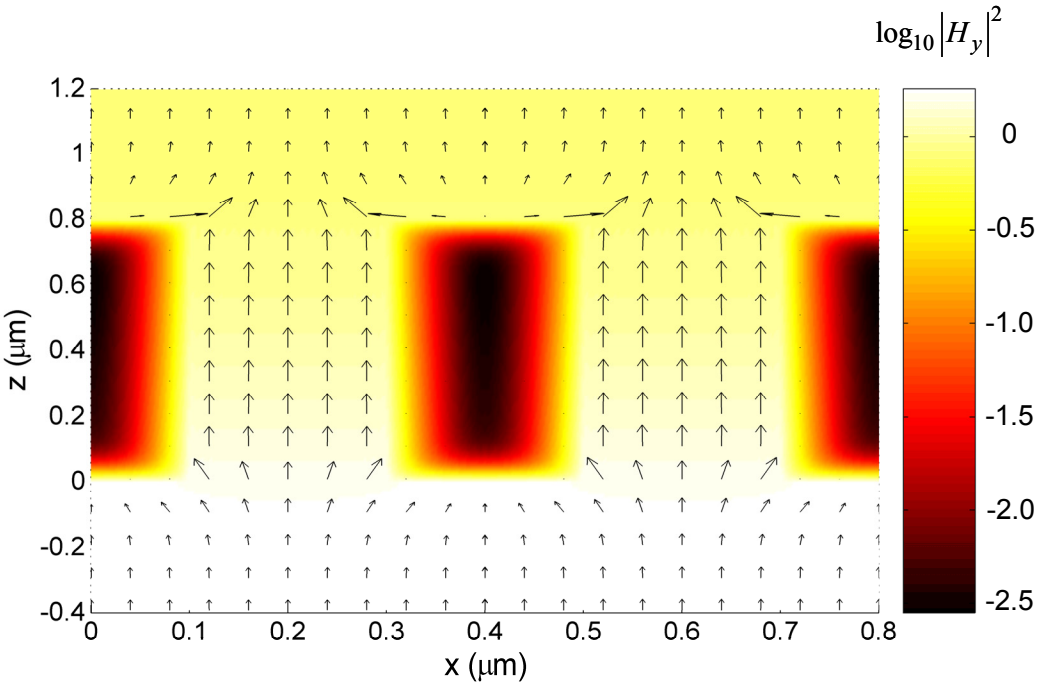

Figure 6.8 Square of the magnitude of complex magnetic field and Poynting vector distribution for TM waves over the two grating periods at $\lambda = 8$ μm.

The arrows represent the directions of the Poynting vector and indicate the path of net energy flow. The magnitude of Poynting vector in vacuum of the grating region is greater than that of Regions I and III, as illustrated by the longer arrows, because energy transferred through Ag strips is negligible. Therefore, the incident energy is squeezed into the narrow slit regions. The Poynting vector distribution quickly evens out within a distance around 200 nm from the grating surface. Note that the Poynting vectors become the largest around the sharp corners of the slits; this may be caused by the abrupt change of material properties at the corner. The figure is a clear illustration of how the IR radiation can be funneled through the nanometer scale grating structures. More detailed discussion about the near-field localization of the IR radiation in the nanometer length scale through the 1D metallic gratings is discussed in the next section.

6.2. Near-Field Confinement

This section is going to show a large transmission enhancement as well as strong localization of the EM fields in the nanometer scale can be achieved from a metallic slit array in the mid-infrared (MIR) spectral region. For TM waves, incident radiation can be significantly confined at the exit plane of the slits with a large transmission enhancement in a wavelength-insensitive manner, offering a great application potential in nanophotothermal fabrication. The polarization-dependent high transmission in a wide MIR spectral band was initially observed from metallic wire grids, which have been used as a polarizer since 1960's (Bird and Parrish, 1960). While the transmittance enhancement for TM waves can be explained qualitatively using an effective medium formulation, solutions based on Maxwell's equations are necessary to understand

localization and near-field confinement. For this reason, the present work uses the RCWA to model the near-field distributions of the energy density and Poynting vector.

For illustration of the concept, a free-standing metallic silt array is schematically depicted in Fig. 6.9a. Unlike previous used silver, Aluminum (Al) is used as the metal film with periodical openings (slits) here due to the available optical constants in the mid-IR region (Palik, 1998) . The slit array is essentially a 1D lateral grating with the period Λ and height d, and extends to infinite in the y direction. The grating period is defined by the widths of Al strip l and the slit w such that $\Lambda = l + w$. A plane wave is incident from the bottom of the grating at normal incidence. The medium surrounding the metallic strips is assumed to be vacuum for simplicity, and effects of a dielectric substrate will be considered later. RCWA is employed to calculate the transmittance and EM fields of the periodic structure. Consequently, the Poynting vector and energy density distribution can be obtained from the calculated EM fields (Lee *et al.,* 2007a).

The spectral transmittance of the Al grating is plotted in Fig. 6.9b for TM waves at normal incidence with the following parameters: $\Lambda = 300$ nm , $d = 100$ nm , and $w = 50$ nm . The transmittance for the TE (transverse electric) waves is essentially zero ($< 0.001\%$) and not shown in the figure. The spectral transmittance modeled by RCWA shows a large enhancement for TM waves in a broad MIR spectral band. For example, at the typical CO_2 laser wavelength of 10.64 μm, a 100-nm-thick Al thin film is essentially opaque because the radiation penetration depth is approximately 9 nm. When 50-nm-wide periodic slits exist in the Al film ($w/\Lambda = 1/6$), however, the transmittance reaches 0.939 for the TM wave and remains nearly zero (2.8×10^{-7}) for the TE wave. The ratio w/λ, where λ is the wavelength of the incident radiation in vacuum, is about $1/200$,

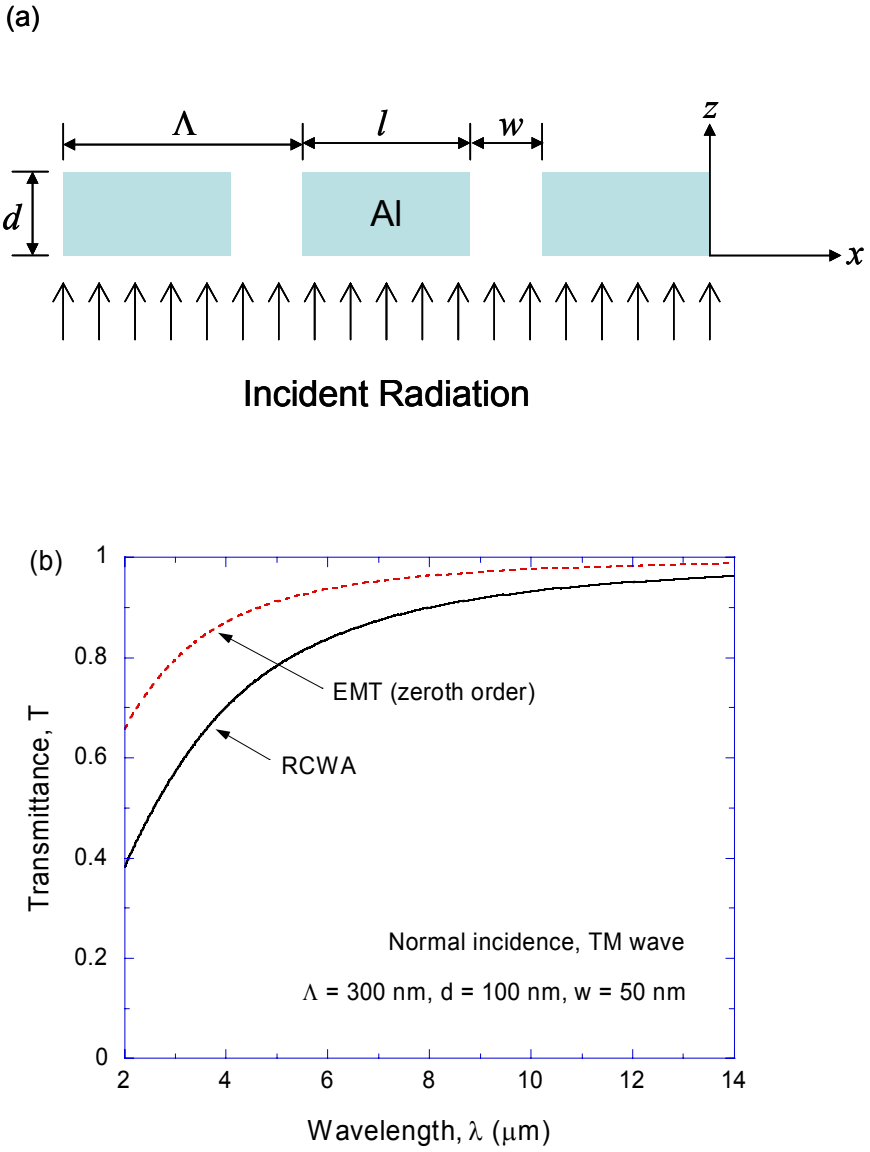

Figure 6.9 Effective medium behavior of the grating structure in the MIR spectral region for the TM wave: (a) the schematic of the Al grating, whose geometry is defined by the thickness d, period Λ, and slit width w; (b) spectral transmittance of the Al grating at normal incidence based on RCWA and EMT. The geometric parameters of the Al grating are $d = 100$ nm, $l = 250$ nm, and $w = 50$ nm, where $\Lambda = l + w = 300$ nm.

which is much smaller than any previous reports (Porto *et al.*, 1999; Treacy, 1999; Marquier *et al.*, 2005). The narrow slits enable TM waves to penetrate through the slit array with little back scattering and absorption losses. The transmission enhancement for TM waves depends weakly on the wavelength of the incident radiation, suggesting that the enhancement is due neither to the cavity resonance nor to the excitation of surface plasmons. Instead, the transmission enhancement through the Al grating in the MIR spectral region can be explained based on an effective medium theory (EMT) (Lalanne and Lemercier-Lalanne, 1996). The transmittance spectrum based on the EMT is also plotted in Fig. 6.9b for comparison. In essence, the EMT treats the grating region as a homogeneous thin film with an effective dielectric function. According to Fig. 6.9b, the transmittance based on the EMT shows the large enhancement, which is also wavelength-independent, like that from RCWA results. On the other hand, the EMT shows consistently higher transmittance values than RCWA in the considered spectral region. When the wavelength becomes much longer than the grating period, the transmittance spectra from RCWA and EMT are getting closer to each other. In the following, emphasis is placed on the field localization of MIR radiation for Al gratings in the near-field regime. The near-field characteristics and the far-field transmittance are obtained.

The energy density in vacuum is shown in Fig. 6.10a over two grating periods for the same Al slit array as in Fig. 6.9. Since the fields in the slit region are of interest, the Al gratings are drawn in a symmetric manner with one or two periods in all illustrations hereafter. The energy density is normalized to that of the incident wave and is plotted in logarithmic scale, i.e., $\log_{10}(u/u_i)$, where subscript i denotes the incidence. The energy density in vacuum can be calculated from

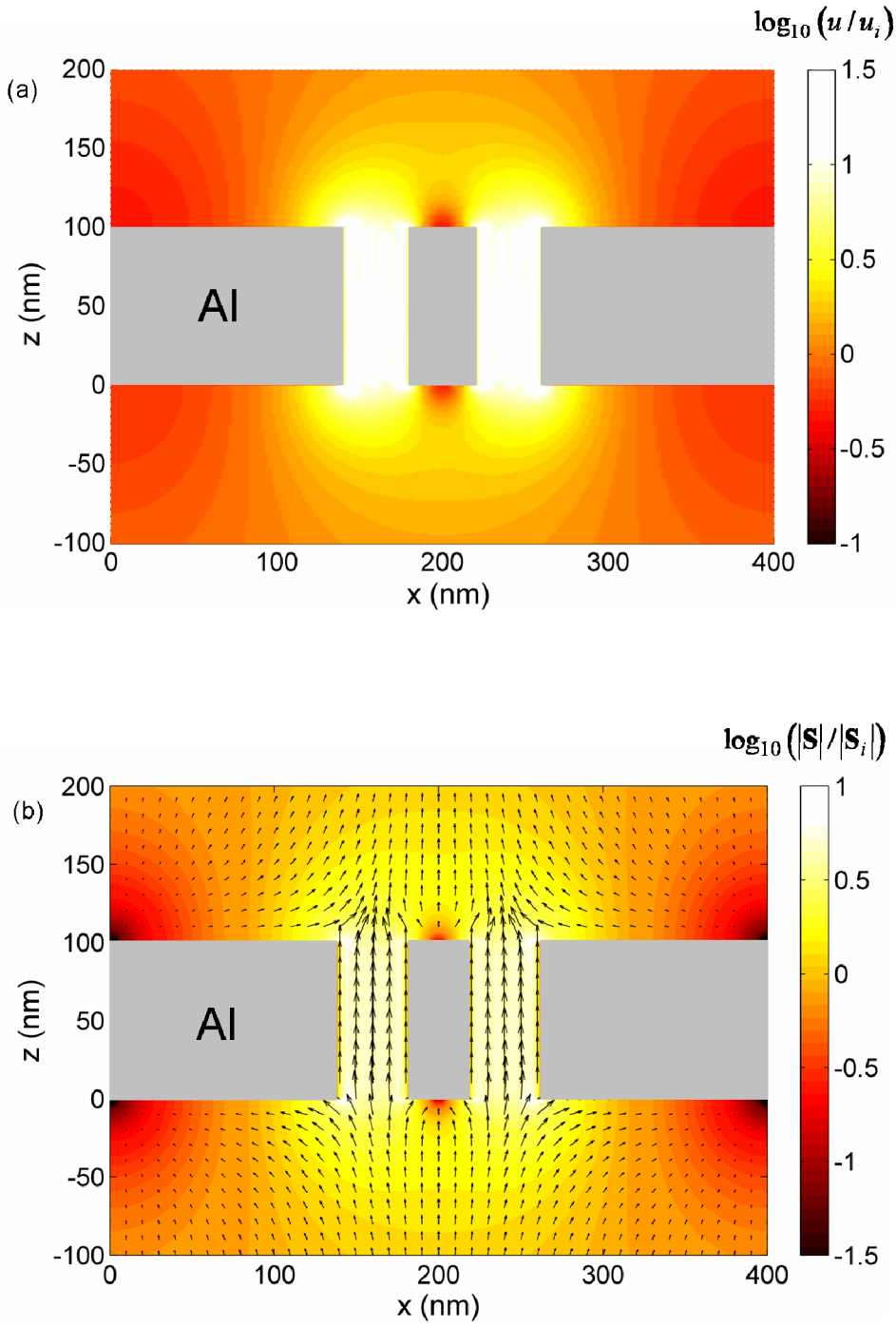

Figure 6.10 Energy density and the Poynting vector distributions for the Al grating with two slits per period SA-2, whose geometric parameters are given in Table 6.1: (a) energy density; (b) Poynting vector.

$$u = \tfrac{1}{4}(\varepsilon_0 \mathbf{E}\cdot\mathbf{E}^* + \mu_0 \mathbf{H}\cdot\mathbf{H}^*) \tag{6.4}$$

where ε_0 and μ_0 are the vacuum permittivity and permeability, **E** and **H** are the complex electric and magnetic field vectors, respectively, and $*$ refers the complex conjugate. The energy density inside the Al strips is several orders of magnitude smaller than that in vacuum and is not shown. As can be seen from Fig. 6.10a, the energy density is highly localized inside the slit region, suggesting that the incident radiation is funneled through the slits. Strong localization is found at the exit plane ($z = d$) of the slit. It is important to note that the localized energy density is a combination of both propagating and evanescent waves. According to the grating equation, also known as Floquet condition, only the zeroth-order diffraction is a propagating wave and the rest are evanescent waves because $\lambda / \Lambda >> 1$. The lateral size of the region with high energy densities is slightly larger than the slit width due to interference effects of the diffracted waves. The region of highly localized energy density extends to approximately 40 nm away from the Al surface. While the enhancement also occurs at the slit inlet, it is the exit that is of interest. Since evanescent waves decay exponentially, the high-contrast localization of fields cannot reach further in the z direction.

Figure 6.10b shows the time-averaged Poynting vector of the same structure as in Fig. 6.10a. The direction of the Poynting vector is represented by arrows, which indicate the path that the incident energy flows through the Al slit array. The magnitude of the Poynting vector, normalized to that of the incident wave, is also shown as the contour plot in the logarithmic scale. Near the exit plane, the Poynting vectors with large magnitudes direct to the region where the energy density is greatly localized. At the incident region, on the other hand, some of the Poynting vectors direct to the sharp edges

of the Al strips. However, most of the incident energy flows through the narrow slits. Since the transmittance of the structure is higher than 90%, the transmitted plane wave in the far-field is nearly the same as that of the incidence. In the near-field regime, the transmitted energy is highly localized around the slits, which act as funnels for the energy flow with an enhanced flux. When the effects of oblique incidence are considered (not shown here) with the wavevector of incident wave still in the *x*-*z* plane at an oblique incidence, a strong field localization can still be achieved at the slit exit. The transmittance increases as the angle of incidence increases to 75°, and then decrease as the incidence angle further increases.

To quantify the field localization effects, we define η_s as the average of the normalized *z* component of the Poynting vector over the slit width at the exit plane, and η_u for the normalized energy density in a similar manner. Here, the normalization is conducted with respect to the incident wave. For the considered Al slit array, the calculated values are $\eta_s = 5.57$ and $\eta_u = 24.2$, suggesting that the 50-nm slits significantly enhance the light transmission as well as the field localization. Since $w/\Lambda = 1/6$, η_s value of 5.57 implies that about 98.9% of the transmitted energy is passing through the slits. Table 6.1 summarizes the calculated η_s, η_u, and transmittance (*T*) for five different slit arrays, which have one, two, or three slits in one period. In Table 6.1, SA stands for the slit array. The geometry of the strip/slit arrays are identified by the widths of the Al strips and slits as *l*'s and *w*'s, respectively.

Figure 6.11 plots the normalized energy density and Poynting vector distributions of SA-2 over one grating period. The geometric parameters are $l_1 = 280$ nm, $w_1 = 40$ nm,

$l_2 = 40$ nm, $w_2 = 40$ nm (i.e., $\Lambda = 400$ nm), and the same height $d = 100$ nm. In the plots, the left strip and right strip are $l_1/2 = 140$ nm to show the grating in a symmetric manner. Two distinct regions of high energy density are formed at the exits of both slits. Though the width of the narrower Al strip is only 40 nm, it separates the two localized EM fields. The Poynting vector distribution indicates that almost all the energy flows through the slits and the exit energy flux is concentrated within the opening and then expands laterally. The short distance in the z direction does not allow a visualization of the expansion of the Poynting vector from the slit region to even out the distribution and eventually reconstruct the plan wave behavior in the far-field regime. As can be seen in Table 6.1, the transmittance of SA-2 is slightly higher than that of SA-1. This is presumably due to the larger value of w/Λ (i.e., smaller value of f) for SA-2. Results calculated from EMT also support the variation of transmittance with different w/Λ.

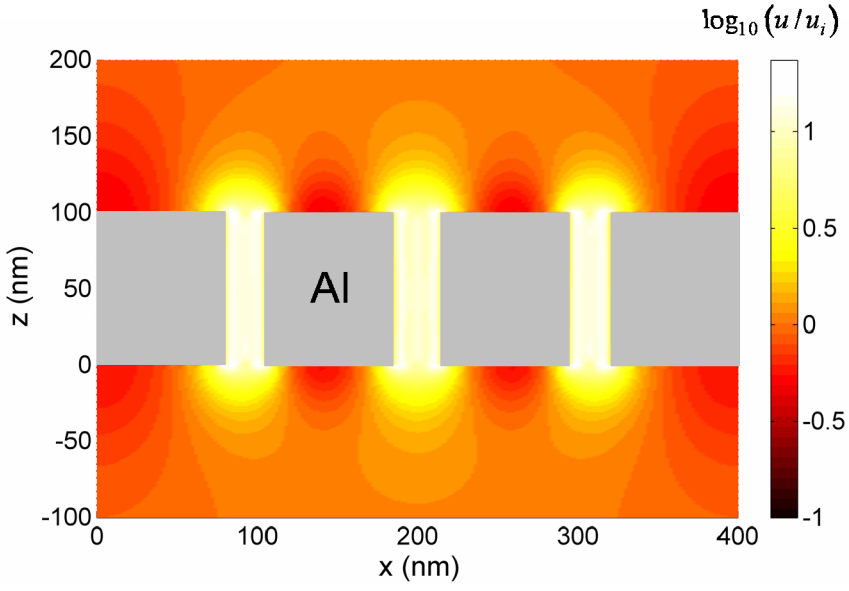

Figure 6.11 Energy density distribution for the Al grating with three slits in a period SA-3.

Table 6.1 Calculated η_s, η_u, and T for slit arrays with 1, 2, or 3 slits per period, for TM waves at normal incidence and $\lambda = 10.64$ μm.

	SA-1	SA-2	SA-3	SA-4	SA-5
Λ (nm)	300	400	400	300	300
l's (nm)	250	280 / 40	160 / 80 / 80	250	250
w's (nm)	50	40 / 40	25 / 30 / 25	50	50
η_s	5.57	4.69 / 4.69	4.82 / 4.51 / 4.82	3.76	3.86
η_u	24.2	15.9 / 15.9	16.7 / 14.3 / 16.7	26.0†	27.2†
T	0.939	0.956	0.968	0.644	0.644

†Values are normalized by the energy density of the transmitted light in the far-field regime

Figure 6.12 shows the normalized energy density of SA-3 over one grating period. The grating period and height are the same as SA-2. The lateral dimensions are $l_1 = 160$ nm, $w_1 = 25$ nm, $l_2 = 80$ nm, $w_2 = 30$ nm, $l_3 = 80$ nm, and $w_3 = 25$ nm. The energy density is highly localized near the three exits, with the minimum width of less than $\lambda/400$. The corresponding η_u are 16.7, 14.3, and 16.7 for the first, second, and third slits, and η_s are 4.82, 4.51, and 4.82, respectively. In general, the values of η_u and η_s are complex functions of the geometry. For SA-3, greater values of η_u and η_s are found for the narrower slits. Notice that only Al is considered to illustrate the concept because of available optical constants; however, in applications, Al can be replaced by Au or Pt with similar effects in the infrared to avoid oxidations.

In practical applications, a dielectric substrate may be used to support the Al gratings. For simplicity, the structure of Al grating coated on a silicon substrate is considered. At $\lambda = 10.64$ μm, optical constants of Si are given by $n = 3.42$ and

$\kappa = 1.09 \times 10^{-4}$ (Palik, 1985), such that Si can be thought as a dielectric by neglecting κ. Figure 6.12 shows the transmittance of Al grating on Si substrate assuming it to be semi-infinite, when the radiation is incident from vacuum (SA-4). In the calculation, the geometric parameters of Al grating are set to be the same as those of SA-1. Since the localization of energy density is a near-field phenomenon that involves evanescent waves, the assumption of the semi-infinite substrate is valid as long as the thickness is sufficiently large. Furthermore, if the top and bottom surfaces of the substrate are not parallel (i.e., wedged surfaces), then the interference effects due to multiple reflections inside the substrate can be neglected. Comparing Figs 6.9b and 6.12, the presence of Si substrate does not change much the far-field transmission characteristics of the Al slit array, except slightly lower transmittance values. Furthermore, similar to those of the free-standing Al slit array, the EMT results also show reasonable agreements with RCWA even though there exits a substrate.

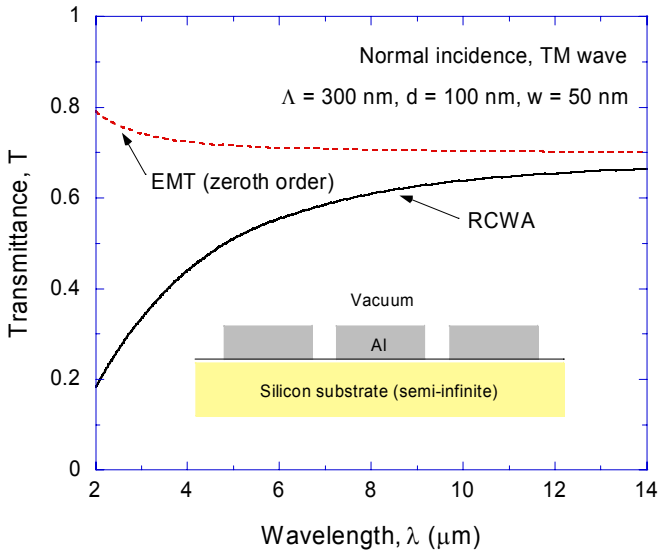

Figure 6.12 The spectral transmittance for the structure of Al grating mounted on a silicon substrate at normal incidence for the TM wave based on RCWA and EMT.

Figure 6.13a shows the normalized energy density of SA-4 over one grating period, where the slit region is from $x = 125$ nm to 175 nm. Unlike SA-1 that is a free-standing slit array, the media below and above SA-4 are different from each other. Since the localization of energy density in the exit medium is the key to fabricate nanoscale patterns, the energy density is normalized to that of the far-field transmitted radiation rather than that of incident radiation. Here, the far-field energy density is calculated at 100 μm away from the exit plane of the Al grating in Si. That is, the normalized energy density is differently defined from previous ones. In the figure, the shaded area represents the lateral region corresponding to the vacuum gap of slit array at various distances apart from the exit plane. At 5 nm away from the exit plane, the calculated energy density shows two high peaks with values close to 20 near x = 125 and 175 nm. On the other hand, the center of the slit has relatively low energy density, which is about 10. As the distance increases, the two peaks gradually disappear and the energy density distribution shows a plateau in the lateral region, whose size corresponds to the vacuum gap. At the distance of 50 nm, the maximum energy density is approximately 2 at the lateral position of the slit center line. When the distance is more than 300 nm, the energy density is not localized but the same everywhere, suggesting that field distribution beyond 300 nm is just like that of the far-field transmitted radiation. The values of η_u and η_s of SA-4 at the exit plane are also listed in Table 6.1. The definition of η_s is the same as the previous one. The η_s value of 3.76 based on the Poynting vector distribution implies that approximately 97.3% of transmitted energy is through the slit region. Note that this value is less than that of other cases mainly due to the lower transmittance of SA-4 with the Si substrate.

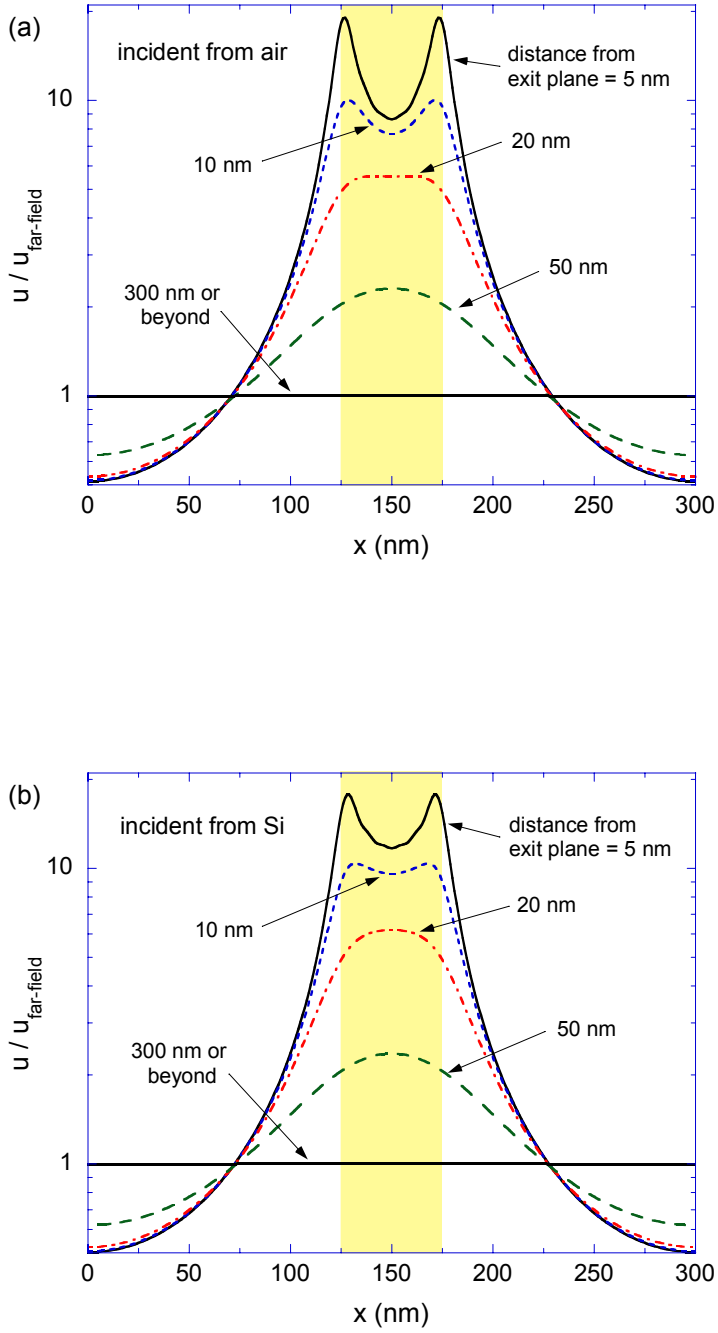

Figure 6.13 The normalized energy density distribution of the Al grating on Si structure over one grating period at various distances from the exit plane of the slit array: (a) when the radiation is incident from vacuum (SA-4); (b) when the radiation is incident from silicon (SA-5).

SA-5 represents the case when the radiation is incident from semi-infinite Si instead of a vacuum while the geometric parameters of grating are the same as those of SA-4. Subsequently, the far-field transmittance of SA-5 should be the same as that of SA-4. On the other hand, the near-field localization effects may be different because a vacuum is the medium after the exit plane. Figure 6.13b shows the normalized energy density distribution of SA-5 over one grating period at various distances from the exit plane. Again, the energy density is normalized to that of the far-field transmitted radiation. The normalized energy density of SA-5 shows very similar trend to that of SA-4, except at very short distance from the exit plane. When the distance is 5 nm, for instance, the energy density at the center of the shaded region for SA-5 is higher than that for SA-4, while peak values are very similar to each other. Consequently, SA-5 results in higher η_u value at the exit plane. Similar to SA-4, the localization of energy density becomes negligible if the distance from the exit plane is larger than 300 nm. In addition, the calculated η_s value is 3.86, which means that almost 99.9% of the incident energy is transmitted through vacuum gaps. Notice that more than 97% of the incident energy is funneled through the slit region for all structures considered in this section. This suggests that the near-field localization effects may not be strongly affected by the geometry of the grating as well as the medium after the exit plane. For applications, the grating structures considered here can be fabricated on a double-side polished silicon wafer. A Si_3N_4 thin film can be coated on the Si substrate as an anti-reflection coating.

6.3. Sample Fabrication and Transmission Measurement

In this section, three types of 1D metallic slits are fabricated on top of double-side-polished silicon wafer e-beam lithography. Figure 6.14 shows the four main steps of

the fabrication process and the thickness of each material. At the first step, 0.5 μm thick electron beam resist is coated on top of a 400 μm thick lightly doped silicon substrate and exposed to the electron beam. Silicon is selected as the substrate material for supporting metallic strips because it is semi-transparent in the infrared region. A JEOL JBX-9300FS e-beam lithography system is employed for fabrication due to its high resolution, pattern generation flexibility and repeatability, and acceptable time for pattern generation. Note that small quantity but different types of submicron sample are necessary for the current work such that an e-beam lithography system is a good choice. For mass production of similar structures as wire grid polarizers; however, extreme ultraviolet (EUV) or x-ray lithography as well as nanoimprinting can be more efficient. At the second step, the exposed resist is developed and the designed patterns are successfully transferred. Though the cross-sectional feature size of the resist strips is submicron scale, the strips are 4 mm in length and thousands of strips are equally spaced. Thus, the area of each sample is 4×4 mm, which is large enough for measurement later. 10 mm margin is left at the each side boundary such that each diced piece with sample is 24×24 mm. In other words, the sample is in the middle of 24×24 mm square silicon piece.

Next, 0.01 μm titanium and 0.1 μm gold are e-beam evaporated on top of the patterned substrate without breaking the vacuum of the e-beam metal evaporator (CVC SC 5000). A quartz crystal microbalance monitor displayed the thickness such that the deposition thickness is within a relative uncertainty of 10% (Lee *et al.*, 2006). The thin titanium plays the role as an adhesive layer between gold and silicon. Gold film of 0.1 μm thickness is considered as an optically thick due to the small penetration depth, which is mostly less than 20 nm in the spectral range. Since the patterned wafer is holding

vertically upside down during the evaporation, little amount of metal attaches on the side walls of the resist pattern and is easy for lift-off process. The lift-off process, which is the last step, is to remove the unwanted metal coatings by stripping the resist below them but still keep the designed metal strips. The lateral size of finished metallic slits is characterized by metal strip width (l), slit width (w), and the period ($\Lambda = l + w$). The metal filling ratio ($f = l / \Lambda$) is critical and the only geometric parameter when effective medium behavior is employed for modeling (Lee *et al.*, 2007b). In order to tell such dimensions of the fabricated samples, we take their images from a scanning electron microscopy (SEM). Table 6.2 lists the values of those dimensions as well as the metal filling ratio of each sample.

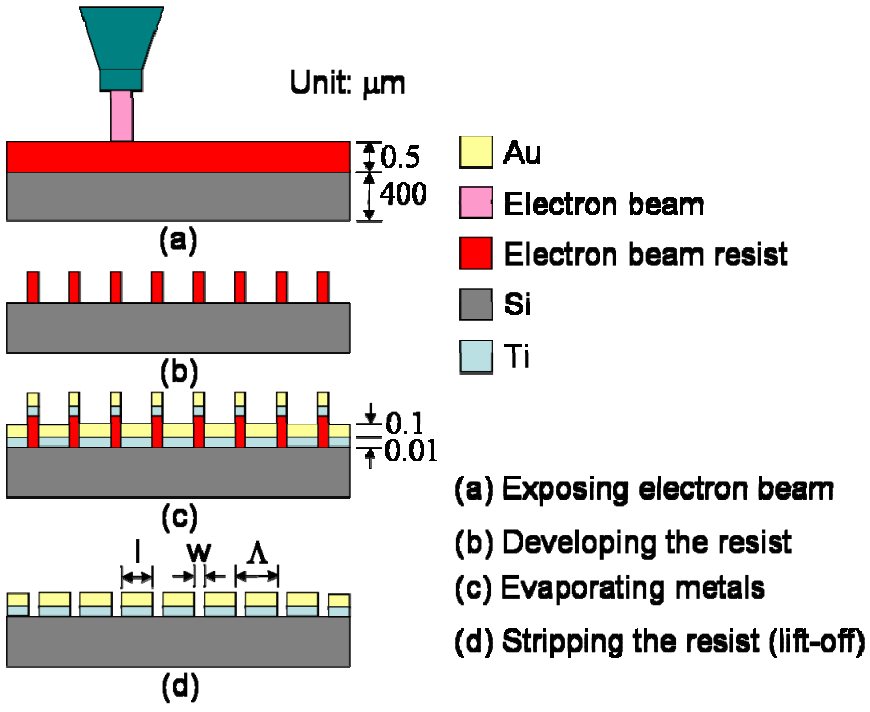

Figure 6.14 Fabrication of periodic nanoscale slit arrays. (a) exposing electron beam; (b) developing the resist; (c) evaporating metals; (d) stripping the resist.

Table 6.2 Lateral dimension of submicron metallic slit arrays

Sample No.	Λ (nm)	l (nm)	w (nm)	f
1	800	506	294	0.63
2	800	514	286	0.64
3	1000	717	283	0.72

Figures 6.15a and 6.15b show the SEM images from top view of sample No. 2 and 3, respectively. Though it takes several hours to fabricate each sample and the patterns in a field (500×500 μm) is duplicated step by step, the whole area of each sample is very uniform. As a result, the period of the metal strips is believed to be the same as the designed values (800 and 1000 nm), which also agree with those measured from the scale. However, the strip and slit width deviate from the designed values due to the lift-off process and e-beam dose profile. Figure 6.15b shows the SEM image of sample 3 in an oblique angle to see the side and edges of several metal strips on top of silicon. It is clear that a thin titanium adhesive layer is between the gold strips and the substrate. The top profile of the gold strip is pretty flat, except the edges show some gold residue after the lift-off process. Very little warp at the end of each metal strip is also shown in the figure. Since only middle part of each sample is going to be measured and modeled, the approximation of rectangular solid for metal strips should be valid. Note that the thickness of the films is assumed to be the same as the designed value.

The ABB Bomen FTLA 2000 series (MB154S) FT-IR spectrometer (Lee *et al.*, 2005) with a highest resolution of 1 cm^{-1} is used to measure the normal transmittance (T) as shown in Fig. 6.15. The spectrometer equips a globar source and a pyroelectric detector to measure the transmittance spectrum in the wave number range from 500 to 5000 cm^{-1} ($2 < \lambda < 20$ μm). A sample holder with a tailored 3×3 mm square aperture

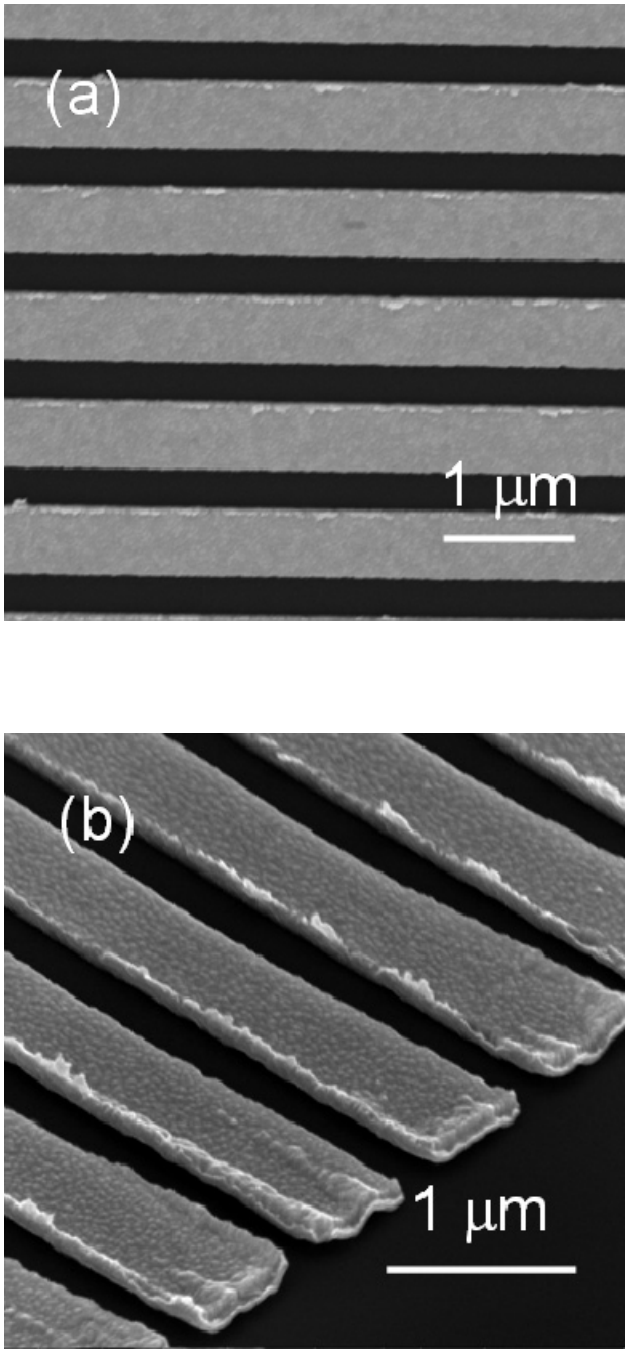

Figure 6.15 SEM images of: (a) Sample No.2; (b) Sample No. 3.

limits the incidence size smaller than sample area. Though the aperture is smaller than the beam size, the transmitted light is still strong enough to be sensed. The sample is clamped against the aperture perpendicularly to the incident beam. The apodization function and the phase correction are both cosine truncation function. For all measurements, an average of 800 scans is used to reduce the noise level. The uncertainty is estimated to be 0.01 in the measurements, which may be a problem if the transmittance is close to zero. In order to purify the polarization of the light, two wire-grid linear polarizers with zinc selenide (ZnSe) substrate are employed. One is positioned in front of the aperture as a pre-polarizer while the other one is behind the sample as a post-polarizer as the top view of experiment set-up shown in Fig. 6.16. The two polarizers are intentionally not parallel aligned with each other as well as the aperture to eliminate multiple reflections among them. Each polarizer shows high polarization-dependant transmission in the infrared region. For example, the extinction ratio (ER) defined by the maximum transmission divided by the minimum transmission is 100 and 300 at $\lambda = 3$ μm and $\lambda = 10$ μm,

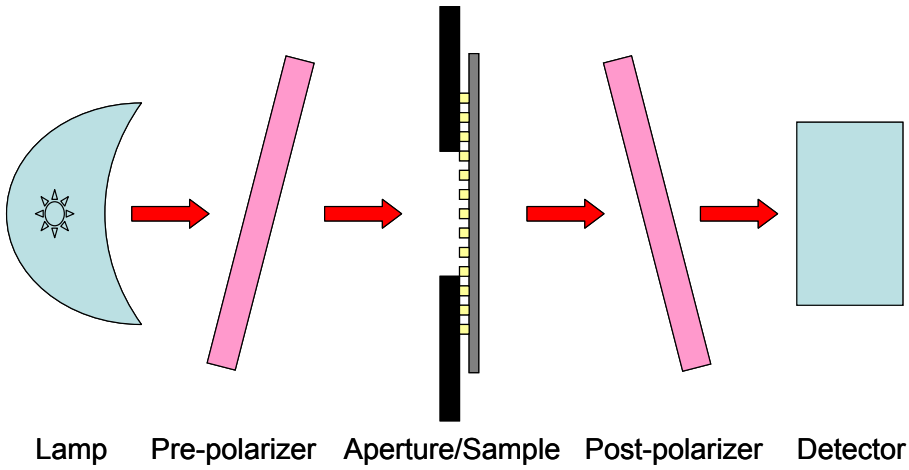

Figure 6.16 Set-up of normal transmission measurement for nanoscale slit arrays.

respectively. The minimum transmission is between 0.002 to 0.004 at $\lambda \geq 5$ μm. Note that the insertion of the polarizers leaves much space that cannot be N_2 purged. Hence, the participation of H_2O, CO_2, and other gases absorption is unavoidable.

The normal transmittance of a 400 μm thick double-side polished and lightly-doped silicon substrate is measured to verify the applicability of the experiment set-up,. Figure 6.17 shows the measured transmittance with different number of polarizers as well as that of numerical modeling results in the spectral range from 2 to 15 μm. The four curves show excellent agreement in the spectral range. It is also clear that the addition of the aperture and tilting polarizers do not affect the measurement results. However, some noises existing in the spectrum come from the absorption of gases. The noises around 2.5 μm comes from the absorption of both CO_2 and H_2O, while the noise at $\lambda = 4.3$ μm and

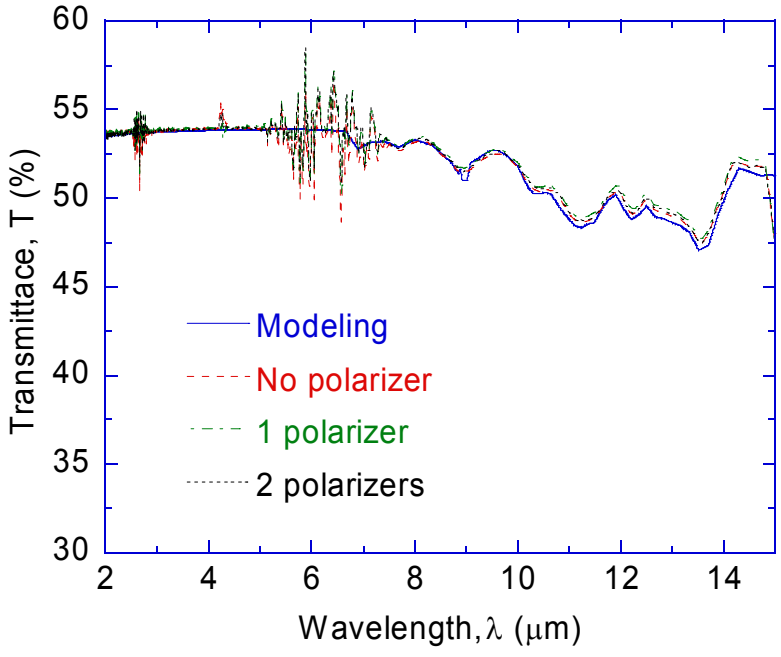

Figure 6.17 Normal transmittance of plain 400-μm-thick silicon substrate.

$\lambda = 6.3$ μm results from the absorption of CO_2 and H_2O, respectively. Note that the spectral averaging of transmittance is applied when calculating the modeling transmittance (Lee *et al.*, 2005). The transmittance value is mostly above 0.47 in the whole spectrum because silicon is semi-transparent and serves well as the supporting substrate of metallic slit arrays.

Figure 6.18 shows the measured normal transmittance as well as modeling results of three samples for different polarized incidence wave. Since the optical constants of Au and Ti in Ref. (Palik, 1998) are only available up to 10 μm, optical constants based on the Drude model (Ordal *et al.*, 1983) are employed and extended for modeling the whole spectral range. Figures 6.18a and 6.18b shows the TE and TM wave transmittance of sample No. 1, respectively. For the TE wave transmittance, both numerical modeling results match well with experiment results although the Drude model shows a little more under prediction. The TE wave transmittance monotonically decreases towards the long wavelength and is less than 0.01 when $\lambda > 4$ μm. Furthermore, the measured transmittance shows negative value when $\lambda > 13$ μm due to very little transmittance and the finite Fourier terms during FT-IR transform. Such low transmittance can be qualitatively explained by the effective medium behavior. In fact, the TE wave transmittance based on the effective medium is less than 10^{-3} along the whole spectrum and is not shown in the plots. For TM waves, the measured transmittance still shows good agreement with numerical modeling, except noises. The noises resulting from the absorption of CO_2 and H_2O still can be found in the measurement results similar to those of plain silicon. The deviation at $\lambda = 9.4$ and 10.4 μm is result of CO_2 absorption. The drop of measured transmittance at $\lambda > 8$ μm may come from the silicon absorption. The

dip $\lambda = 2.81\ \mu m$ is due to the Wood's anomaly (Kim, 2005), which can be predicted by the grating equation. Though Wood's anomaly usually comes from one diffraction order at the grazing angle in the first medium, the tip of TM wave is caused by the diffraction showing at the silicon substrate. That is, the first order diffraction shows up at the grazing angle of silicon substrate with its refractive index close to 3.44 at $\lambda = 2.81\ \mu m$. The transmittance for the TM wave based on the effective medium behavior is close to 0.55 along the spectrum (not shown here) and provides qualitative explanation for high transmission as well.

Figures 6.18c and 6.18d show the normal transmittance of sample No. 2 for the TE wave and TM wave, respectively. Since the sample structure is very close to that of sample No. 1, the transmittance spectrum is also very similar. Specifically, the dip in the TM wave transmittance spectrum is the same wavelength because the periods of metallic slits are identical. However, the transmittance value is a little lower than that of sample No. 1 due to the higher metal filling ratio. In this case, the Drude model gives better agreement with experimental data. Note that titanium is only 10 nm under the 100 nm thick Au gratings as an adhesive layer. Hence, the transmittance spectrum is also modeled without the Ti layer and it shows little difference. On the other hand, Figures 6.18e and 6.18f show the normal transmittance of sample No. 3 for TE and TM waves, respectively. Since the filling ratio is higher than other two samples, the transmittance is lower than that of other samples, especially for the TM wave. In addition, the increment of the slit period shifts the dip of the TM wave transmittance while its wavelength can still be predicted by the grating equation. Generally speaking, optical constants from Palik's handbook give better approximation for the TE wave transmittance and both

numerical models show a good agreement for the TM wave. In short, the measured nanoscale metallic slit array transmittance match RCWA modeling very well for both the TE and TM wave. Such confirmation will facilitate the promising application of using nanoscale slit arrays in nanolithography applications.

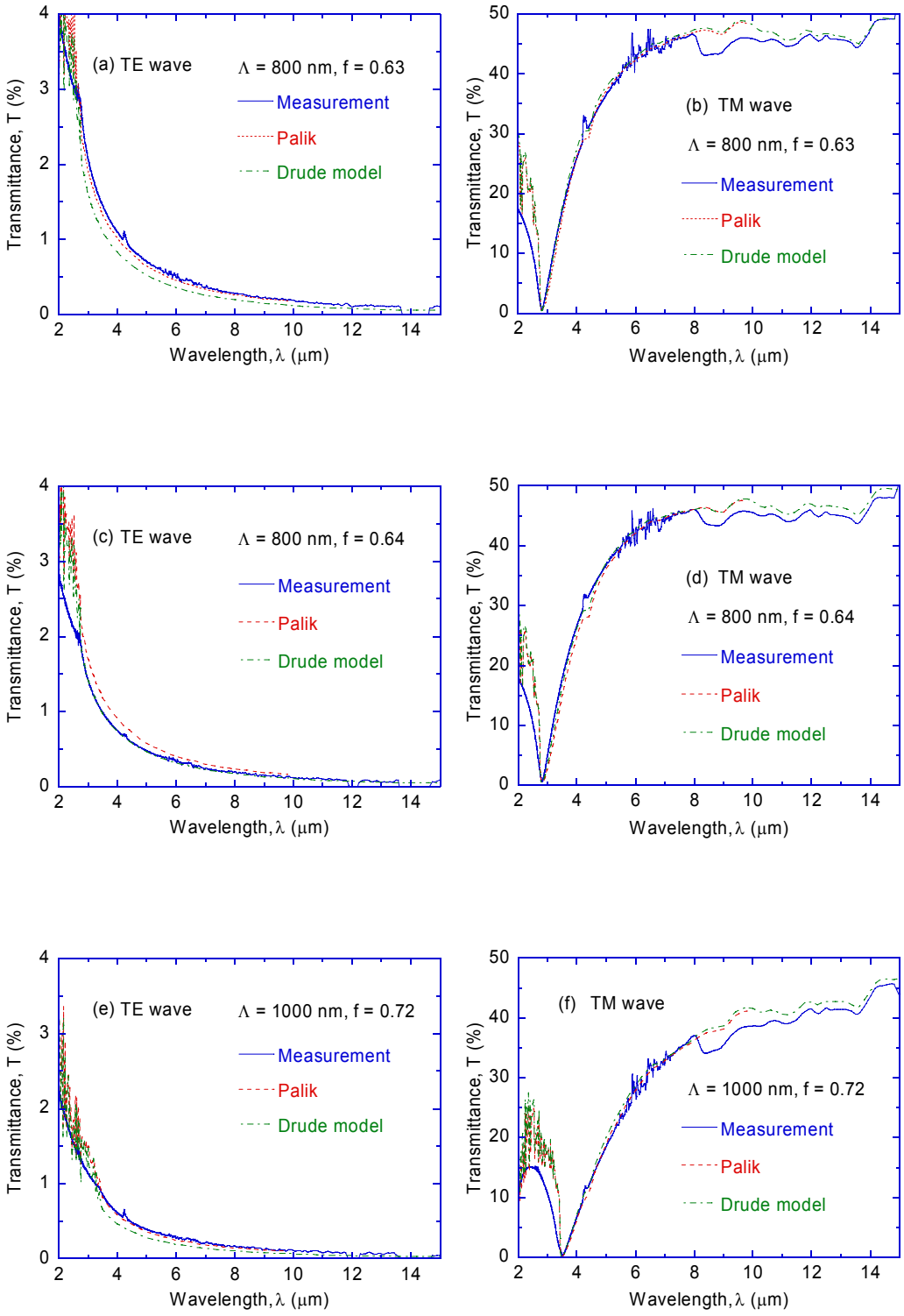

Figure 6.18 Normal transmittance of nanoscale metallic slit arrays: (a) TE waves and (b) TM waves for sample No. 1; (c) TE waves and (d) TM waves for sample No. 2; (e) TE waves and (f) TM waves for sample No. 3.

CHAPTER 7

SUMMARY CONCLUSIONS AND RECOMMENDATIONS

This dissertation clearly demonstrates that precise control and tuning of the radiative properties using micro/nanofabrication are not only feasible but also have numerous technological impacts. Based on the solid foundations, the representative applications of periodic micro/nanostructures in electronics, energy conversion, and nanotechnology are detailed investigated both theoretically and experimentally. An efficient and rigorous numerical algorithm, rigorous coupled-wave analysis (RCWA), is employed as the theoretical foundation for both far-field radiative property and near-field electromagnetic (EM) field modeling. Modifications for RCWA fast convergence in conical diffraction efficiency calculations are demonstrated. The measured diffraction efficiencies of both one- and two-dimensional (1 and 2D) silicon microstructured surfaces illustrate the strong dependence between structure profiles and their radiative properties. The three potential applications in modern technologies are thermal control in rapid thermal processing, thermophotovoltaic radiator design, and nanolithography.

For the first application, this dissertation presents numerical predictions of the absorptance of selected nanoscale patterns that may be found in the device structures in advanced CMOS technology. The effects of temperature, wavelength, polarization, and angle of incidence are systematically studied. Comparison is made to different patterning structures to examine the effect of nanostructures on the radiative properties. In the cases studied, for wavelengths between 200 nm to 1000 nm, temperature does not affect the absorptance significantly when comparing absorptance at temperatures of 25°C, 700°C,

and 910°C. Periodic patterns, including arrays of gates and trenches, lead to diffractions and, hence, affect the absorptance in a complex manner. Different polarizations of the incident radiation lead to different responses from lateral periodic structures. It is particularly notable that the gates affect the absorptance for the TE wave significantly but the trenches affect the absorptance for the TM wave significantly. For the generic CMOS structure composed of gates and trenches, its absorptance spectra exhibit common features shown in those of only gates or trenches. The total absorptance averaged over two polarizations for CMOS is 0.2 greater than that of plain Si. On the other hand, the average total absorptance for only gates or trenches on top of Si substrate is about 0.1 greater than that of plain Si. Although gates on a SiO_2 film and Si substrate is not the most complicated structures, the coupling of diffraction and thin-film effects result in very complicated features in the absorptance spectra and angular distributions. Interestingly, Wood's anomalies introduce abrupt changes in absorptance at short wavelengths and can be predicted by the well-known grating equation. Three effective medium formulations are compared with the RCWA to evaluate their applicability to predict the absorptance for the studied nanostructures. Although in some cases approximation formulations may be used to compute the average total absorptance, they cannot substitute the rigorous solutions for the spectral and polarized radiative properties.

The second application is to actively design a wavelength-selective emitter for energy conversion enhancement. A 1D tungsten complex grating is presented for application of TPV radiators working at wavelengths between 0.8 and 1.7 μm. The complex grating has four pairs of rectangular ridge and groove and is a superposition of two simple gratings. The short-period simple grating provides flat dispersion curve, and

the long-period simple grating provides band-folding and multiple intersections with light lines. Consequently, SPP can be excited to enhance emittance for TM waves with plane of incidence perpendicular to the grating grooves. The emittance of the complex grating shows a wide peak within the wavelength region of interest but low at long wavelengths. The complex grating with different ridge heights is also studied for fabrication flexibility.

For the third application in nanothermal manufacturing, the dissertation initiates an examination of transmission enhancement in the spectral region from visible to mid-infrared through nanoscale 1D slit arrays based on both the far-field spectral transmittance and the field distributions near the grating region. The mechanisms enabling large transmission are Wood's anomaly, cavity resonance, and the effective medium behavior, depending on the spectral region. Near the wavelength corresponding to Wood's anomaly, the field distribution in the vicinity of the grating can be strongly affected by the interference of diffracted evanescent waves and propagating waves. Hence, Wood's anomaly can also suppress the transmittance, along with the excitation of SPPs. The resonance wavelengths depend strongly on the polarization and can also be affected by the thickness, period, and the slit width of gratings. In the mid-IR spectral region, however, the effective medium theory can explain the large transmission found in a wavelength-insensitive manner for TM waves, as well as the nearly-zero transmittance for TE waves. Three submicron 1D metallic gratings on top a Si substrate are fabricated and their measured spectral transmittance spectra firmly support the effective medium behavior and largely match RCWA modeling results. Next, the enhanced TM wave transmission enhancement and strong field localization can be achieved from nanoscale Al slit arrays for MIR radiation. The calculated energy density and Poynting vector

distributions reveal that the EM fields are localized in the near field around the slit exit and inlet. The calculation suggests that infrared radiation could be confined, at least in one dimension, to a length scale as small as $\lambda/400$, with a factor of 16.7 increase in the local energy density and a factor of 4.82 increase of the energy flux compared to those of the incident wave.

In the future, this research may be extended into several aspects with strong impacts. Since RCWA is an efficient tool in obtaining diffraction efficiency from periodic structures, it is of great value to commercialize RCWA software with the capability in modeling diffraction efficiency pattern by simply inputting structure profile and optical constants. For example, 2D and 3D structure modeling capabilities are beneficial to photonic crystal study. The combination structure of thin films and gratings are attractive to waveguide and laser applications. In addition, the software may be able to inversely fit simple 1D surface profiles with known optical constants and diffraction efficiency. Such function is very useful for non-contact inspection, especially for nanoscale devices.

With the knowledge to the first application in the dissertation, the future study can contain locally absorbed energy distribution, which may then be coupled with a heat conduction model to examine the effect of temperature nonuniformity on the dynamic stress field. On the other hand, the heating radiation is random polarized light and comes from all directions to the patterned wafer such that it takes very long for integration even at single wavelength. As a result, one approximation method with reasonable accuracy is still desired. The extension of this study can be the region map generation for different approximation methods such that people can choose suitable approximation methods.

Consequently, one may come out a better approximation model for periodic dielectric or metallic structure at wavelengths comparable to structure feature size as the next step.

For the second application, the experimental demonstration of such wavelength-selective TPV radiator at high temperature is a challenging but meaningful work. The challenges lie in two parts, sample fabrication and experimental set-up. The tungsten substrate is hard to etch, especially for 1D periodic nanoscale long lines. Instead, if the tungsten film is sputtered and the structure is generated by lift-off, the optical constants of deposited film may be different from that of the bulk material. The measurement set-up will be complicated even at room temperature. An integrating sphere is necessary for hemispherical property measurement and a monochromator can be employed for wavelength selection. Several focusing lens and mirrors are expected for light path built-up. Of course, the high temperature involvement should further consider the thermal stability of the set-up and temperature control of the sample heating.

Last but not least, the success of the third application, nanolithography, should be fulfilled by selecting appropriate material for mid-infrared thermal curing to generate nanostructures. Nanothermal manufacturing is not like traditional photolithography, which employs chemicals reactive only at wavelengths in visible or ultraviolet. Thermal radiation exists everywhere such that a sensitive chemical cannot function well. Therefore, the knowledge to material science is critical for the next step of nanoscale pattern generation. In addition, the heat can be transferred through conduction after radiation absorption. Another interesting study could be the investigation on the pattern shift from the initial design due to heat conduction.

REFERENCES

Abdo, A., Nellis, G., Wei, A., El-Morsi, M., Engelstad, R., Brueck, S.R.J., and Neumann, A., 2004, "Optimizing the Fluid Dispensing Process for Immersion Lithography," *Journal of Vacuum Science & Technology B*, Vol. 22, pp. 3454-3458.

Auslender, M., Hava, S., 1995, "Zero Infrared Reflectance Anomaly in Doped Silicon Lamellar Gratings. I. From Antireflection to Total Absorption," *Infrared Physics & Technology*, Vol. 36, pp., pp. 1077-1088.

Azad, A.K., Zhao, Y., and Zhang, W., 2005, "Transmission Properties of Terahertz Pulses through an Ultrathin Subwavelength Silicon Hole Array," *Applied Physics Letters*, Vol. 86, 141102.

Basu, S., Chen, Y.-B., and Zhang, Z.M., 2007, "Microscale Radiation in Thermophotovoltaic Devices - A Review," *International Journal of Energy Research* (accepted).

Bentini, G.G., and Correra, L., 1983, "Analysis of Thermal Stresses Induced in Silicon During Xenon Arc Lamp Flash Annealing," *Journal of Applied Physics*, Vol. 54, pp. 2057-2062.

Bett, A.W., and Sulima, O.V., 2003, "Gasb Photovoltaic Cells for Applications in TPV Generators," *Semiconductor Science and Technology*, Vol. 18, pp. S184-S190.

Bird, G.R., and Parrish, M., 1960, "The Wire Grid as a Near-Infrared Polarizer," *Journal of the Optical Society of America*, Vol. 50, pp. 886-891.

Born, M., and Wolf, E., 1999, *Principles of Optics*, Cambridge, UK.

Boueke, A., Kühn, R., Fath, P., Willeke, G., and Bucher, E., 2001, "Latest Results on Semitransparent POWER Silicon Solar Cells," *Solar Energy Materials and Solar Cells*, Vol. 65, pp. 549-553.

Bruggeman, D.A.G., 1935, "Calculation of Various Physics Constants in Heterogenous Substances I. Dielectricity Constants and Conductivity of Mixed Bodies from Isotropic Substances," *Annalen Der Physik*, Vol. 24, pp. 636-664.

Carminati, R., and Greffet, J.-J., 1999, "Near-Field Effects in Spatial Coherence of Thermal Sources," *Physical Review Letters*, Vol. 82, pp. 1660-1663.

Celanovic, I., O'Sullivan, F., Ilak, M., Kassakian, J., and Perreault, D., 2004, "Design and Optimization of One-Dimensional Photonic Crystals for Thermophotovoltaic Applications," *Optics Letters*, Vol. 29, pp. 863-865.

Chen, Y.B., Zhu, Q.Z., Wright, T.L., King, W.P., and Zhang, Z.M., 2004, "Bidirectional Reflection Measurements of Periodically Microstructured Silicon Surfaces," *International Journal of Thermophysics*, Vol. 25, pp. 1235-1252.

Chen, Y.-B., and Zhang, Z.M., 2007, "Design of Tungsten Complex Gratings for Thermophotovoltaic Radiators," *Optics Communications*, Vol. 269, pp. 411-417.

Chen, Y.-B., Zhang, Z.M., and Timans, P.J., 2007, "Radiative Properties of Patterned Wafers with Nanoscale Linewidth," *Journal of Heat Transfer*, Vol. 129, pp. 79-89.

Cohn, D.W., Tang, K., and Buckius, R.O., 1997, "Comparison of Theory and Experiments for Reflection from Microcontoured Surfaces," *International Journal of Heat and Mass Transfer*, Vol. 40, pp. 3223-3235.

Coutts, T.J., 1999, "A Review of Progress in Thermophotovoltaic Generation of Electricity," *Renewable & Sustainable Energy Reviews*, Vol. 3, pp. 77-184.

Elston, S.J., Bryanbrown, G.P., and Sambles, J.R., 1991, "Polarization Conversion from Diffraction Gratings," *Physical Review B*, Vol. 44, pp. 6393-6400.

Erofeev, A.F., Kolpakov, A.V., Makhviladze, T.M., Martjushenko, A.V., Panjukhin, A.V., Volchek, O.S., and Orlowski, M., 1995, "Comprehensive RTP Modeling and Simulation," *Proc. 3rd International Rapid Thermal Processing Conference*, pp. 181-197.

Fahrenbruch, A.L., and Bube, R.H., 1983, *Fundamentals of Solar Cells: Photovoltaic Solar Energy Conversion*, Academic Press, New York.

Fourspring, P.M., DePoy, D.M., Rahmlow, T.D., Lazo-Wasem, J.E., and Gratrix, E.J., 2006, "Optical Coatings for Thermophotovoltaic Spectral Control," *Applied Optics*, Vol. 45, pp. 1356-1358.

Fraas, L.M., Avery, J.E., Huang, H.X., and Martinelli, R.U., 2003, "Thermophotovoltaic System Configurations and Spectral Control," *Semiconductor Science and Technology*, Vol. 18, pp. S165-S173.

Garnett, J.C.M., 1904, "Colours in Metal Glasses and in Metallic Films.," *Philosophical Transactions of the Royal Society of London Series A*, Vol. 203, pp. 385-420.

Gelpey, J.C., Elliott, K., Camm, D., McCoy, S., Ross, J., Downey, D.F., and Arevalo, E., 2002, "Advanced Annealing for Sub-130nm Junction Formation," *Rapid Thermal and Other Short-Time Processing Technologies III,* P. J. Timans, E. Gusev, F. Roozeboom, M. C. Öztürk, and D.-L. Kwong, eds., The Electrochemical Society, Pennington, NJ, pp. 313-324.

Ghaemi, H.F., Thio, T., Grupp, D.E., Ebbesen, T.W., and Lezec, H.J., 1998, "Surface Plasmons Enhance Optical Transmission through Subwavelength Holes," *Physical Review B*, Vol. 58, pp. 6779-6782.

Glytsis, E.N., and Gaylord, T.K., 1992, "High-Spatial-Frequency Binary and Multilevel Stairstep Gratings: Polarization-Selective Mirrors and Broad-Band Antireflection Surfaces," *Applied Optics*, Vol. 31, pp. 4459-4470.

Granqvist, C.G., and Hunderi, O., 1977, "Optical-Properties of Ultrafine Gold Particles," *Physical Review B*, Vol. 16, pp. 3513-3534.

Green, M.A., 1982, *Solar Cells: Operating Principles, Technology, and System Applications*, Englewood Cliffs, N.J.

Greffet, J.-J., Carminati, R., Joulain, K., Mulet, J.P., Mainguy, S., and Chen, Y., 2002, "Coherent Emission of Light by Thermal Sources," *Nature*, Vol. 416, pp. 61-64.

Groves, T.R., Pickard, D., Rafferty, B., Crosland, N., Adam, D., and Schubert, G., 2002, "Maskless Electron Beam Lithography: Prospects, Progress, and Challenges," *Microelectronic Engineering*, Vol. 61-62, pp. 285-293.

Guo, L.J., 2004, "Recent Progress in Nanoimprint Technology and Its Applications," *Journal of Physics D*, Vol. 37, pp. R123-R141.

Gwyn, C.W., Stulen, R., Sweeney, D., and Attwood, D., 1998, "Extreme Ultraviolet Lithography," *Journal of Vacuum Science & Technology B*, Vol. 16, pp. 3142-3149.

Han, S.T., Tsao, Y.-L., Walser, R.M., and Becker, M.F., 1992, "Electromagnetic Scattering of Two-Dimensional Surface-Relief Dielectric Gratings," *Applied Optics*, Vol. 31, pp. 2343-2352.

Hebb, J.P., and Jensen, K.F., 1998, "The Effect of Patterns on Thermal Stress During Rapid Thermal Processing of Silicon Wafers," *IEEE Transactions on Semiconductor Manufacturing*, Vol. 11, pp. 99-107.

Heinzel, A., Boerner, V., Gombert, A., Bläsi, B., Wittwer, V., and Luther, J., 2000, "Radiation Filters and Emitters for the NIR Based on Periodically Structured Metal Surfaces," *Journal of Modern Optics*, Vol. 47, pp. 2399-2419.

Hesketh, P.J., Gebhart, B., and Zemel, J.N., 1988, "Measurements of the Spectral and Directional Emission from Microgrooved Silicon Surfaces," *Journal of Heat Transfer*, Vol. 110, pp. 680-686.

Hesketh, P.J., Zemel, J.N., and Gebhart, B., 1986, "Organ Pipe Radiant Modes of Periodic Micromachined Silicon Surfaces," *Nature*, Vol. 324, pp. 549-551.

Hessel, A., and Oliner, A.A., 1965, "A New Theory of Woods Anomalies on Optical Gratings," *Applied Optics*, Vol. 4, pp. 1275-1297.

Jellison, G.E., Jr., and Modine, F.A., 1983, "Optical Functions of Silicon between 1.7 and 4.7 ev at Elevated Temperatures," *Physical Review B*, Vol. 27, pp. 7466-7472.

Jellison, G.E., Jr., and Modine, F.A., 1994, "Optical Functions of Silicon at Elevated Temperatures," *Journal of Applied Physics*, Vol. 76, pp. 3758-3761.

Kim, D., 2005, "Polarization Characteristics of a Wire-Grid Polarizer in a Rotating Platform," *Applied Optics*, Vol. 44, pp. 1366-1371.

Kreiter, M., Oster, J., Sambles, R., Herminghaus, S., Mittler-Neher, S., and Knoll, W., 1999, "Thermally Induced Emission of Light from a Metallic Diffraction Grating, Mediated by Surface Plasmons," *Optics Communications*, Vol. 168, pp. 117-122.

Kristensen, R.T., Beausang, J.F., and DePoy, D.M., 2004, "Frequency Selective Surfaces as Near-Infrared Electromagnetic Filters for Thermophotovoltaic Spectral Control," *Journal of Applied Physics*, Vol. 95, pp. 4845-4851.

Laks, B., Mills, D.L., and Maradudin, A.A., 1981, "Surface-Polaritons on Large-Amplitude Gratings," *Physical Review B*, Vol. 23, pp. 4965-4976.

Lalanne, P., and Lemercier-Lalanne, D., 1996, "On the Effective Medium Theory of Subwavelength Periodic Structures," *Journal of Modern Optics*, Vol. 43, pp. 2063-2085.

Lalanne, P., and Morris, G.M., 1996, "Highly Improved Convergence of the Coupled-Wave Method for TM Polarization," *Journal of the Optical Society of America A*, Vol. 13, pp. 779-784.

Laroche, M., Arnold, C., Marquier, E., Carminati, R., Greffet, J.-J., Collin, S., Bardou, N., and Pelouard, J.-L., 2005, "Highly Directional Radiation Generated by a Tungsten Thermal Source," *Optics Letters*, Vol. 30, pp. 2623-2625.

Laroche, M., Carminati, R., and Greffet, J.-J., 2005, "Resonant Optical Transmission through a Photonic Crystal in the Forbidden Gap," *Physical Review B*, Vol. 71, pp. 155113.

Lee, B.J., Chen, Y.-B., and Zhang, Z.M., 2007a, "Transmission Enhancement through Nanoscale Metallic Slit Arrays from the Visible to Mid-Infrared," *Journal of Computational and Theoretical Nanoscience*, (accepted).

Lee, B.J., Chen, Y.-B., and Zhang, Z.M., 2007b, "Confinement of Infrared Radiation to Nanometer Scales through Metallic Slit Arrays," *Journal of Quantitative Spectroscopy and Radiative Transfer*, (submitted).

Lee, B.J., Zhang, Z.M., Early, E.A., DeWitt, D.P., and Tsai, B.K., 2005, "Modeling Radiative Properties of Silicon with Coatings and Comparison with Reflectance Measurements," *Journal of Thermophysics and Heat Transfer*, Vol. 19, pp. 558-565.

Lee, H.J., Chen, Y.B., and Zhang, Z.M., 2006, "Directional Radiative Properties of Anisotropic Rough Silicon and Gold Surfaces," *International Journal of Heat and Mass Transfer*, Vol. 49, pp. 4482-4495.

LeGall, J., Olivier, M., and Greffet, J.-J., 1997, "Experimental and Theoretical Study of Reflection and Coherent Thermal Emission by a SiC Grating Supporting a Surface-Phonon Polariton," *Physical Review B*, Vol. 55, pp. 10105-10114.

Lezec, H.J., and Thio, T., 2004, "Diffracted Evanescent Wave Model for Enhanced and Suppressed Optical Transmission through Subwavelength Hole Arrays," *Optics Express*, Vol. 12, pp. 3629-3651.

Li, L., 1996, "Use of Fourier Series in the Analysis of Discontinuous Periodic Structures," *Journal of the Optical Society of America A*, Vol. 13, pp. 1870-1876.

Lindsay, R., Pawlak, B.J., Henson, K., Satta, A., Severi, S., Lauwers, A., Surdeanu, R., McCoy, S., Gelpey, J., Pages, X., and Maex, K., 2004, "Integration of Low and High Temperature Junction Anneals for 45nm CMOS," *Advanced Short-Time Thermal Processing for Si-Based CMOS Devices II,* M. C. Öztürk, E. P. Gusev, L. J. Chen, D.-L. Kwong, P. J. Timans, G. Miner and F. Roozeboom, eds., The Electrochemical Society, Pennington, NJ, pp. 145-156.

Lin, S.Y., Moreno, J., and Fleming, J.G., 2003, "Three-Dimensional Photonic-Crystal Emitter for Thermal Photovoltaic Power Generation," *Applied Physics Letters*, Vol. 83, pp. 380-382.

Liu, J., Zhang, S.J., and Chen, Y.S., 2004, "Rigorous Electromagnetic Modeling of Radiative Interactions with Microstructures Using the Finite Volume Time-Domain Method," *International Journal of Thermophysics*, Vol. 25, pp. 1281-1297.

Luo, X., and Ishihara, T., 2004, "Surface Plasmon Resonant Interference Nanolithography Technique," *Applied Physics Letters*, Vol. 84, pp. 4780-4782.

Madou, M.J., 1997, *Fundamentals of Microfabrication*, Boca Raton, FL.

Malitson, I.H., 1965, "Interspecimen Comparison of the Refractive Index of Fused Silica," *Journal of the Optical society of America*, Vol. 55, pp. 1205-1209.

Marquier, F., Joulain, K., Mulet, J.P., Carminati, R., Greffet, J.-J., and Chen, Y., 2004, "Coherent Spontaneous Emission of Light by Thermal Sources," *Physical Review B*, Vol. 69, pp. 155412.

Marquier, F., Greffet, J.-J., Collin, S., Pardo, F., and Pelouard, J.L., 2005, "Resonant Transmission through a Metallic Film Due to Coupled Modes," *Optics Express*, Vol. 13, pp. 70-76.

Maruyama, S., Kashiwa, T., Yugami, H., and Esashi, M., 2001, "Thermal Radiation from Two-Dimensionally Confined Modes in Microcavities," *Applied Physics Letters*, Vol. 79, pp. 1393-1395.

Maxwell Garnett, J.C., 1904, "Colours in Metal Glasses and in Metallic Films," *Philosophical Transactions of the Royal Society of London A*, Vol. 203, pp. 385-420.

Messenger, R.A., and Ventre, J., 2004, *Photovoltaic Systems Engineering*, CRC Press, Boca Raton, FL.

Modest, M.F., 2003, *Radiative Heat Transfer*, Academic, San Diego, CA.

Moharam, M.G., Grann, E.B., Pommet, D.A., and Gaylord, T.K., 1995a, "Formulation for Stable and Efficient Implementation of the Rigorous Coupled-Wave Analysis of Binary Gratings," *Journal of the Optical Society of America A*, Vol. 12, pp. 1068-1076.

Moharam, M.G., Pommet, D.A., Grann, E.B., and Gaylord, T.K., 1995b, "Stable Implementation of the Rigorous Coupled-Wave Analysis for Surface-Relief Gratings - Enhanced Transmittance Matrix Approach," *Journal of the Optical Society of America A*, Vol. 12, pp. 1077-1086.

Nelson, R.E., 2003, "A Brief History of Thermophotovoltaic Development," *Semiconductor Science and Technology*, Vol. 18, pp. S141-S143.

Ordal, M.A., Long, L.L., Bell, R.J., Bell, S.E., Bell, R.R., Alexander, R.W., and Ward, C.A., 1983, "Optical Properties of the Metals Al, Co, Cu, Au, Fe, Pb, Ni, Pd, Pt, Ag, Ti, and W in the Infrared and Far Infrared," *Applied Optics*, Vol. 22, pp. 1099-1119.

O'Sullivan, F., Celanovic, I., Jovanovic, N., Kassakian, J., Akiyama, S., and Wada, K., 2005, "Optical Characteristics of One-Dimensional Si/SiO_2 Photonic Crystals for Thermophotovoltaic Applications," *Journal of Applied Physics*, Vol. 97, pp. 033529.

Palik, E.D., 1998, *Handbook of Optical Constants of Solids*, San Diego, CA.

Park, K., Lee, B.J., Fu, C., and Zhang, Z.M., 2005, "Study of the Surface and Bulk Polaritons with a Negative Index Metamaterial," *Journal of the Optical Society of America B*, Vol. 22, pp. 1016-1023.

Peng, S., and Morris, G.M., 1995, "Efficient Implementation of Rigorous Coupled-Wave Analysis for Surface-Relief Gratings," *Journal of the Optical Society of America A*, Vol. 12, pp. 1087-1096.

Petit, R., and Botten, L.C., 1980, *Electromagnetic Theory of Gratings*, Berlin, New York.

Piner, R.D., Zhu, J., Xu, F., Hong, S., and Mirkin, C.A., 1999, ""Dip-Pen" Nanolithography," *Science*, Vol. 283, pp. 661-663.

Porto, J.A., Garcia-Vidal, F.J., and Pendry, J.B., 1999, "Transmission Resonances on Metallic Gratings with Very Narrow Slits," *Physical Review Letters*, Vol. 83, pp. 2845-2848.

Pralle, M.U., Moelders, N., McNeal, M.P., Puscasu, I., Greenwald, A.C., Daly, J.T., Johnson, E.A., George, T., Choi, D.S., El-Kady, I., and Biswas, R., 2002, "Photonic Crystal Enhanced Narrow-Band Infrared Emitters," *Applied Physics Letters*, Vol. 81, pp. 4685-4687.

Raether, H., 1988, *Surface Plasmons on Smooth and Rough Surfaces and on Gratings*, New York.

Raguin, D.H., and Morris, G.M., 1993, "Antireflection Structured Surfaces for the Infrared Spectral Region," *Applied Optics*, Vol. 32, pp. 1154-1167.

Roberts, S., 1959, "Optical Properties of Nickel and Tungsten and Their Interpretation According to Drude's Formula," *Physical Review*, Vol. 114, pp. 104-115.

Rytov, S.M., 1956, "Electromagnetic Properties of a Finely Stratified Medium," *Soviet Physics JETP*, Vol. 2, pp. 466-475.

Sai, H., Kanamori, Y., Hane, K., and Yugami, H., 2005, "Numerical Study on Spectral Properties of Tungsten One-Dimensional Surface-Relief Gratings for Spectrally Selective Devices," *Journal of the Optical Society of America A*, Vol. 22, pp. 1805-1813.

Sai, H., and Yugami, H., 2004, "Thermophotovoltaic Generation with Selective Radiators Based on Tungsten Surface Gratings," *Applied Physics Letters*, Vol. 85, pp. 3399-3401.

Semiconductor Industry Association, 2004, International Technology Roadmap for Semiconductors 2004 Update (http://public.rtrs/net).

Sentenac, A., and Greffet, J.-J., 1994, "Design of Surface Microrelief with Selective Radiative Properties," *International Journal of Heat and Mass Transfer*, Vol. 37, pp. 553-558.

Sharma, A.K., Zaidi, S.H., Logofătu, P.C., and Brueck, S.R.J., 2002, "Optical and Electrical Properties of Nanostructured Metal-Silicon-Metal Photodetectors," *IEEE Journal of Quantum Electronics*, Vol. 38, pp. 1651-1660.

Shen, Y.J., Zhu, Q.Z., and Zhang, Z.M., 2003, "A Scatterometer for Measuring the Bidirectional Reflectance and Transmittance of Semiconductor Wafers with Rough Surfaces," *Review of Scientific Instruments*, Vol. 74, pp. 4885-4892.

Siegel, R., and Howell, J.R., 2002, *Thermal Radiation Heat Transfer*, Taylor & Francis, New York.

Silverman, J.P., 1998, "Challenges and Progress in X-Ray Lithography," *Journal of Vacuum Science & Technology B*, Vol. 16, pp. 3137-3141.

Sun, B.K., Zhang, X., and Grigoropoulos, C.P., 1997, "Spectral Optical Functions of Silicon in the Range of 1.13–4.96 ev at Elevated Temperatures," *International Journal of Heat and Mass Transfer*, Vol. 40, pp. 1591-1600.

Tada, H., Abramson, A.R., Mann, S.E., Miaoulis, I.N., and Wong, P.Y., 2000, "Evaluating the Effects of Thin Film Patterns on the Temperature Distribution of Silicon Wafers during Radiant Processing," *Optical Engineering*, Vol. 39, pp. 2296-2304.

Tan, W.C., Preist, T.W., Sambles, J.R., and Wanstall, N.P., 1999, "Flat Surface-Plasmon-Polariton Bands and Resonant Optical Absorption on Short-Pitch Metal Gratings," *Physical Review B*, Vol. 59, pp. 12661-12666.

Tang, K., and Buckius, R.O., 1998, "The Geometric Optics Approximation for Reflection from Two-Dimensional Random Rough Surfaces," *International Journal of Heat and Mass Transfer*, Vol. 41, pp. 2037-2047.

Treacy, M.M.J., 1999, "Dynamical Diffraction in Metallic Optical Gratings," *Applied Physics Letters*, Vol. 75, pp. 606-608.

Vigil, O., Ruiz, C.M., Seuret, D., Bermudez, V., and Dieguez, E., 2005, "Transparent Conducting Oxides as Selective Filters in Thermophotovoltaic Devices," *Journal of Physics*, Vol. 17, pp. 6377-6384.

Wang, T.K., and Zemel, J.N., 1993, "Polarized Spectral Emittance from Periodic Micromachined Surfaces: V. Undoped Silicon : Angular Measurement in Shallow Lamellar Gratings," *Applied Optics*, Vol. 32, pp. 2021-2027.

Wu, T.K., 1997, "Infrared Filters for High-Efficiency Thermovoltaic Devices," *Microwave and Optical Technology Letters*, Vol. 15, pp. 9-12.

Xue, H., Yang, W.M., Chou, S.K., Shu, C., and Li, Z.W., 2005, "Microthermophotovoltaics Power System for Portable MEMS Devices," *Microscale Thermophysical Engineering*, Vol. 9, pp. 85-97.

Yang, W.M., Chou, S.K., Shu, C., Li, Z.W., and Xue, H., 2002, "Development of Microthermophotovoltaic System," *Applied Physics Letters*, Vol. 81, pp. 5255-5257.

Zhang, Q.-C., 2000, "Recent Progress in High-Temperature Solar Selective Coatings," *Solar Energy Materials and Solar Cells*, Vol. 62, pp. 63-74.

Zhang, Z.M., Fu, C.J., and Zhu, Q.Z., 2003, "Optical and Thermal Radiative Properties of Semiconductors Related to Micro/Nanotechnology," *Advances in Heat Transfer***,** Vol. 37, pp. 179-296.